nature immunology

Article

https://doi.org/10.1038/s41590-025-02210-x

DNA hypomethylation traits define human regulatory T cells in cutaneous tissue and identify their blood recirculating counterparts

Received: 11 October 2024

Accepted: 9 June 2025

A list of authors and their affiliations appears at the end of the paper

CD4$^+$ regulatory T (T$_{reg}$) cells in tissues play crucial immunoregulatory and regenerative roles. Despite their importance, the epigenetics and differentiation of human tissue T$_{reg}$ cells are incompletely understood. Here, we performed genome-wide DNA methylation analysis of human T$_{reg}$ cells from skin and blood and integrated these data into a multiomic framework, including chromatin accessibility and gene expression. This analysis identified programs that governed the tissue adaptation of skin T$_{reg}$ cells. We found that subfamilies of transposable elements represented a major constituent of the hypomethylated landscape in tissue T$_{reg}$ cells. Based on T cell antigen receptor sequence and DNA hypomethylation homologies, our data indicate that blood CCR8$^+$ T$_{reg}$ cells contain recirculating human skin T$_{reg}$ cells. Conversely, differences in chromatin accessibility and gene expression suggest a certain reversal of the tissue adaptation program during recirculation. Our findings provide insights into the biology of human tissue T$_{reg}$ cells, which may help harness these cells for therapeutic purposes.

CD4$^+$ regulatory T (T$_{reg}$) cells are a subset of CD4$^+$ T cells that exhibit a specific epigenetic framework[1] and exert immunosuppressive effects[2]. T$_{reg}$ cells in nonlymphoid tissues are phenotypically and functionally distinct from those in lymphoid tissues[3–7]. Nonlymphoid tissue adaptation is accompanied by the ability of tissue T$_{reg}$ cells to support tissue homeostasis and repair in multiple tissues[5,8–15]. In mice, tissue T$_{reg}$ cells were reported to develop in a multistep process from a tissue T$_{reg}$ progenitor that originates in lymphoid organs[4,6,16] and is dependent on several transcription factors, including BATF[3,4,10,17,18].

Although mouse tissue T$_{reg}$ cells have been well characterized, human tissue T$_{reg}$ cells remain incompletely understood, as few studies have focused on healthy human tissue T$_{reg}$ cells[6,10]. T$_{reg}$ cells in tumor tissues are the target of several clinical trials that aim to deplete CCR8$^+$ T$_{reg}$ cells in various solid tumors (NCT05537740, NCT05635643, NCT05518045, NCT06387628, NCT05007782, NCT05101070, NCT05935098 and NCT06131398). Although CCR8$^+$ T$_{reg}$ cells were thought to be a cancer-specific subpopulation of human T$_{reg}$ cells[19,20], recent data indicate that CCR8$^+$ T$_{reg}$ cells are also the predominant population of human tissue T$_{reg}$ cells in nontumor tissues[10]. Considering that cancer therapies targeting CCR8$^+$ T$_{reg}$ cells may also deplete a substantial proportion of tissue T$_{reg}$ cells in healthy tissues, further studies are needed to better understand the identity of tissue T$_{reg}$ cells. In addition to the CCR8$^+$ T$_{reg}$ cells located within human tissues, a circulating population of CCR8$^+$ T$_{reg}$ cells exists in healthy individuals and individuals with cancer[10,21]. This circulating CCR8$^+$ T cell subset displays some similarities to tissue T$_{reg}$ cells, including a notable amount of shared T cell antigen receptor (TCR) sequences[10,21]. Epigenetic data, providing long-term information about the differentiation state of cell populations, would allow us to precisely understand the relationship between circulating and tissue CCR8$^+$ T$_{reg}$ cells.

✉e-mail: delacher@uni-mainz.de; markus.feuerer@ukr.de

Therefore, we investigated DNA methylation, chromatin accessibility (assay for transposase-accessible chromatin using sequencing (ATAC-seq)) and gene expression data from human blood and skin CD45$^+$CD3$^+$CD4$^+$CD127$^-$CD25$^+$ T$_{\text{reg}}$ cells at multiple levels, including the transposable element (TE) landscape. TEs are components of the genome that can, or previously could, insert themselves at new genomic locations, a process called transposition[22,23]. In humans, they are estimated to account for 40–50% of the genome[24–26]. TEs can participate in gene regulation by being transcribed into RNAs or being part of promoters and enhancers and are often inactivated by DNA methylation[27–29]. Our analysis found a substantial number of hypomethylated TE subfamilies in human tissue T$_{\text{reg}}$ cells, which could potentially be reactivated, allowing them to function as enhancers. Further, our methylation data strongly indicated that recirculating tissue T$_{\text{reg}}$ cells are a part of the blood CCR8$^+$ T$_{\text{reg}}$ cell population.

Results

Hypomethylation defines skin and blood CCR8$^+$ T$_{\text{reg}}$ cells

Tissue T$_{\text{reg}}$ cells are characterized by their expression of CCR8 (Fig. 1a and Extended Data Fig. 1a). To define the relationship between blood CCR8$^+$ T$_{\text{reg}}$ cells and tissue T$_{\text{reg}}$ cells, we performed whole-genome bisulfite sequencing to investigate DNA methylation in blood antigen-inexperienced CD3$^+$CD4$^+$CD8$^-$CD25$^+$CD127$^-$CD45RA$^+$CD45RO$^-$ T$_{\text{reg}}$ cells, blood antigen-inexperienced CD3$^+$CD4$^+$CD8$^-$CD25$^-$CD127$^+$CD45RA$^+$CD45RO$^-$ conventional T (T$_{\text{conv}}$) cells, skin CD45$^+$CD3$^+$CD4$^+$CD8$^-$CD25$^+$CD127$^-$ T$_{\text{reg}}$ cells, skin CD45$^+$CD3$^+$CD4$^+$CD8$^-$CD25$^-$CD127$^+$ T$_{\text{conv}}$ cells and blood CD3$^+$CD4$^+$CD8$^-$CD25$^+$CD127$^-$CD45RA$^-$CD45RO$^+$CCR8$^+$ T$_{\text{reg}}$ cells from nine healthy female donors (Tissue Donors 7, 10 and 11 and Blood Donors 3–8; for age, see Methods; Fig. 1b). We analyzed 27,999,538 CpGs with a median coverage of 2–7× per sample (Extended Data Fig. 1b–d). Principal component analysis indicated that blood CD45RA$^+$ T$_{\text{reg}}$ and T$_{\text{conv}}$ cells clustered together, away from skin T$_{\text{reg}}$ cells and blood CCR8$^+$ T$_{\text{reg}}$ cells, which clustered together, and away from skin T$_{\text{conv}}$ cells (Fig. 1c). Analysis on a chromosomal level showed that, genome-wide, skin T$_{\text{reg}}$ cells and blood CCR8$^+$ T$_{\text{reg}}$ cells were hypomethylated compared to blood CD45RA$^+$ T$_{\text{reg}}$ cells (Fig. 1d). To extract methylation-level signatures that defined single cell types or groups of cell types, we examined methylation values at individual CpG sites. We specifically looked for CpG sites that separated cell types based on the corresponding methylation values. As such, we looked at the largest numeric gap in methylation between any two cell types. CpGs that met our criteria were considered 'signature CpGs', and groups of at least three consecutive CpGs that qualified as signature CpGs were defined as 'signature regions' (Fig. 1e). Depending on which cell types were hypomethylated in a signature region, the signature regions were grouped into 'signature categories'. The signature category that defined skin T$_{\text{reg}}$ cells, skin T$_{\text{conv}}$ cells and blood CCR8$^+$ T$_{\text{reg}}$ cells was the largest, encompassing 182,204 signature regions (Fig. 1f, Extended Data Fig. 1d and Supplementary Table 1). In most signature categories, most signature regions were associated with gene elements like introns, except for the 'skin T$_{\text{reg}}$, skin T$_{\text{conv}}$ and blood CCR8$^+$ T$_{\text{reg}}$' signature category, which was dominated by intergenic regions with very low association with CpG islands (Fig. 1g). These data show that blood CCR8$^+$ T$_{\text{reg}}$ cells exhibit a global hypomethylation landscape similar to that of tissue T$_{\text{reg}}$ and T$_{\text{conv}}$ cells.

A multiomics comparison identified DMR–peak–gene links

We used publicly available single-cell ATAC-seq (scATAC-seq) data[10] of skin and blood CD4$^+$ T cells from four healthy female donors (ATAC Donors 1, 2, 4 and 5; specific age range of skin and blood samples unknown; Methods and Extended Data Fig. 2a,b) and publicly available RNA-sequencing (RNA-seq) data[10] of sorted CD3$^+$CD4$^+$CD8$^-$CD25$^+$CD127$^-$CD45RO$^-$CD45RA$^+$ T$_{\text{reg}}$ cells and CD3$^+$CD4$^+$CD8$^-$CD25$^-$CD127$^+$CD45RO$^-$CD45RA$^+$ T$_{\text{conv}}$ cells from five healthy female donors of unknown age (Blood Donors 3–5, 9 and 10) to compare DNA methylation changes to chromatin accessibility and gene expression of blood CD45RA$^+$ naive T$_{\text{reg}}$ versus T$_{\text{conv}}$ cells. We identified a core naive T$_{\text{reg}}$ cell signature of more than 3,600 differentially methylated regions (DMRs) encompassing regions associated with classical T$_{\text{reg}}$ cell genes, including *TNFRSF1B*, *TNFRSF9*, *IKZF2*, *IKZF4* and *FOXP3* (Fig. 2a, Extended Data Fig. 2c,e and Supplementary Table 2), and determined DMR-accessible peak–gene links, in which a DMR overlapped with a differentially accessible peak and the associated gene was differentially expressed (hereafter 'DMR–peak–gene' links). This approach resulted in 151 DMR–peak–gene links comprising 73 genes (Fig. 2a). We noticed a correlation between hypomethylation changes on one hand and increased accessibility and increased gene expression levels on the other (Fig. 2b and Extended Data Fig. 2d), including DMR–peak–gene links associated with the T$_{\text{reg}}$ cell marker genes *TIGIT*, *IL2RA*, *FOXP3*, *CTLA4* and *TNFRSF1B* as well as new marker genes such as *DNAHB* or, on the opposite site, *LRRN3* and *SYTL3* (Fig. 2b,c and Extended Data Fig. 2f).

To validate the observed methylation differences for some of these links using a different technology, we used amplicon-based bisulfite sequencing in six independent healthy male blood donors (Amplicon Donors 1–6, age unknown). DNA extracted from CD3$^+$CD4$^+$CD25$^+$CD127$^-$CD45RA$^+$ T$_{\text{reg}}$ and CD3$^+$CD4$^+$CD25$^-$CD127$^+$CD45RA$^+$ T$_{\text{conv}}$ cells was used to amplify selected regions, including *FOXP3*, *TIGIT*, *IL2RA*, *TNFRSF1B*, *LRRN3* and *SYTL3*, by PCR followed by bisulfite sequencing. This confirmed the methylation differences for these loci observed by whole-genome bisulfite sequencing (Fig. 2d and Supplementary Table 4). Thus, the DMR–peak-gene link analysis identified new and confirmed known T$_{\text{reg}}$ cell-associated marker genes.

Skin T$_{\text{reg}}$ cell tissue adaptation has a multiomic signature

To define the tissue adaptation program of human skin T$_{\text{reg}}$ cells, we focused on differences between skin T$_{\text{reg}}$ and blood CD45RA$^+$ T$_{\text{reg}}$ cells.

Fig. 1 | DNA methylation separates skin T$_{\text{reg}}$ and blood CCR8$^+$ T$_{\text{reg}}$ cells from blood CD45RA$^+$ T$_{\text{reg}}$ cells. a, Representative flow cytometry plot showing CD45RA$^-$CCR8$^+$ T$_{\text{reg}}$ cells among CD4$^+$CD127$^-$CD25$^+$ T$_{\text{reg}}$ cells in human blood, fat and skin (left) and percentage of CD45RA$^-$CCR8$^+$ T$_{\text{reg}}$ cells among CD4$^+$CD127$^-$CD25$^+$ T$_{\text{reg}}$ cells in human blood compared to skin (right; $n = 6$ healthy female donors; FACS Donors 1–6; median age: 46 years; range: 31–61 years). The P value was determined by two-tailed Wilcoxon signed-rank test. **b**, Sort layout showing isolation of blood CD45RA$^+$ T$_{\text{reg}}$, blood CD45RA$^+$ T$_{\text{conv}}$, blood CCR8$^+$ T$_{\text{reg}}$, skin T$_{\text{conv}}$ and skin T$_{\text{reg}}$ cells in one healthy female donor (FACS Donor 7; age unknown). Not all gates are shown. **c**, Principal component analysis of DNA methylation in blood CD45RA$^+$ T$_{\text{reg}}$ cells (RA$^+$ T$_{\text{reg}}$ cells), blood CD45RA$^+$ T$_{\text{conv}}$ cells (RA$^+$ T$_{\text{conv}}$ cells), blood CCR8$^+$ T$_{\text{reg}}$ cells, skin T$_{\text{conv}}$ cells and skin T$_{\text{reg}}$ cells isolated from blood and skin from nine healthy female donors (Tissue Donors 7, 10 and 11 and Blood Donors 3–8). **d**, Methylation level by genomic position and corresponding differences with respect to blood CD45RA$^+$ T$_{\text{conv}}$ cells in blood CD45RA$^+$ T$_{\text{reg}}$, blood CCR8$^+$ T$_{\text{reg}}$, skin T$_{\text{conv}}$ and skin T$_{\text{reg}}$ cells in human donors as in **c**. Numbers in brackets indicate the average methylation level on autosomes and chromosome X. **e**, Schematic showing the extraction of cell-type signatures based on the largest numeric methylation gap between any two cell types (red arrows), which was required to be at least 0.15 and at least 1.5 times as large as the second-to-largest methylation gap (blue arrows) and resulted in the selection of signature regions; RA, CD45RA. **f**, DNA methylation in regions belonging to selected cell-type signatures as in **e**. Rows correspond to signature regions, and columns correspond to donors ($n = 3$ donors per cell type as in **c**). Numbers on the right indicate the number of regions per signature category. Signature nomenclature is based on the cell types that were hypomethylated in the corresponding signature regions. **g**, Distribution of cell-type signature regions from the signatures in **e** in genomic intervals defined by genes (top) and CpG islands (bottom). Numbers at the top indicate the number of regions per signature category. Data are representative of three or more independent experiments with three or more individual donors; TSS, transcription start site.

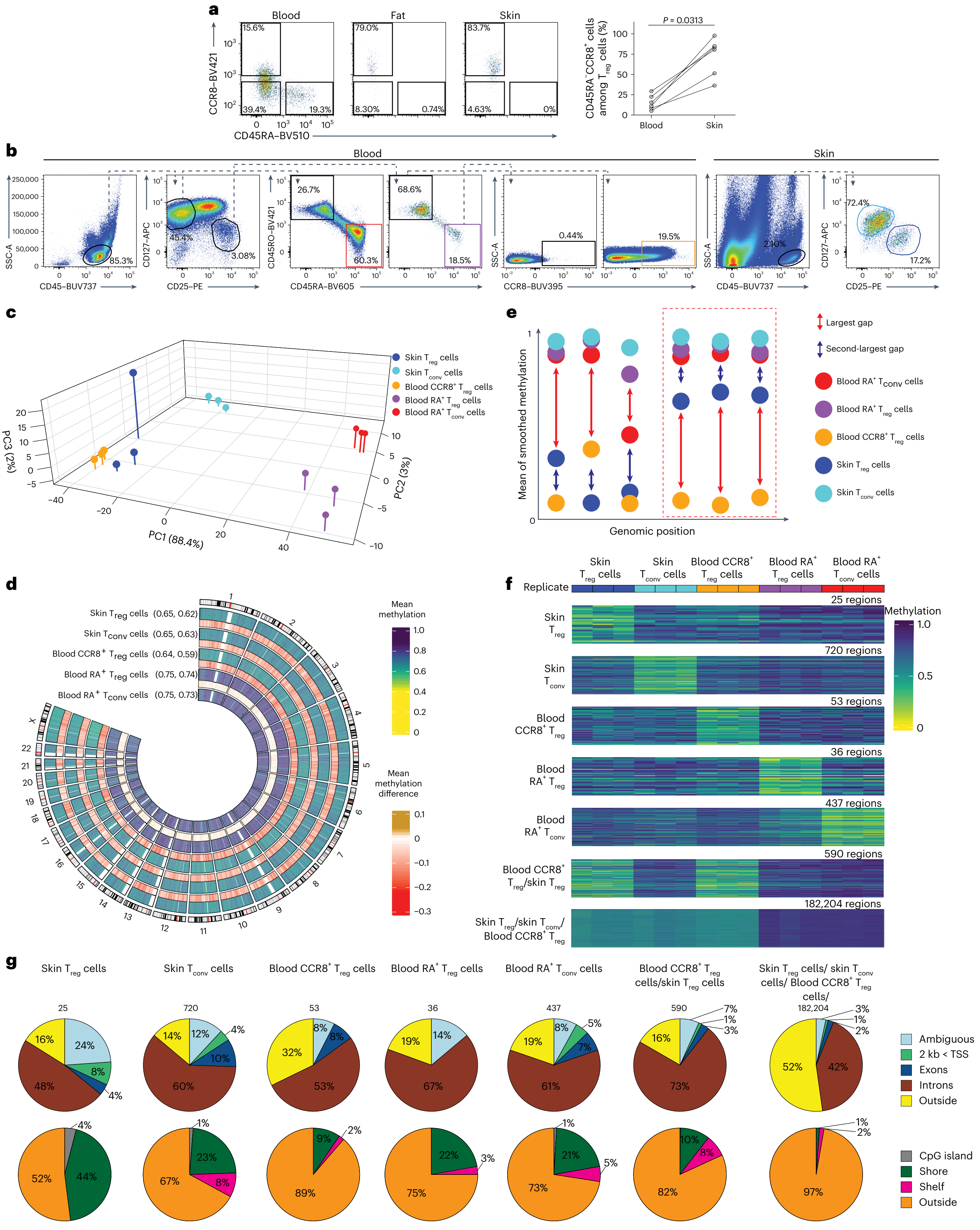
a
Blood
Fat
Skin
CCR8–BV421
CD45RA–BV510
15.6%
39.4%
19.3%
79.0%
8.30%
0.74%
83.7%
4.63%
0%
CD45RA−CCR8+ cells among Treg cells (%)
P = 0.0313
Blood
Skin
b
Blood
Skin
SSC-A
CD45–BUV737
85.3%
CD127–APC
CD25–PE
45.4%
3.08%
CD45RO–BV421
CD45RA–BV605
26.7%
60.3%
68.6%
18.5%
CCR8–BUV395
0.44%
19.5%
2.10%
72.4%
17.2%
c
Skin Treg cells
Skin Tconv cells
Blood CCR8+ Treg cells
Blood RA+ Treg cells
Blood RA+ Tconv cells
PC1 (88.4%)
PC2 (3%)
PC3 (2%)
d
Skin Treg cells (0.65, 0.62)
Skin Tconv cells (0.65, 0.63)
Blood CCR8+ Treg cells (0.64, 0.59)
Blood RA+ Treg cells (0.75, 0.74)
Blood RA+ Tconv cells (0.75, 0.73)
Mean methylation
Mean methylation difference
e
Mean of smoothed methylation
Genomic position
Largest gap
Second-largest gap
Blood RA+ Tconv cells
Blood RA+ Treg cells
Blood CCR8+ Treg cells
Skin Treg cells
Skin Tconv cells
f
Replicate
Skin Treg cells
Skin Tconv cells
Blood CCR8+ Treg cells
Blood RA+ Treg cells
Blood RA+ Tconv cells
Methylation
Skin Treg
25 regions
Skin Tconv
720 regions
Blood CCR8+ Treg
53 regions
Blood RA+ Treg
36 regions
Blood RA+ Tconv
437 regions
Blood CCR8+ Treg/skin Treg
590 regions
Skin Treg/skin Tconv/ Blood CCR8+ Treg
182,204 regions
g
Skin Treg cells
Skin Tconv cells
Blood CCR8+ Treg cells
Blood RA+ Treg cells
Blood RA+ Tconv cells
Blood CCR8+ Treg cells/skin Treg cells
Skin Treg cells/ skin Tconv cells/ Blood CCR8+ Treg cells/
25
720
53
36
437
590
182,204
Ambiguous
2 kb < TSS
Exons
Introns
Outside
CpG island
Shore
Shelf
Outside

Therefore, we compared our DNA methylation data to publicly available scATAC-seq data[10] of skin and blood $CD4^+$ T cells (four healthy female donors; ATAC Donors 1, 2, 4 and 5; specific age range of blood and skin samples unknown; see Methods) and publicly available RNA-seq data[10] of sorted $CD45^+CD3^+CD4^+CD8^-CD25^+CD127^-$ skin T_{reg} cells and $CD3^+CD4^+CD8^-CD25^+CD127^-CD45RO^-CD45RA^+$ blood T_{reg} cells from nine healthy female donors (Tissue Donors 7, 8, 10 and 11 and Blood Donors 3–5, 9 and 10) as described above. This comparison identified a methylation skin T_{reg} signature comprising 300,199 DMRs (298,457 hypomethylated regions), an accessibility skin T_{reg} signature comprising 8,914 peaks (3,192 significantly hyperaccessible peaks) and a gene expression skin T_{reg} signature comprising 6,877 genes (4,049 significantly overexpressed genes; Fig. 3a, Extended Data Fig. 3a and Supplementary Table 3).

Analysis of DMR–peak–gene links identified 1,203 links and showed a notable negative correlation between hypomethylation changes and increased accessibility and gene expression (Fig. 3b and Extended Data Fig. 3b). This ensemble of DMR–peak–gene links contained 813 links (785 DMRs, 793 peaks and 408 genes) that lost methylation and gained accessibility and expression (*TNFRSF8*, *RELB*, *CCR8*, *PRDM1* and *BATF*) and 223 links (210 DMRs, 211 peaks and 132 genes) that gained methylation and lost accessibility and expression (*TGFBR2*, *SELL* and *IGF1R*) in skin T_{reg} cells (Fig. 3c and Extended Data Fig. 3c). Enrichment of Hallmark gene sets[30] among links that lost methylation but gained accessibility and gene expression in skin T_{reg} cells identified processes including interleukin-2 (IL-2)–STAT5 signaling, TNF signaling and TGFβ signaling (Fig. 3d). We also analyzed genomic regions that experienced strong methylation changes during skin T_{reg} cell tissue adaptation that were not part of the DMR–peak–gene links and found that most regions (297,577) were hypomethylated (Extended Data Fig. 3d and Supplementary Table 3).

To investigate whether the 'core naive T_{reg}' and 'skin T_{reg}' cell signatures (as defined in Figs. 2a and 3a, respectively) were shared with T_{reg} cells from other tissues, we generated whole-genome methylation data from $CD45^+CD3^+CD4^+CD8^-CD25^+CD127^-$ T_{reg} cells isolated from the subcutaneous fat of three healthy female donors (Tissue Donors 6, 7 and 8). In addition, we used publicly available scATAC-seq[10] data from subcutaneous adipose tissue $CD4^+$ T cells (three healthy female donors; ATAC Donors 3–5; age unknown) and bulk RNA-seq data[10] from fat T_{reg} cells (five healthy female donors; Tissue Donors 5–9). The skin tissue T_{reg} cell signature defined against blood $CD45RA^+$ T_{reg} cells showed strong similarities between skin and fat T_{reg} cells (Extended Data Fig. 3e). These results suggest a conserved tissue adaptation program for human T_{reg} cells.

Methylation of bZIP and bHLH motifs marks skin T_{reg} cells

To identify transcription factors whose activity may be affected by epigenetic changes in skin T_{reg} cells, we analyzed the enrichment of transcription factor motifs in DMRs and differentially accessibility peaks between skin T_{reg} cells and blood $CD45RA^+$ T_{reg} cells (Supplementary Table 5). A range of motifs for basic leucine zipper (bZIP) transcription factors, such as BATF or the composite Jun–AP1, was enriched in skin T_{reg} cell hypomethylation DMRs and skin T_{reg} cell hyperaccessibility peaks compared to randomly selected background sets of genomic regions[31] (Fig. 4a,b and Extended Data Fig. 4a–c), suggesting that regions around bZIP motifs became hypomethylated and were more accessible during skin T_{reg} cell tissue adaptation. Furthermore, we found an enrichment of several basic helix–loop–helix (bHLH) transcription factor motifs (such as c-Myc, n-Myc and USF1) in skin T_{reg} cell hypomethylation DMRs, but not in skin T_{reg} cell hyperaccessibility peaks (Fig. 4c,d and Extended Data Fig. 4d–f), suggesting that the function of bHLH transcription factors was regulated more by changes in DNA methylation than by changes in chromatin accessibility. To determine which of these transcription factors gain activity during skin T_{reg} cell tissue adaptation, we analyzed the 'transcriptomic footprints' of their activity by measuring the enrichment of their target genes among genes that were differentially expressed between skin T_{reg} cells and blood $CD45RA^+$ T_{reg} cells. Several bZIP and bHLH factors, including Jun, JunB, c-Myc and USF1, had a 'transcriptomic footprint' and were expressed in skin T_{reg} cells (Fig. 4e,f). This gain in activity might indicate an involvement in the tissue adaptation of skin T_{reg} cells. The genes *MLPH* and *GNA11* contained a chromatin immunoprecipitation with sequencing (ChIP–seq)-confirmed c-Myc or USF1 binding site[32] that displayed hypomethylation in skin T_{reg} cells compared to blood $CD45RA^+$ T_{reg} cells (Fig. 4g and Extended Data Fig. 4g). To assess whether the c-Myc binding sites played a regulatory role for these genes, we targeted their surroundings, as determined by motif analysis and public ChIP–seq data[32], using a CRISPR-based transcriptional activation system (CRISPRa) in human primary blood $CD3^+CD4^+CD25^+CD127^-$ T_{reg} cells from six donors (CRISPR Donors 1–6; three donors per guide RNA; see Methods) of unknown sex and age to activate the sites in situ. CRISPRa targeting with specific guide RNAs upregulated *MLPH* and *GNA11* gene expression compared to scrambled control guide RNA (Fig. 4g and Extended Data Fig. 5). These data suggest a regulatory enhancer potential of hypomethylated regions containing c-Myc binding sites.

Blood $CCR8^+$ T_{reg} cells resemble skin T_{reg} cells

Next, we investigated the positioning of blood $CCR8^+$ T_{reg} cells relative to blood $CD45RA^+$ T_{reg} cells and skin T_{reg} cells using our methylation, accessibility and RNA expression skin T_{reg} cell signatures. Analysis of the 300,199 DMRs indicated that more than 97% (293,604) of the methylation values of the DMRs in blood $CCR8^+$ T_{reg} cells were closer to those in skin T_{reg} cells than to those in blood $CD45RA^+$ T_{reg} cells (Fig. 5a, Extended Data Fig. 6a,b and Supplementary Table 6). Analysis of about 8,914 accessibility features placed blood $CCR8^+$ T_{reg} cells closer to skin T_{reg} cells in less than 60% (5,285) of features (Fig. 5a and Extended Data Fig. 6a,b), whereas analysis of gene expression levels showed that less than 45% (2,988) of genes placed blood $CCR8^+$ T_{reg} cells closer to skin T_{reg} cells than to $CD45RA^+$ T_{reg} cells (Fig. 5a and Extended Data Fig. 6a,b). These differences were seen in each donor analyzed (Fig. 5b). An analysis restricted to DMR–peak–gene links revealed a similar methylation,

Fig. 2 | A multiomics comparison defines a core T_{reg} cell signature. **a**, Methylation, chromatin accessibility and expression of DMRs (left), differentially accessible peaks (middle) and differentially expressed genes (right) between blood $CD45RA^+$ T_{reg} cells (RA^+ T_{reg} cells) and blood $CD45RA^+$ T_{conv} cells (RA^+ T_{conv} cells). Rows represent genomic regions (left and middle) or genes (right). Columns indicate samples from individual donors (left and right) or mean accessibility across cells from a single donor (middle); $n = 3$ donors (methylation, Blood Donors 3–5), 2 donors (accessibility, ATAC Donors 1 and 2) and 3 blood $CD45RA^+$ T_{conv} donors and 5 blood $CD45RA^+$ T_{reg} donors (expression, Blood Donors 3–5, 9 and 10). **b**, Correlation between differential methylation, accessibility and expression for DMR–peak–gene links ($n = 151$ DMR–peak–gene links). Positive values indicate larger methylation, accessibility or expression in blood $CD45RA^+$ T_{reg} cells. Donors are as in **a**; gex., gene expression. **c**, Smoothed methylation (top left), raw methylation (top right), chromatin accessibility (bottom left) and expression (bottom right; mean ± s.d.) for selected DMR–peak–gene links in blood $CD45RA^+$ T_{reg} and blood $CD45RA^+$ T_{conv} cells. Highlighted regions mark DMRs (methylation tracks) and differential peaks (accessibility tracks). Vertical lines at the bottom of the methylation tracks mark CpG sites. Gene expression P values were determined by two-tailed Wald test implemented in DEseq2 ($n = 5$ T_{reg} cell donors and 3 T_{conv} cell donors) with a Benjamini–Hochberg correction. Donors are as in **a**; P_{adj}, adjusted P value. **d**, Amplicon-based bisulfite sequencing showing methylation differences between blood $CD45RA^+$ T_{reg} and blood $CD45RA^+$ T_{conv} cells in selected regions ($n = 6$ donors, Amplicon Donors 1–6). Each circle corresponds to a CpG site. P values were determined by two-tailed Wilcoxon signed-rank test ($n = 6$ donors) with a Benjamini–Hochberg correction; Acc., accessibility; adj., adjusted; Meth., methylation; RPKM, reads per kilobase per million; TPM, transcripts per million. Data are representative of two or more independent experiments with two or more individual donors.

https://doi.org/10.1038/s41590-025-02210-x

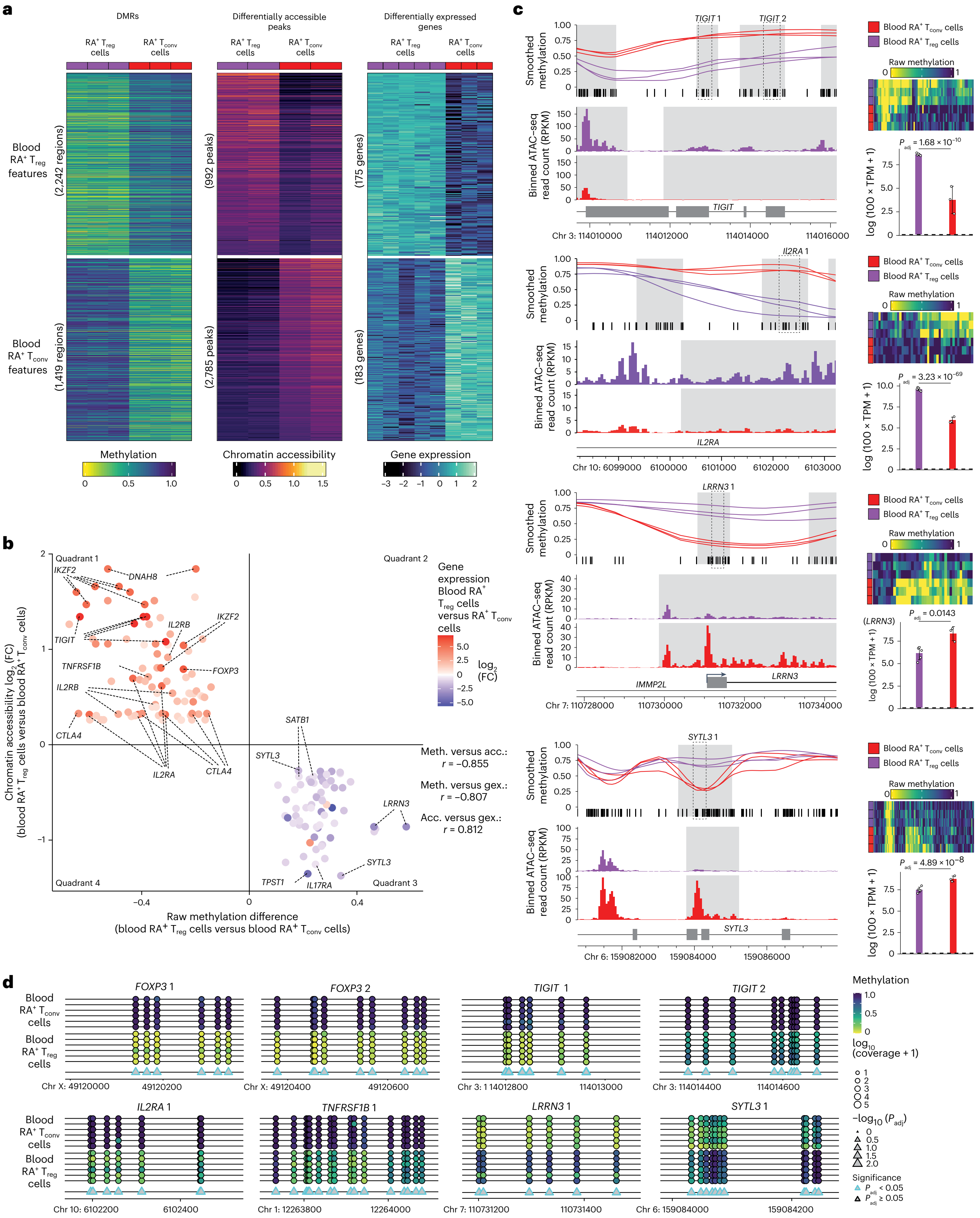

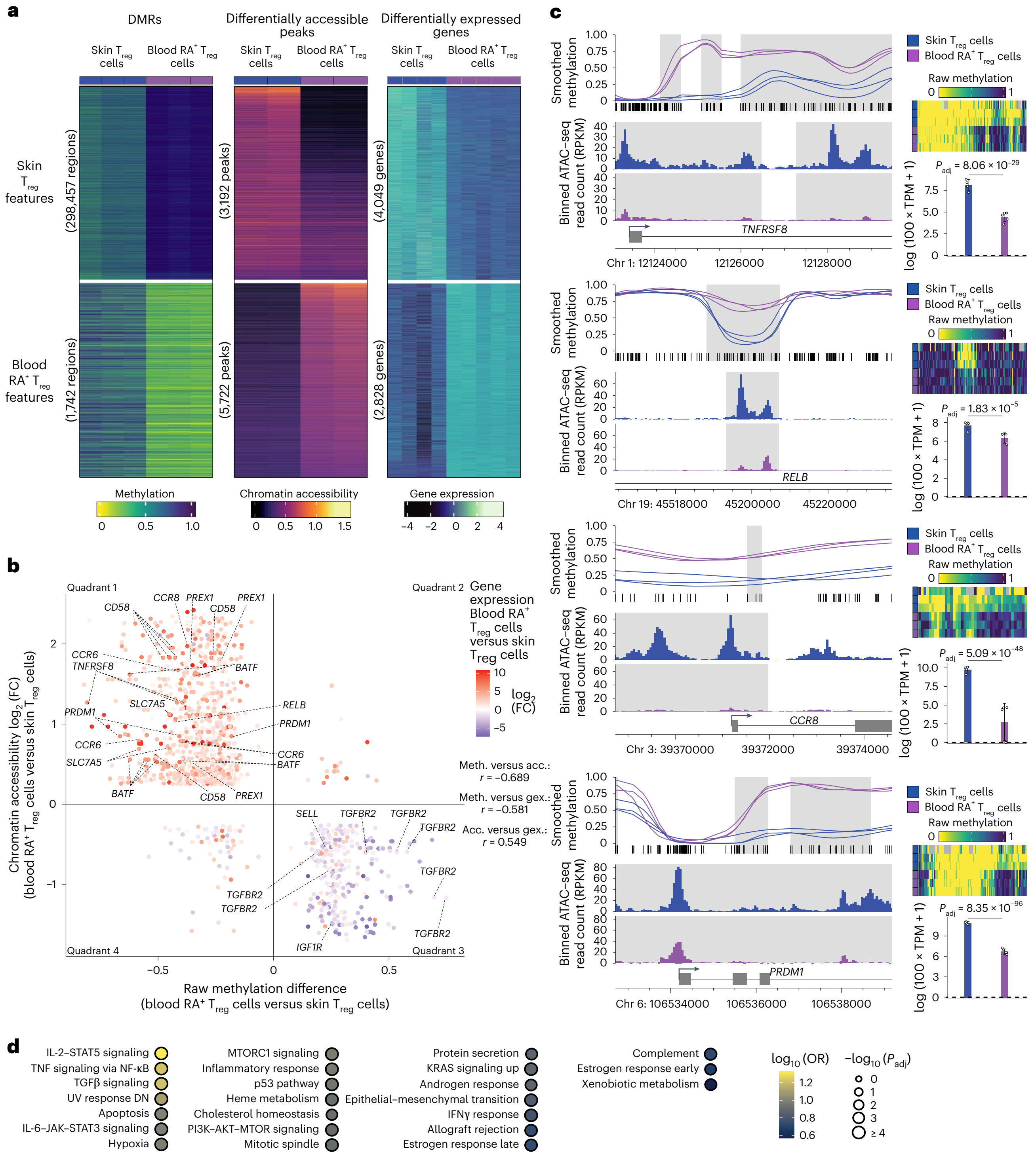

Fig. 3 | DMR–peak–gene links define a multiomic signature of skin T_{reg} cell development. a, Methylation, chromatin accessibility and expression of DMRs (left), differentially accessible peaks (middle) and differentially expressed genes (right) between skin T_{reg} cells and blood CD45RA$^+$ T_{reg} cells (blood RA$^+$ T_{reg} cells). Rows represent genomic regions (left and middle) or genes (right). Columns indicate samples from individual donors (left and right) or mean accessibility across cells from a single donor (middle); *n* = 3 donors per cell type (methylation, Tissue Donors 7, 10 and 11 and Blood Donors 3–5), 2 donors per cell type (accessibility, ATAC Donors 1, 2, 4 and 5), 4 skin T_{reg} donors and 5 blood CD45RA$^+$ T_{reg} donors (expression, Tissue Donors 7, 8, 10 and 11 and Blood Donors 3–5, 9 and 10). **b**, Correlation between differential methylation, accessibility and expression for DMR–peak–gene links (*n* = 1,203 DMR–peak–gene links). Positive values indicate larger methylation, accessibility or expression in skin T_{reg} cells. Donors are as in **a**; FC, fold change. **c**, Smoothed methylation (top left), raw methylation (top right), chromatin accessibility (bottom left) and gene expression (bottom right; mean ± s.d.) in skin T_{reg} and blood CD45RA$^+$ T_{reg} cells for selected DMR–peak–gene links. Highlighted regions mark DMRs (methylation tracks) and differential peaks (accessibility tracks). Vertical lines at the bottom of the methylation tracks mark CpG sites. Gene expression *P* values were determined by two-tailed Wald test implemented in DESeq2 (*n* = 4 skin donors and 5 blood donors) with a Benjamini–Hochberg correction. Donors are as in **a**. **d**, Enrichment of hallmark gene sets among genes belonging to the multiomic skin T_{reg} cell signature. All gene sets displaying a P_{adj} of <0.01 are shown. *P* values were determined by one-tailed Fisher's exact test (*n* = 408 genes from the multiomic signature) with a Benjamini–Hochberg correction; DN, down; OR, odds ratio; *r*, Pearson correlation. Data are representative of two or more independent experiments with two or more individual donors.

https://doi.org/10.1038/s41590-025-02210-x

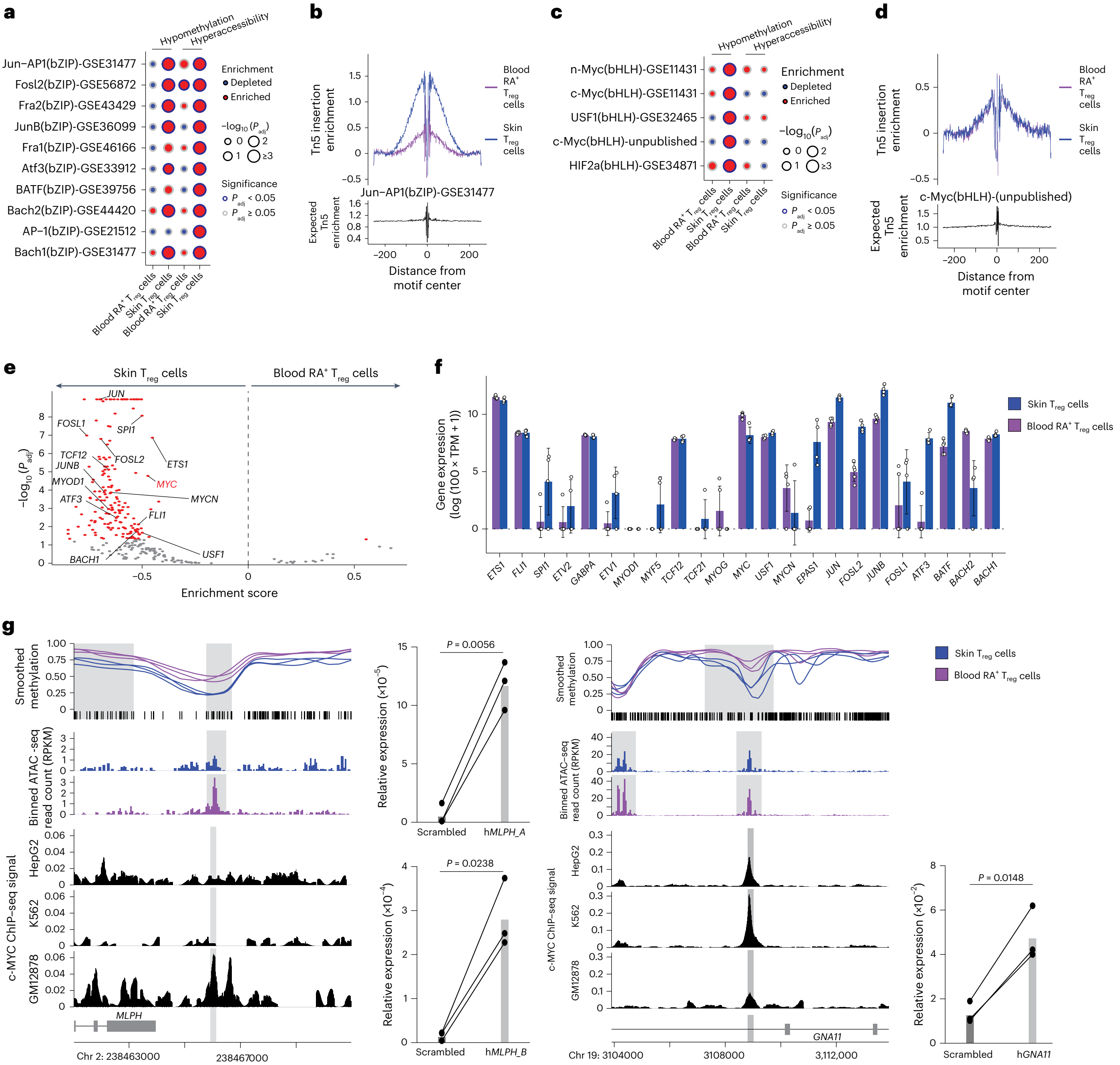

Fig. 4 | Activity of bZIP and bHLH transcription factors during skin T_{reg} cell development is associated with binding site hypomethylation. a, Enrichment of bZIP motifs in DMRs and differential peaks between skin T_{reg} cells and blood CD45RA$^+$ T_{reg} cells (blood RA$^+$ T_{reg} cells). *P* values were determined by one-tailed binomial test implemented in homer[31] (n = 1,742 DMRs, 298,457 DMRs, 5,722 peaks and 3,192 peaks for columns 1–4) with a Benjamini–Hochberg correction. **b**, Chromatin accessibility in skin T_{reg} and blood CD45RA$^+$ T_{reg} cells (four donors, ATAC Donors 1, 2, 4 and 5) around genomic sites for a selected bZIP motif. **c**, Enrichment of bHLH motif sites in DMRs and differential peaks between skin T_{reg} cells and blood CD45RA$^+$ T_{reg} cells. *P* values were determined as in **a**. **d**, Chromatin accessibility in skin T_{reg} and blood CD45RA$^+$ T_{reg} cells around genomic sites for a selected bHLH motif. Donors are as in **b**. **e**, Transcriptomic footprint of transcription factors (that is, enrichment of target genes) among genes differentially expressed between skin T_{reg} and blood CD45RA$^+$ T_{reg} cells. Labels correspond to transcription factor gene names. *P* values were determined by two-tailed permutation test (n = 28,078 genes) with a Benjamini–Hochberg correction. **f**, Expression of transcription factor genes corresponding to relevant motifs (mean ± s.d.; n = 4 skin T_{reg} cell donors and 5 blood CD45RA$^+$ T_{reg} cell donors, Tissue Donors 7, 8, 10 and 11 and Blood Donors 3–5, 9 and 10). **g**, Methylation (top left, Tissue Donors 7, 10 and 11 and Blood Donors 3–5) and chromatin accessibility (middle left, ATAC Donors 1, 2, 4 and 5) in skin T_{reg} and blood CD45RA$^+$ T_{reg} cells together with c-Myc ChIP–seq signal[32] from three cell lines (bottom left) around c-Myc motif sites associated with *MLPH* and *GNA11* and quantitative PCR with reverse transcription showing relative gene expression (mean) of *MLPH* (guide RNA A or B) and *GNA11* in primary blood T_{reg} cells from six donors (CRISPR Donors 1–6, three donors per guide RNA) after CRISPR-mediated activation originating from regions shown in track plots (right). Highlighted regions correspond to selected DMRs (methylation tracks), scATAC-seq peaks (chromatin accessibility tracks) and c-Myc motif sites (motif ± 100 bases; ChIP–seq and gene tracks). Vertical lines at the bottom of the methylation tracks mark CpG sites. *P* values were determined by two-tailed paired *t*-test (n = 3 donors). Data are representative of two or more independent experiments with two or more individual donors.

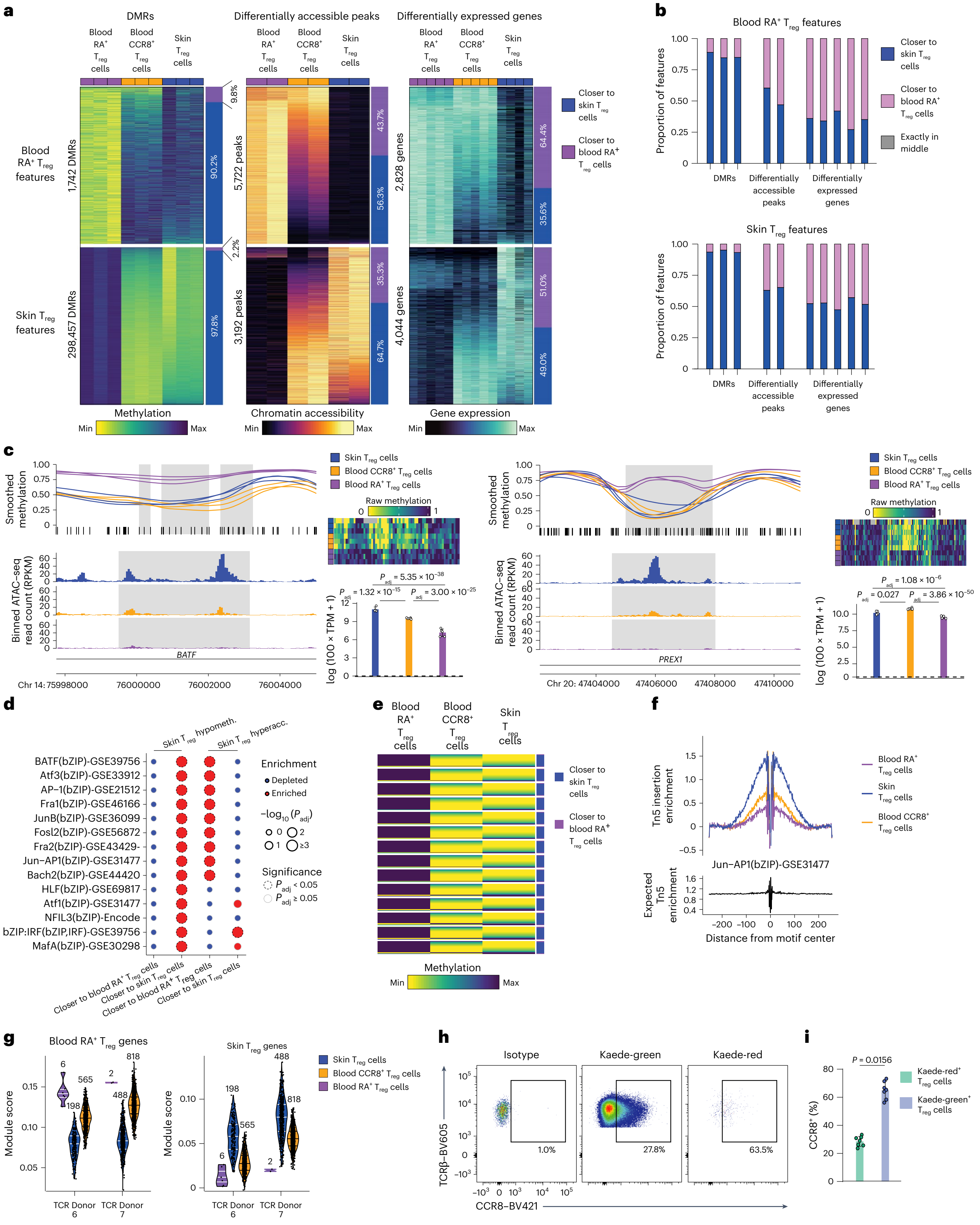
a
DMRs
Differentially accessible peaks
Differentially expressed genes
Blood RA+ Treg cells
Blood CCR8+ Treg cells
Skin Treg cells
Blood RA+ Treg features
Skin Treg features
1,742 DMRs
298,457 DMRs
5,722 peaks
3,192 peaks
2,828 genes
4,044 genes
9.8%
90.2%
2.2%
97.8%
43.7%
56.3%
35.3%
64.7%
64.4%
35.6%
51.0%
49.0%
Closer to skin Treg cells
Closer to blood RA+ Treg cells
Methylation
Chromatin accessibility
Gene expression
Min
Max
b
Blood RA+ Treg features
Skin Treg features
Proportion of features
1.00
0.75
0.50
0.25
0
DMRs
Differentially accessible peaks
Differentially expressed genes
Closer to skin Treg cells
Closer to blood RA+ Treg cells
Exactly in middle
c
Smoothed methylation
Binned ATAC–seq read count (RPKM)
Skin Treg cells
Blood CCR8+ Treg cells
Blood RA+ Treg cells
Raw methylation
BATF
Chr 14: 75998000
76000000
76002000
76004000
log (100 × TPM + 1)
Padj = 5.35 × 10−38
Padj = 1.32 × 10−15
Padj = 3.00 × 10−25
PREX1
Chr 20: 47404000
47406000
47408000
47410000
Padj = 1.08 × 10−6
Padj = 0.027
Padj = 3.86 × 10−50
d
Skin Treg hypometh.
Skin Treg hyperacc.
BATF(bZIP)-GSE39756
Atf3(bZIP)-GSE33912
AP-1(bZIP)-GSE21512
Fra1(bZIP)-GSE46166
JunB(bZIP)-GSE36099
Fosl2(bZIP)-GSE56872
Fra2(bZIP)-GSE43429-
Jun-AP1(bZIP)-GSE31477
Bach2(bZIP)-GSE44420
HLF(bZIP)-GSE69817
Atf1(bZIP)-GSE31477
NFIL3(bZIP)-Encode
bZIP:IRF(bZIP,IRF)-GSE39756
MafA(bZIP)-GSE30298
Closer to blood RA+ Treg cells
Closer to skin Treg cells
Closer to blood RA+ Treg cells
Closer to skin Treg cells
Enrichment
Depleted
Enriched
−log10 (Padj)
0
1
2
≥3
Significance
Padj < 0.05
Padj ≥ 0.05
e
Blood RA+ Treg cells
Blood CCR8+ Treg cells
Skin Treg cells
Closer to skin Treg cells
Closer to blood RA+ Treg cells
Methylation
Min
Max
f
Tn5 insertion enrichment
Blood RA+ Treg cells
Skin Treg cells
Blood CCR8+ Treg cells
Jun-AP1(bZIP)-GSE31477
Expected Tn5 enrichment
Distance from motif center
g
Blood RA+ Treg genes
Skin Treg genes
Module score
TCR Donor 6
TCR Donor 7
Skin Treg cells
Blood CCR8+ Treg cells
Blood RA+ Treg cells
h
Isotype
Kaede-green
Kaede-red
1.0%
27.8%
63.5%
TCRβ–BV605
CCR8–BV421
i
P = 0.0156
CCR8+ (%)
Kaede-red+ Treg cells
Kaede-green+ Treg cells

Fig. 5 | DNA methylation patterns reflect similarity of skin T_{reg} and blood $CCR8^+$ T_{reg} cells. a, Methylation (Tissue Donors 7, 10 and 11 and Blood Donors 3–8), chromatin accessibility (ATAC Donors 1, 2, 4 and 5) and gene expression (Tissue Donors 7, 8, 10 and 11 and Blood Donors 3–12) of features that are different between skin T_{reg} and blood $CD45RA^+$ T_{reg} cells (blood RA^+ T_{reg} cells). Annotation bars indicate blood $CCR8^+$ T_{reg} cell positioning. **b**, Proportions of features placing blood $CCR8^+$ T_{reg} cells closer to skin T_{reg} cells or blood $CD45RA^+$ T_{reg} cells. Donors are as in **a**. **c**, Smoothed methylation (top left), raw methylation (top right), chromatin accessibility (bottom left) and gene expression (bottom right, mean ± s.d.) in skin T_{reg}, blood $CCR8^+$ T_{reg} and blood $CD45RA^+$ T_{reg} cells for regions where blood $CCR8^+$ T_{reg} cells are closer to blood $CD45RA^+$ T_{reg} cells than to skin T_{reg} cells regarding chromatin accessibility. Highlighted regions mark DMRs and differential peaks. *P* values were determined by two-tailed Wald test implemented in DESeq2 ($n = 4$, 5 and 5 donors for skin T_{reg} cells, blood $CCR8^+$ T_{reg} cells and blood $CD45RA^+$ T_{reg} cells, respectively) with a Benjamini–Hochberg correction. Donors are as in **a**. **d**, Enrichment of bZIP motifs in feature sets defined by blood $CCR8^+$ T_{reg} cell positionings. *P* values were determined by one-tailed binomial test implemented in homer[31] ($n = 6{,}424$ DMRs, 292,033 DMRs, 1,128 peaks and 2,064 peaks for columns 1–4) with a Benjamini–Hochberg correction. **e**, Methylation around genomic sites (±200 bases) for bZIP motifs overlapping with DMRs (mean across three biological replicates) in skin T_{reg}, blood $CCR8^+$ T_{reg} and blood RA^+ T_{reg} cells. Annotation bars indicate whether blood $CCR8^+$ T_{reg} cells are closer to skin T_{reg} cells or blood $CD45RA^+$ T_{reg} cells as in **a**. Donors are as in **a**. Heat maps are ordered as in **d**. **f**, Chromatin accessibility in skin T_{reg}, blood $CCR8^+$ T_{reg} and blood $CD45RA^+$ T_{reg} cells around genomic sites for a selected bZIP motif (see Fig. 4). Donors are as in **a**. **g**, Module scores (with cell numbers, median and bottom/top quartile) of genes upregulated in blood $CD45RA^+$ T_{reg} or skin T_{reg} cells in TCR-matched blood $CCR8^+$ T_{reg}, skin T_{reg} and blood $CD45RA^+$ T_{reg} cells from two donors (TCR Donors 6 and 7). **h**,**i**, Concatenated flow cytometry plot showing CCR8 expression (**h**) and percentage of $CCR8^+$ cells among $Kaede\text{-}red^+$ T_{reg} cells and $Kaede\text{-}green^+$ T_{reg} cells (**i**) in skin dLN T_{reg} cells of Kaede mice 6 days after skin photoconversion from Kaede-green to Kaede-red (data concatenated from seven mice; mean ± s.d.). The *P* value was determined by two-tailed Wilcoxon signed-rank test. Data are representative of two or more independent experiments with two or more individual donors.

accessibility and gene expression pattern between blood $CCR8^+$ T_{reg} cells and skin or blood $CD45RA^+$ T_{reg} cells (Extended Data Fig. 6c). These data indicate that the methylation landscape of blood $CCR8^+$ T_{reg} cells was analogous to that of skin T_{reg} cells, whereas similarities in chromatin accessibility and gene expression were less pronounced. Regions in which skin T_{reg} cell traits were reflected by methylation, but not by accessibility, in blood $CCR8^+$ T_{reg} cells included *BATF*, *PREX1*, a member of the phosphatidylinositol-3,4,5-trisphosphate signaling pathway, and *SPRED2*, a Ras regulator (Fig. 5c and Extended Data Fig. 6d).

To investigate how well the epigenetic properties of blood $CCR8^+$ T_{reg} cells reflected traits linked to transcription factor motifs, we examined DMRs and differentially accessible peaks from the 'skin T_{reg} cell hypomethylation' and 'skin T_{reg} cell hyperaccessibility' signatures as defined above and performed motif enrichment analysis to assess whether transcription factor motifs were enriched in these DMRs and peaks compared to background sets of genomic regions[31]. bZIP motifs were significantly enriched in DMRs that placed blood $CCR8^+$ T_{reg} cells closer to skin T_{reg} cells than to blood $CD45RA^+$ T_{reg} cells (Fig. 5d,e and Extended Data Fig. 7a), indicating that the epigenetic characteristics surrounding bZIP motifs in skin T_{reg} cells were well reflected by the methylation level in blood $CCR8^+$ T_{reg} cells. These effects were less pronounced when analyzing chromatin accessibility data around the genomic sites of Jun–AP1(bZIP) and other bZIP motifs (Fig. 5d,f and Extended Data Fig. 7b). We also observed an enrichment of many bHLH motifs among DMRs that placed blood $CCR8^+$ T_{reg} cells closer to skin T_{reg} cells than to blood $CD45RA^+$ T_{reg} cells (Extended Data Fig. 7c,d), indicating that skin T_{reg} cell-related methylation traits of bHLH motifs were reflected by blood $CCR8^+$ T_{reg} cells.

To assess whether loss of conservation of skin T_{reg} cell signature gene expression in blood $CCR8^+$ T_{reg} cells could be detected in identical αβ TCR clones, we analyzed previously published scRNA-seq and scTCR-seq data[10] from skin T_{reg} cells and blood $CCR8^+$ T_{reg} cells from two healthy female donors (TCR Donors 6 and 7, unknown age; Extended Data Fig. 8a–d). We identified 198 (TCR Donor 6) and 488 (TCR Donor 7) skin T_{reg} cells that shared TCR sequences with blood $CCR8^+$ T_{reg} cells compared to 565 (TCR Donor 6) and 818 (TCR Donor 7) blood $CCR8^+$ T_{reg} cells that shared TCR sequences with skin T_{reg} cells (Fig. 5g). In total, 4–10% of all identified blood $CCR8^+$ T_{reg} TCR clonotypes could also be found in skin T_{reg} cells, whereas only about 0.3% of all identified blood $CD45RA^+$ T_{reg} TCR clonotypes were also found in skin T_{reg} cells (Extended Data Fig. 8e). Furthermore, more than 38% of TCR clonotypes found in skin T_{reg} cells were also found in blood $CCR8^+$ T_{reg} cells, compared to less than 2.5% in blood $CD45RA^+$ T_{reg} cells (Extended Data Fig. 8f), indicating considerable clonal TCR overlap between blood $CCR8^+$ T_{reg} cells and skin T_{reg} cells. To determine the conservation of gene expression patterns in TCR-identical clones between blood $CCR8^+$ T_{reg} cells and skin T_{reg} cells, we calculated the aggregated expression of genes from the skin T_{reg} signature ('skin T_{reg} cell hyperexpression' genes and 'blood $CD45RA^+$ T_{reg} hyperexpression' genes) into module scores per cell. This analysis indicated that loss of the skin T_{reg} cell-specific gene expression program and gain of a more naive phenotype occurred once clones left the skin (Fig. 5g).

In mice, CCR8 is a marker for tissue T_{reg} cells, similar to in humans[10]. To experimentally test whether $CCR8^+$ T_{reg} cells represented recirculating tissue T_{reg} cells, we used Tg(CAG-Kaede)15Kgwa mice, which ubiquitously express the photoconvertible fluorescence protein Kaede (which switches from green to red after exposure to violet light) under the control of a CAG promoter[33]. On day 6, after exposing the back skin to 5 min of violet light, we found photoconverted $Kaede\text{-}red^+$ migratory skin T_{reg} cells in the skin draining lymph nodes (dLNs; Extended Data Fig. 8g), as has been previously observed[34]. Approximately 65% of these

Fig. 6 | TEs are hypomethylated in skin T_{reg} cells and blood $CCR8^+$ T_{reg} cells. a,**b**, Enrichment of TE classes and subfamilies in regions hypomethylated (**a**) or hyperaccessible (**b**) in skin T_{reg} cells. *P* values were determined by one-tailed permutation test ($n = 298{,}457$ DMRs and 3,192 differential peaks) with a Benjamini–Hochberg correction; RC, rolling circle. **c**, Methylation of annotated insertion sites (with median) for three TE classes in skin T_{reg} and blood $CD45RA^+$ T_{reg} cells (blood RA^+ T_{reg} cells; left; three donors per cell type; Tissue Donors 7, 10 and 11 and Blood Donors 3–5) and distribution of differences in mean methylation (across the three donors) between skin T_{reg} and blood $CD45RA^+$ T_{reg} cells for each insertion site (right). The numbers indicate how many insertion sites displayed differences below and above 0; AU, arbitrary units. **d**, Methylation (donors are as in **c**) and chromatin accessibility (ATAC Donors 1, 2, 4 and 5) in skin T_{reg} and blood $CD45RA^+$ T_{reg} cells around selected TE insertion sites. Highlighted regions mark DMRs (methylation tracks), differential peaks (accessibility tracks) and TE insertion sites overlapping with DMRs (only TE subfamilies enriched among the DMRs; gene tracks). Vertical lines at the bottom of the methylation tracks mark CpG sites (CpG sites overlapping with TEs are shown in red). TE labels correspond to TE subfamilies (partly overlaps with Figs. 3 and 5). **e**,**f**, Enrichment of TE classes and subfamilies in regions that are hypomethylated (**e**) or hyperaccessible (**f**) in skin T_{reg} cells and defined by specific positionings of blood $CCR8^+$ T_{reg} cells. *P* values were determined by two-tailed Fisher's exact test ($n = 292{,}033/2{,}064$ DMRs/peaks 'closer to skin T_{reg}', 6,424/1,128 DMRs/peaks 'closer to blood $CD45RA^+$ T_{reg}'). **g**, Methylation of TE insertion sites overlapping with regions hypomethylated in skin T_{reg} cells (with median) in skin T_{reg}, blood $CCR8^+$ T_{reg} and blood $CD45RA^+$ T_{reg} cells (top; three donors per cell type; Tissue Donors 7, 10 and 11 and Blood Donors 3–8) and distribution of differences in mean methylation (across the three donors) between any two cell types for each insertion site (bottom). Numbers indicate how many insertion sites displayed differences below and above 0. Data are representative of two or more independent experiments with two or more individual donors.

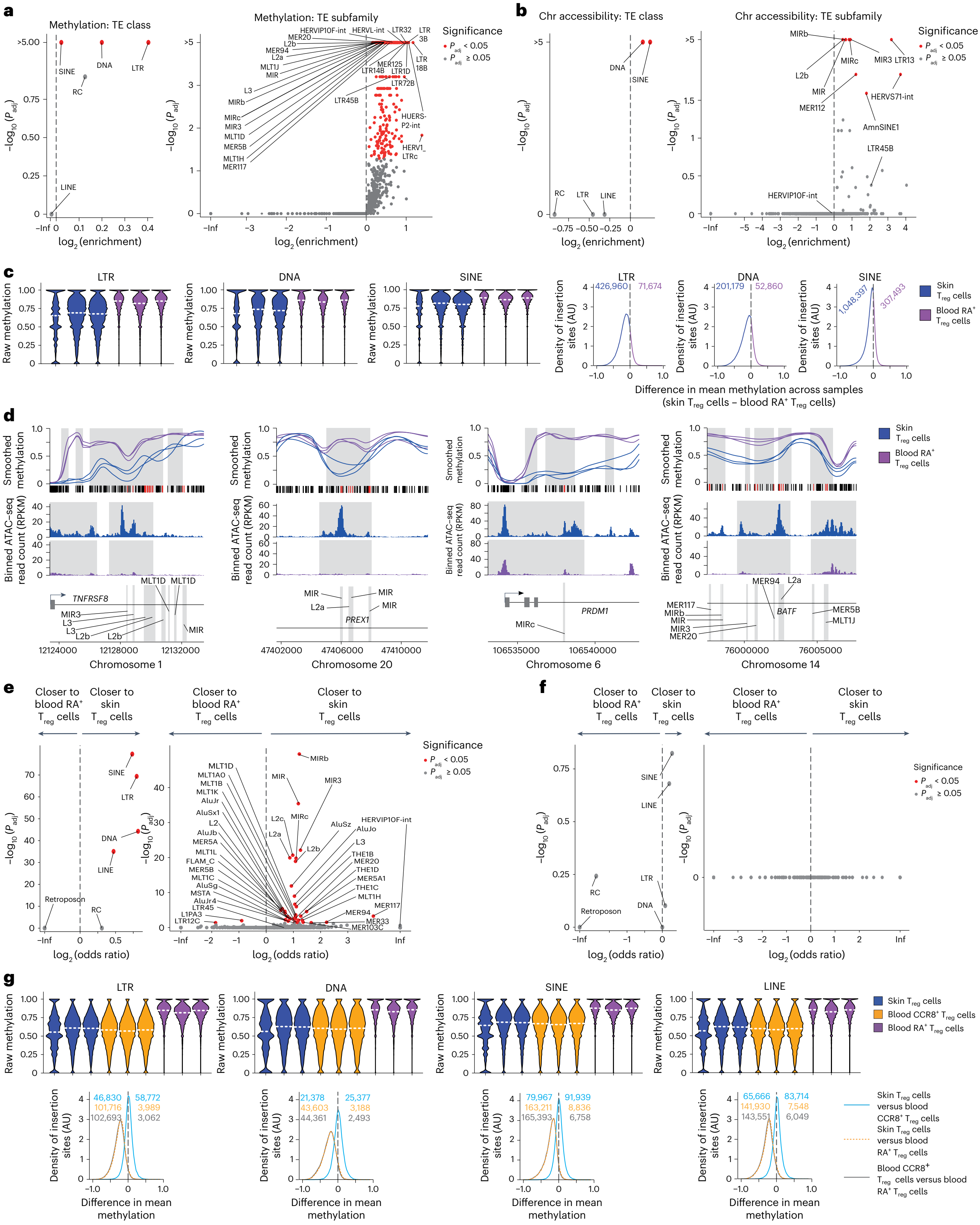
a
Methylation: TE class
Methylation: TE subfamily
Significance
P_{adj} < 0.05
P_{adj} ≥ 0.05
SINE
DNA
LTR
RC
LINE
$-\log_{10}(P_{adj})$
$\log_2$(enrichment)
HERVIP10F-int
HERVL-int
LTR32
LTR 3B
MER20
L2b
MER94
L2a
MLT1J
MIR
L3
MIRb
MIRc
MIR3
MLT1D
MER5B
MLT1H
MER117
MER125
LTR14B
LTR1D
LTR 18B
LTR72B
LTR45B
HUERS-P2-int
HERV1_LTRc
b
Chr accessibility: TE class
Chr accessibility: TE subfamily
MIRb
L2b
MIRc
MIR
MER112
MIR3
LTR13
HERVS71-int
AmnSINE1
LTR45B
HERVIP10F-int
c
LTR
DNA
SINE
Raw methylation
Density of insertion sites (AU)
426,960
71,674
201,179
52,860
1,048,397
307,493
Difference in mean methylation across samples (skin T_{reg} cells – blood RA$^+$ T_{reg} cells)
Skin T_{reg} cells
Blood RA$^+$ T_{reg} cells
d
Smoothed methylation
Binned ATAC-seq read count (RPKM)
TNFRSF8
MIR3
L3
L3
L2b
L2b
MLT1D
MLT1D
MIR
12124000
12128000
12132000
Chromosome 1
MIR
L2a
MIR
MIR
PREX1
47402000
47406000
47410000
Chromosome 20
PRDM1
MIRc
106535000
106540000
Chromosome 6
MER94
L2a
MER117
MIRb
MIR
MIR3
MER20
BATF
MER5B
MLT1J
76000000
76005000
Chromosome 14
e
Closer to blood RA$^+$ T_{reg} cells
Closer to skin T_{reg} cells
SINE
LTR
DNA
LINE
Retroposon
RC
MIRb
MIR
MIR3
MLT1D
MLT1A0
MLT1B
MLT1K
AluJr
AluSx1
L2
AluJb
MER5A
MLT1L
FLAM_C
MER5B
MLT1C
AluSg
MSTA
AluJr4
LTR45
L1PA3
LTR12C
L2c
MIRc
L2a
L2b
AluSz
HERVIP10F-int
AluJo
L3
THE1B
MER20
THE1D
MER5A1
THE1C
MLT1H
MER117
MER94
MER33
MER103C
$\log_2$(odds ratio)
f
SINE
LINE
RC
Retroposon
LTR
DNA
g
LTR
DNA
SINE
LINE
Skin T_{reg} cells
Blood CCR8$^+$ T_{reg} cells
Blood RA$^+$ T_{reg} cells
46,830
101,716
102,693
58,772
3,989
3,062
21,378
43,603
44,361
25,377
3,188
2,493
79,967
163,211
165,393
91,939
8,836
6,758
65,666
141,930
143,551
83,714
7,548
6,049
Difference in mean methylation
Skin T_{reg} cells versus blood CCR8$^+$ T_{reg} cells
Skin T_{reg} cells versus blood RA$^+$ T_{reg} cells
Blood CCR8$^+$ T_{reg} cells versus blood RA$^+$ T_{reg} cells

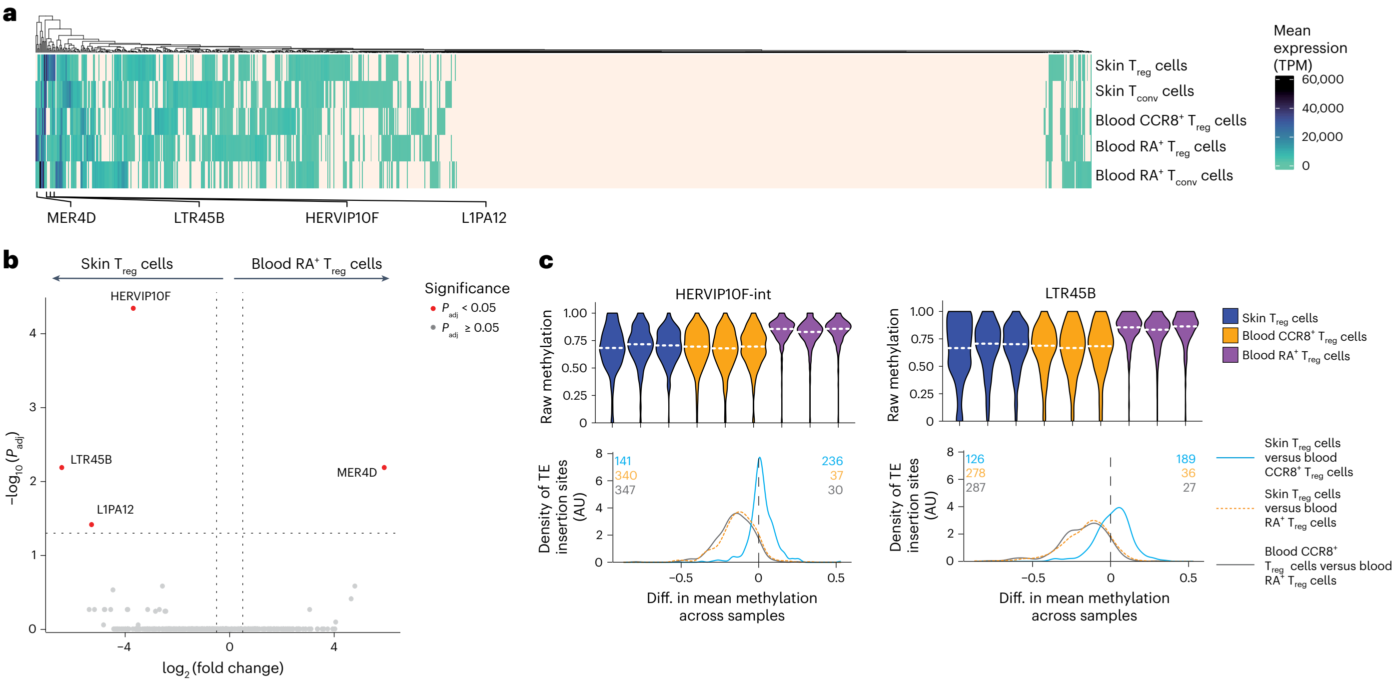

Fig. 7 | Several TE subfamilies are transcribed in skin T_{reg} cells. a, Expression levels of TE subfamilies in skin T_{reg}, skin T_{conv}, blood CCR8⁺ T_{reg}, blood CD45RA⁺ T_{reg} (blood RA⁺ T_{reg}) and blood CD45RA⁺ T_{conv} (blood RA⁺ T_{conv}) cells with within-cell-type mean based on 4, 4, 5, 5 and 3 donors, respectively (Tissue Donors 7, 8, 10 and 11 and Blood Donors 3–12). Values equal to 0 are shown in light beige. TPM normalization reflects the expression level of a particular TE compared to the whole collection of TEs. **b**, Differential expression of TE subfamilies between skin T_{reg} cells and blood CD45RA⁺ T_{reg} cells. *P* values were determined by two-tailed Wald test implemented in DESeq2 (skin T_{reg} cell donors, $n = 4$; blood CD45RA⁺ T_{reg} cell donors, $n = 5$; donors are as in **a**) with a Benjamini–Hochberg correction. **c**, Methylation of annotated HERVIP10F-int and LTR45B insertion sites (with median) in skin T_{reg}, blood CCR8⁺ T_{reg} and blood CD45RA⁺ T_{reg} cells (top; $n = 3$ donors per cell type; Tissue Donors 7, 10 and 11 and Blood Donors 3–8) and distribution of differences in mean methylation (across the three donors) between any two cell types for each insertion site (bottom). Numbers indicate how many insertion sites displayed differences below and above 0.

photoconverted Kaede-red⁺ T_{reg} cells expressed CCR8 in the dLNs, whereas only 30% of nonconverted Kaede-green⁺ T_{reg} cells expressed CCR8 (Fig. 5h,i and Extended Data Fig. 8h), indicating that the CCR8⁺ T_{reg} cell pool is enriched for tissue egressing, recirculating T_{reg} cells. These results showed a higher conservation of skin T_{reg} cell methylation traits in blood CCR8⁺ T_{reg} cells than DNA accessibility and gene expression traits and suggested that blood CCR8⁺ T_{reg} cells could represent recirculating tissue T_{reg} cells that lost part of their accessibility and gene expression tissue characteristics.

TE hypomethylation characterizes tissue T_{reg} cells

TEs contribute to gene regulatory functions, and DNA methylation suppresses their activity[28,35,36]. TE elements can be subdivided into classes (including long interspersed nuclear elements (LINEs), long terminal repeats (LTRs), short interspersed nuclear elements (SINEs) and DNA elements) and further into families and subfamilies (Supplementary Table 7). In total, more than 1,100 TE subfamilies can be distinguished with individual integration sites, ranging from a few dozen integration sites to more than 100,000 integrations per subfamily[37–39]. We asked which TE classes and subfamilies were enriched in epigenetically differential regions of skin T_{reg} cells versus blood CD45RA⁺ T_{reg} cells. We found that the TE classes SINE, LTR and DNA as well as 323 TE subfamilies, including LTR18B, HUERS-P2-int, LTR3B, LTR1D, LTR32 and MER125, were significantly enriched in 'skin T_{reg} cell hypomethylation' DMRs compared to the TE distribution expected by chance (Fig. 6a, Extended Data Fig. 9a and Supplementary Table 8). Significant TE enrichment was also detected at the accessibility level in skin T_{reg} cells (Fig. 6b and Extended Data Fig. 9b). We also directly examined methylation and accessibility around annotated TE insertion sites in skin T_{reg} and blood CD45RA⁺ T_{reg} cells. LTR, SINE and DNA TEs were strongly affected by hypomethylation changes in skin T_{reg} cells (Fig. 6c). In all three TE classes, more TE insertion sites were hypomethylated in skin T_{reg} cells than in blood CD45RA⁺ T_{reg} cells, for example, 86% for LTR class TE insertion sites (Fig. 6c and Extended Data Fig. 9c). Similar hypomethylation patterns were also observed in subcutaneous adipose tissue T_{reg} cells (Extended Data Fig. 9d). Skin T_{reg} cell signature genes, such as *TNFRSF8*, *PREX1*, *PRDM1* and *BATF*, contained hypomethylated TE insertion sites for several TE subfamilies, such as MIR and L2a (Fig. 6d and Extended Data Fig. 9e).

Next, we investigated the TE traits of blood CCR8⁺ T_{reg} cells compared to skin T_{reg} and blood CD45RA⁺ T_{reg} cells. DMRs and differential peaks were stratified based on their positioning of blood CCR8⁺ T_{reg} cells, and we examined whether TEs were enriched among the stratified features. SINE, LINE, LTR and DNA TE classes and 38 individual TE subfamilies, including MIR and L2a, were enriched in DMRs that placed blood CCR8⁺ T_{reg} cells closer to skin T_{reg} cells (Fig. 6e). We did not observe any significant TE enrichment at the accessibility level (Fig. 6f), suggesting that TE-related traits in blood CCR8⁺ T_{reg} cells reflected skin T_{reg} cell traits at the methylation, but not chromatin accessibility, level. Because TE enrichments may have been biased by different underlying region numbers, we also examined methylation around individual TE insertion sites. The hypomethylation pattern in LTR, SINE, LINE and DNA TEs in CCR8⁺ T_{reg} cells, but not the hyperaccessibility pattern, was almost indistinguishable from the pattern of skin T_{reg} cells compared to blood CD45RA⁺ T_{reg} cells (Fig. 6g and Extended Data Fig. 9f). These findings indicate that TEs represent an integral constituent of the hypomethylation landscape in tissue T_{reg} cells and that blood CCR8⁺ T_{reg} cells conserve the TE hypomethylation traits found in tissue T_{reg} cells.

TE subfamilies gain RNA expression in skin T_{reg} cells

Because TEs can be transcribed into RNA[23], we investigated how epigenetic methylation changes of TE insertion sites influenced

Table 1 | Locations and methylation of the most strongly hypomethylated HERVIP10F-int and LTR45B insertion sites overlapping with DMRs hypomethylated in skin T_{reg} cells

Chr.	Interval	Meth. blood RA^+ T_{reg} cells	Meth. skin T_{reg} cells	Meth. diff.
HERVIP10F-int				
4	141519736–141521252	0.860	0.477	−0.383
11	92994750–92995433	0.828	0.542	−0.370
14	21193203–21193472	0.903	0.542	−0.361
2	132899525–132902896	0.857	0.505	−0.352
11	67456726–67457160	0.749	0.400	−0.349
LTR45B				
4	107573927–107573965	1.000	0.254	−0.746
10	33423433–33423859	0.664	0.100	−0.564
12	106417286–106417799	0.758	0.200	−0.558
20	13999437–13999668	0.719	0.167	−0.552
11	5612894–5613203	0.792	0.317	−0.475

Methylation values correspond to the mean across three donors (Tissue Donors 7, 10 and 11 and Blood Donors 3–5). Chr.; chromosome; Diff., difference; Meth., Methylation; RA, CD45RA.

TE expression during skin T_{reg} cell tissue adaptation. We matched RNA-based sequencing reads to TE consensus sequences and quantified the expression of TEs in the bulk RNA-seq data[10]. TEs inserted into larger transcribed regions (genes) can bias this analysis because their expression might be due to transcription of the larger region and not expression of the TE. To avoid such biases, we excluded TE reads that mapped to gene bodies or long noncoding RNAs (lncRNAs). We detected a median number of 1,071 (range: 625–1,561) TE-derived reads across the analyzed samples (Supplementary Table 9). Of 1,103 profiled TEs, 613 displayed detectable expression in at least one cell type (skin T_{reg}, skin T_{conv}, blood CD45RA$^+$ T_{reg}, CD45RA$^+$ T_{conv} and CCR8$^+$ T_{reg} cells; Fig. 7a and Supplementary Table 9). Analysis of TEs that changed transcription during skin T_{reg} cell tissue adaptation identified three TEs that were overexpressed in skin T_{reg} cells compared to in blood CD45RA$^+$ T_{reg} cells (Fig. 7b), including the TE subfamilies HERVIP10F (labeled 'HERVIP10F-int' in the insertion site database) and LTR45B. The insertion sites of HERVIP10F and LTR45B were hypomethylated in skin and subcutaneous fat T_{reg} cells (Fig. 7c and Extended Data Fig. 10a,b). Blood CCR8$^+$ T_{reg} cells reflected this trend (Fig. 7c). We identified 103 HERVIP10F-int and 72 LRT45B insertion sites that overlapped with 'skin T_{reg} cell hypomethylation' DMRs (Supplementary Table 10). The most strongly hypomethylated insertion sites included a position on chromosome 4, with 74% methylation reduction in skin T_{reg} cells compared to blood CD45RA$^+$ T_{reg} cells (Table 1). Thus, the TE landscape is an integral part of the hypomethylation traits of tissue T_{reg} cells, shared by circulating CCR8$^+$ T_{reg} cells.

Discussion

Based on epigenetic DNA analyses, we identified tissue adaptation programs, often involving specific TE subfamilies, in human tissue T_{reg} cells. We found that CCR8$^+$ circulating blood T_{reg} cells shared a strong epigenetic relationship with tissue T_{reg} cells, characterized by a similar hypomethylation pattern, while they differed in their chromatin accessibility and RNA expression profile. This indicated that CCR8$^+$ T_{reg} cells in the blood contained recirculating tissue T_{reg} cells showing signs of a reversal of the tissue adaptation program toward a more naive phenotype.

In mice, T_{reg} cells are characterized by DNA hypomethylated T_{reg} cell signature genes, which are essential for T_{reg} cell functionality, long-term lineage stability[1] and tissue-specific functional adaptations[3,4,7,10]. Here, we described about 300,000 DMRs between human skin tissue T_{reg} cells and naive CD45RA$^+$ blood T_{reg} cells. The sheer number of methylation changes, which we also found in subcutaneous adipose T_{reg} cells, indicates that T_{reg} cell tissue adaptation goes along with marked epigenetic reconfiguration. Notably, tissue adaptation programs were dominated by hypomethylation changes. Dominance of hypomethylation was reported for developing lymphocytes and immune cell proliferation[40], which has been attributed in part to specific late-replicating regions called 'partially methylated domains'[41,42].

TEs can influence immunological processes by providing an enhancer landscape[39,43]. Reactivated TE RNA or DNA can be sensed by the innate immune system, resulting in pathological inflammation[44,45]. Research into how TEs affect gene regulation by influencing the enhancer landscape in immune cells is just emerging. It was reported that interferon responses rely on TE co-option[46], and CD8$^+$ T cell activation exploits the TE enhancer architecture[47]. Specific TE families were reported to be associated with tissue adaptation of immune cells[38]. Here, we found similar patterns in human skin and subcutaneous adipose T_{reg} cells. We found TE RNA, which was indicative of the reactivation of TE subfamilies, associated with hypomethylation of TE insertion sites in skin tissue T_{reg} cells.

Our data showed a strong relationship between human circulating CCR8$^+$ T_{reg} cells and tissue T_{reg} cells, suggesting that blood CCR8$^+$ T_{reg} cells are the recirculating counterpart of tissue T_{reg} cells. Using cell tracking in mice, we found that dLN CCR8$^+$ T_{reg} cells contained skin recirculating tissue T_{reg} cells. Therefore, blood CCR8$^+$ T_{reg} cells could become a valuable diagnostic tool, as these cells may have witnessed alterations in a tissue, such as an imminent immune rejection in a transplant situation. The strong epigenetic relationship observed in the methylation data was only partly recapitulated by chromatin accessibility traits, suggesting that methylation changes are a more permanent trait than chromatin accessibility, as previously reported[48]. A recirculating population of human tissue T_{reg} cells would not be unexpected, as data in mice point in this direction[49]. Mouse parabiosis experiments suggested that depending on the tissue, the mean dwell time of tissue T_{reg} cells within a certain tissue is 2–8 weeks (ref. 49), and work on mouse muscle T_{reg} cells showed shared muscle T_{reg} cell TCR sequences in a specific spleen T_{reg} cell population, compatible with recirculating muscle T_{reg} cells[12]. Our multiomic analysis indicated that recirculating tissue T_{reg} cells show signs of a regression of the tissue adaptation program toward a more naive state, resembling a precursor-like phenotype, making the distinction between true precursor tissue T_{reg} cells that never entered the tissue and egressing tissue T_{reg} cells difficult. The precursor-like phenotype may allow circulating tissue T_{reg} cells to better readapt to new challenges, while maintaining certain methylation traits that could enforce a more pan-tissue T_{reg} cell identity. The existence of a pan-tissue T_{reg} cell identity across various organs and even between human and mouse tissue T_{reg} cells has been reported[3,4,7,10,49]. In conclusion, our data provide insights into the tissue adaptation of human tissue T_{reg} cells, which may have important implications for therapeutic applications of T_{reg} cells and disease diagnostics.

Online content

Any methods, additional references, Nature Portfolio reporting summaries, source data, extended data, supplementary information, acknowledgements, peer review information; details of author contributions and competing interests; and statements of data and code availability are available at https://doi.org/10.1038/s41590-025-02210-x.

References

1. Ohkura, N. et al. T cell receptor stimulation-induced epigenetic changes and Foxp3 expression are independent and complementary events required for T_{reg} cell development. *Immunity* **37**, 785–799 (2012).
2. Dikiy, S. & Rudensky, A. Y. Principles of regulatory T cell function. *Immunity* **56**, 240–255 (2023).

3. Delacher, M. et al. Genome-wide DNA-methylation landscape defines specialization of regulatory T cells in tissues. *Nat. Immunol.* **18**, 1160–1172 (2017).
4. Delacher, M. et al. Precursors for nonlymphoid-tissue T_{reg} cells reside in secondary lymphoid organs and are programmed by the transcription factor BATF. *Immunity* **52**, 295–312 (2020).
5. Munoz-Rojas, A. R. & Mathis, D. Tissue regulatory T cells: regulatory chameleons. *Nat. Rev. Immunol.* **21**, 597–611 (2021).
6. Miragaia, R. J. et al. Single-cell transcriptomics of regulatory T cells reveals trajectories of tissue adaptation. *Immunity* **50**, 493–504 (2019).
7. DiSpirito, J. R. et al. Molecular diversification of regulatory T cells in nonlymphoid tissues. *Sci. Immunol.* **3**, eaat5861 (2018).
8. Feuerer, M. et al. Lean, but not obese, fat is enriched for a unique population of regulatory T cells that affect metabolic parameters. *Nat. Med.* **15**, 930–939 (2009).
9. Cipolletta, D. et al. PPAR-γ is a major driver of the accumulation and phenotype of adipose tissue T_{reg} cells. *Nature* **486**, 549–553 (2012).
10. Delacher, M. et al. Single-cell chromatin accessibility landscape identifies tissue repair program in human regulatory T cells. *Immunity* **54**, 702–720 (2021).
11. Ali, N. et al. Regulatory T cells in skin facilitate epithelial stem cell differentiation. *Cell* **169**, 1119–1129 (2017).
12. Burzyn, D. et al. A special population of regulatory T cells potentiates muscle repair. *Cell* **155**, 1282–1295 (2013).
13. Arpaia, N. et al. A distinct function of regulatory T cells in tissue protection. *Cell* **162**, 1078–1089 (2015).
14. Ito, M. et al. Brain regulatory T cells suppress astrogliosis and potentiate neurological recovery. *Nature* **565**, 246–250 (2019).
15. Sakai, R. et al. Kidney GATA3$^+$ regulatory T cells play roles in the convalescence stage after antibody-mediated renal injury. *Cell Mol. Immunol.* **18**, 1249–1261 (2021).
16. Li, C. et al. TCR transgenic mice reveal stepwise, multi-site acquisition of the distinctive fat-T_{reg} phenotype. *Cell* **174**, 285–299 (2018).
17. Vasanthakumar, A. et al. The transcriptional regulators IRF4, BATF and IL-33 orchestrate development and maintenance of adipose tissue-resident regulatory T cells. *Nat. Immunol.* **16**, 276–285 (2015).
18. Hayatsu, N. et al. Analyses of a mutant *Foxp3* allele reveal BATF as a critical transcription factor in the differentiation and accumulation of tissue regulatory T cells. *Immunity* **47**, 268–283 (2017).
19. Azizi, E. et al. Single-cell map of diverse immune phenotypes in the breast tumor microenvironment. *Cell* **174**, 1293–1308 (2018).
20. Plitas, G. et al. Regulatory T cells exhibit distinct features in human breast cancer. *Immunity* **45**, 1122–1134 (2016).
21. Wang, L. et al. Connecting blood and intratumoral T_{reg} cell activity in predicting future relapse in breast cancer. *Nat. Immunol.* **20**, 1220–1230 (2019).
22. Cordaux, R. & Batzer, M. A. The impact of retrotransposons on human genome evolution. *Nat. Rev. Genet.* **10**, 691–703 (2009).
23. Giassa, I.-C. & Alexiou, P. Bioinformatics and machine learning approaches to understand the regulation of mobile genetic elements. *Biology* **10**, 896 (2021).
24. Mills, R. E., Bennett, E. A., Iskow, R. C. & Devine, S. E. Which transposable elements are active in the human genome? *Trends Genet.* **23**, 183–191 (2007).
25. Lander, E. S. et al. Initial sequencing and analysis of the human genome. *Nature* **409**, 860–921 (2001).
26. Bruno, M., Mahgoub, M. & Macfarlan, T. S. The arms race between KRAB-zinc finger proteins and endogenous retroelements and its impact on mammals. *Annu. Rev. Genet.* **53**, 393–416 (2019).
27. Ali, A., Han, K. & Liang, P. Role of transposable elements in gene regulation in the human genome. *Life* **11**, 118 (2021).
28. Fueyo, R., Judd, J., Feschotte, C. & Wysocka, J. Roles of transposable elements in the regulation of mammalian transcription. *Nat. Rev. Mol. Cell Biol.* **23**, 481–497 (2022).
29. Gebrie, A. Transposable elements as essential elements in the control of gene expression. *Mob. DNA* **14**, 9 (2023).
30. Liberzon, A. et al. The Molecular Signatures Database (MSigDB) hallmark gene set collection. *Cell Syst.* **1**, 417–425 (2015).
31. Heinz, S. et al. Simple combinations of lineage-determining transcription factors prime *cis*-regulatory elements required for macrophage and B cell identities. *Mol. Cell* **38**, 576–589 (2010).
32. Encode Project Consortium. An integrated encyclopedia of DNA elements in the human genome. *Nature* **489**, 57–74 (2012).
33. Tomura, M. et al. Monitoring cellular movement in vivo with photoconvertible fluorescence protein 'Kaede' transgenic mice. *Proc. Natl Acad. Sci. USA* **105**, 10871–10876 (2008).
34. Tomura, M. et al. Activated regulatory T cells are the major T cell type emigrating from the skin during a cutaneous immune response in mice. *J. Clin. Invest.* **120**, 883–893 (2010).
35. Zhou, W., Liang, G., Molloy, P. L. & Jones, P. A. DNA methylation enables transposable element-driven genome expansion. *Proc. Natl Acad. Sci. USA* **117**, 19359–19366 (2020).
36. Wells, J. N. & Feschotte, C. A field guide to eukaryotic transposable elements. *Annu. Rev. Genet.* **54**, 539–561 (2020).
37. Kojima, S. et al. Mobile element variation contributes to population-specific genome diversification, gene regulation and disease risk. *Nat. Genet.* **55**, 939–951 (2023).
38. Simon, M. et al. Single-cell chromatin accessibility and transposable element landscapes reveal shared features of tissue-residing immune cells. *Immunity* **57**, 1975–1993 (2024).
39. Schmidleithner, L., Stuve, P. & Feuerer, M. Transposable elements as instructors of the immune system. *Nat. Rev. Immunol.* https://doi.org/10.1038/s41577-025-01172-3 (2025).
40. Schuyler, R. P. et al. Distinct trends of DNA methylation patterning in the innate and adaptive immune systems. *Cell Rep.* **17**, 2101–2111 (2016).
41. Zhou, W. et al. DNA methylation loss in late-replicating domains is linked to mitotic cell division. *Nat. Genet.* **50**, 591–602 (2018).
42. Endicott, J. L., Nolte, P. A., Shen, H. & Laird, P. W. Cell division drives DNA methylation loss in late-replicating domains in primary human cells. *Nat. Commun.* **13**, 6659 (2022).
43. Bourque, G. et al. Ten things you should know about transposable elements. *Genome Biol.* **19**, 199 (2018).
44. De Cecco, M. et al. L1 drives IFN in senescent cells and promotes age-associated inflammation. *Nature* **566**, 73–78 (2019).
45. Simon, M. et al. LINE1 derepression in aged wild-type and SIRT6-deficient mice drives inflammation. *Cell Metab.* **29**, 871–885 (2019).
46. Chuong, E. B., Elde, N. C. & Feschotte, C. Regulatory evolution of innate immunity through co-option of endogenous retroviruses. *Science* **351**, 1083–1087 (2016).
47. Ye, M. et al. Specific subfamilies of transposable elements contribute to different domains of T lymphocyte enhancers. *Proc. Natl Acad. Sci. USA* **117**, 7905–7916 (2020).
48. Barnett, K. R. et al. ATAC-Me captures prolonged DNA methylation of dynamic chromatin accessibility loci during cell fate transitions. *Mol. Cell* **77**, 1350–1364 (2020).
49. Burton, O. T. et al. The tissue-resident regulatory T cell pool is shaped by transient multi-tissue migration and a conserved residency program. *Immunity* **57**, 1586–1602 (2024).

Niklas Beumer [1,2,3,22], Charles D. Imbusch [1,2,4,22], Tamara Kaufmann [1,2,22], Lisa Schmidleithner[5,6], Kathrin Gütter[5,6], Philipp Stüve[5,6], Harriet Marchel [5,6], Dieter Weichenhan[7], Marion Bähr[7], Brigitte Ruhland[5,6], Federico Marini [2,8], Lieke Sanderink[5,6], Uwe Ritter[5,6], Malte Simon[3,4,5,21], Kathrin Luise Braband [1,2], Morten Michael Voss[1,2], Sara Salome Helbich[1,2], Delia Mihaela Mihoc[1,2], Agnes Hotz-Wagenblatt[9], Hadrian Nassabi[10], Andreas Eigenberger[11], Lukas Prantl[11], Claudia Gebhard[5], Michael Rehli [5,12], Nicholas Strieder [5], Kartikeya Singh[13], Christian Schmidl[5], Christoph Plass[7], Jochen Huehn [14,15], Thomas Hehlgans[5,6], Julia K. Polansky [16,17], Benedikt Brors [4,18,19,20,23], Michael Delacher [1,2,23] ✉ & Markus Feuerer [5,6,23] ✉

[1]Institute of Immunology, University Medical Center Mainz, Mainz, Germany. [2]Research Center for Immunotherapy, University Medical Center Mainz, Mainz, Germany. [3]Faculty of Biosciences, Heidelberg University, Heidelberg, Germany. [4]Division of Applied Bioinformatics, German Cancer Research Center (DKFZ), Heidelberg, Germany. [5]Leibniz Institute for Immunotherapy, Regensburg, Germany. [6]Chair for Immunology, University Regensburg, Regensburg, Germany. [7]Division of Cancer Epigenomics, German Cancer Research Center (DKFZ), Heidelberg, Germany. [8]Institute of Medical Biostatistics, Epidemiology and Informatics (IMBEI), University Medical Center Mainz, Mainz, Germany. [9]Core Facility Omics IT and Data Management (ODCF), German Cancer Research Center (DKFZ), Heidelberg, Germany. [10]Department of Dermatology, University Medical Center of the Johannes Gutenberg University, Mainz, Germany. [11]Department of Plastic, Hand and Reconstructive Surgery, University Hospital Regensburg, Regensburg, Germany. [12]Department of Internal Medicine III, University Hospital Regensburg, Regensburg, Germany. [13]Institute of Computational Biology, Helmholtz Munich, Munich, Germany. [14]Department of Experimental Immunology, Helmholtz Centre for Infection Research, Braunschweig, Germany. [15]RESIST, Cluster of Excellence 2155, Hannover Medical School, Hannover, Germany. [16]Immuno-Epigenetics, Berlin Institute of Health Center for Regenerative Therapies at Charité Universitätsmedizin Berlin, Berlin, Germany. [17]Immuno-Epigenetics, German Rheumatism Research Centre, Berlin, Germany. [18]National Center for Tumor Diseases (NCT), Heidelberg, Germany. [19]German Cancer Consortium (DKTK), German Cancer Research Center (DKFZ), Heidelberg, Germany. [20]Medical Faculty Heidelberg and Faculty of Biosciences, Heidelberg University, Heidelberg, Germany. [21]Present address: Evotec SE, Hamburg, Germany. [22]These authors contributed equally: Niklas Beumer, Charles D. Imbusch, Tamara Kaufmann. [23]These authors jointly supervised this work: Benedikt Brors, Michael Delacher, Markus Feuerer. ✉e-mail: delacher@uni-mainz.de; markus.feuerer@ukr.de

Methods

Human donors, sample acquisition, sample sizes and ethics

Human skin and subcutaneous adipose (fat) tissue used for whole-genome bisulfite sequencing and RNA-seq was obtained from seven healthy female donors (named Tissue Donors 5–11) undergoing abdominoplasty procedures after weight loss or epigastric hernia repair after multiple pregnancy. For whole-genome bisulfite sequencing, samples from three donors per cell type were processed. We analyzed skin T_{reg} cells from Tissue Donors 7, 10 and 11 (median age: 52 years; range: 41–53 years), skin T_{conv} cells from Tissue Donors 7, 10 and 11 (ages as for skin T_{reg} cells) and fat T_{reg} cells from Tissue Donors 6, 7 and 8 (age not available for each donor). For bulk RNA-seq, we profiled samples from four to five donors per cell type. We analyzed skin T_{reg} cells from Tissue Donors 7, 8, 10 and 11 (age not available for each donor), skin T_{conv} cells from Tissue Donors 7, 8, 10 and 11 (age not available for each donor) and fat T_{reg} cells from Tissue Donors 5, 6, 7, 8 and 9 (age not available for each donor). These bulk RNA-seq data have been published previously[10]. For flow cytometry analysis, blood and skin samples were obtained from seven healthy female donors undergoing abdominoplasty procedures after weight loss and epigastric hernia repair. For statistical analysis, we used samples from FACS Donors 1–6 (median age: 46 years; range: 31–61 years). For exemplification of our gating strategy, we used samples from FACS Donor 7 (age unknown). Collection of tissue, immune cells and blood samples from these donors was performed in accordance with the Declaration of Helsinki after ethical approval by the local ethics committee at Regensburg University, Germany (reference number 19-1453-101), and signed informed consent.

To obtain human blood samples for whole-genome bisulfite sequencing and RNA-seq, peripheral blood mononuclear cells for CD4$^+$ T cell enrichment were isolated from leukocyte reduction chambers from ten healthy female donors of unknown age who donated thrombocytes (termed Blood Donors 3–12). For whole-genome bisulfite sequencing, samples from three donors per cell type were used (blood CD45RA$^+$ T_{reg} cells from Blood Donors 3–5, blood CD45RA$^+$ T_{conv} cells from Blood Donors 3–5 and blood CCR8$^+$ T_{reg} cells from Blood Donors 6–8). For bulk RNA-seq, we profiled three to five samples per cell type (blood CD45RA$^+$ T_{reg} cells from Blood Donors 3–5, 9 and 10, blood CD45RA$^+$ T_{conv} cells from Blood Donors 3–5 and blood CCR8$^+$ T_{reg} cells from Blood Donors 6–8, 11 and 12). These bulk RNA-seq data have been previously published[10]. For CRISPR activation, we analyzed T cells from six donors of unknown sex and age. Cells from CRISPR Donors 1–3 were used for the guide RNAs hMLPH_A and hGNA11, and cells from CRISPR Donors 4–6 were used for the guide RNA hMLPH_B. For amplicon-based bisulfite sequencing, we processed samples from six male donors of unknown age. These donors were termed 'Amplicon Donors 1–6'. Collection of blood samples was performed in compliance with the Declaration of Helsinki after ethical approval by the local ethical committee (reference numbers 19-1414-101 and 19-1614-101) and signed informed consent. Donors provided written informed consent, and their samples were not used for any other analyses in this study.

No statistical methods were used to predetermine sample sizes, but our sample sizes are similar to those reported in previous publications[50]. Donors were not assigned to different experimental groups, and no randomization was performed. Data collection and analysis were not performed blind to the conditions of the experiments.

In addition, we used public scATAC-seq and scRNA-seq/scTCR-seq data[10]. scATAC-seq data contained data on CD4$^+$ T cells from blood, skin and subcutaneous fat from five healthy female donors (blood from ATAC Donors 1 and 2, skin from ATAC Donors 4 and 5 and fat from ATAC Donors 3–5) with an average age of 44.6 years (±14; range from 26 to 56 years, ages for individual donors unknown) undergoing abdominoplasty procedures after weight loss and epigastric hernia repair. scRNA-seq/scTCR-seq data contained data on CD4$^+$ T cells from blood, skin and subcutaneous fat from two healthy female donors (termed TCR Donors 6 and 7) of unknown age who underwent abdominoplasty procedures after weight loss and epigastric hernia repair. Collection of tissue, immune cells and blood samples from these donors was performed in accordance with the Declaration of Helsinki after ethical approval by the local ethics committee at Regensburg University, Germany (reference number 19-1453-101), and signed informed consent.

All animal experiments were approved by the governmental committee for animal experimentation (Regierungspräsidium Unterfranken) and were conducted in accordance with ethical regulations. Specific details on animal characteristics are provided in a dedicated section below.

Tissue digestion for flow cytometry and FACS of T cells

To isolate T cells from human skin tissue, skin and underlying fat were first mechanically separated. The skin was then cut into small pieces and digested (base medium DMEM (Gibco, 41965), 4 mg ml^{-1} collagenase type IV (Sigma-Aldrich, C5138), 10 µg ml^{-1} DNase I (Roche, 11284932001), 2% fetal bovine serum and 10 mM HEPES). Digestion was performed directly in a GentleMACS C tube with the program '37_C_Multi_H' for 90 min, followed by centrifugation and filtration steps. Dead cell removal was performed with a dead cell removal kit (Miltenyi, 130-090-101).

Peripheral blood mononuclear cell isolation and pre-enrichment of blood lymphocytes

To isolate T cells from human blood, leukocyte reduction chambers or buffy coats were used. Leukocytes were first diluted 1:3 with DPBS (Gibco, 14190-094), and the resulting blood and PBS mixture was split into two fractions and underlaid with an equal amount of Pancoll (PAN-Biotech, P04-601000). Samples were centrifuged at 1,000*g* for 20 min at room temperature, with acceleration set to 4 and brake to 0. The peripheral blood mononuclear cell layer was isolated and washed twice by centrifugation. Antibodies were used, if not indicated otherwise, as recommended by the manufacturer (including amounts and dilutions). Cells were pre-enriched with biotinylated anti-human CD4 (clone OKT4, Biolegend, 317406), biotinylated anti-human CD8 (clone HIT8a, Biolegend, 300904) or PE-labeled or biotinylated anti-human CD25 (clone BC96, Biolegend, 302606 or 302624) at a dilution of 1:20 or 1:100, followed by column-based magnetic separation with anti-biotin or anti-PE ultrapure microbeads (Miltenyi Biotec, 130-105-637 or 130-105-639) following the manufacturer's protocol. All antibodies were from commercial sources and were validated by the manufacturer.

Preparation of samples for FACS

T cells were isolated and pre-enriched as described in the previous sections. Cells were stained in 1.5-ml Eppendorf tubes or 96-well plates in FACS buffer (2% fetal calf serum in PBS). Surface staining was performed at 4 °C for 20 min in a staining volume of 50–100 µl. Antibodies were used, if not indicated otherwise, as recommended by the manufacturer (including amounts and dilutions). All antibodies were from commercial sources and were validated by the manufacturer. The following antibodies were used for surface staining: anti-human CD3-BV785 (OKT3, Biolegend, 317330 or BD Biosciences, 566782), anti-human CD4-BV711 (OKT4/L200, Biolegend, 317440 or BD Biosciences, 563913), anti-human TCR-β-chain BV785 (IP26, Biolegend, 306742), anti-human CD8-BUV395 (RPA-T8, BD Biosciences, 563795), anti-human CD19-BV605 (HIB19, Biolegend, 302244), anti-human CD25-PE (BC96/2A3, Biolegend, 302606 or BD Biosciences, 57214), anti-human CD45-BUV737 (HI30, BD Biosciences, 748719), anti-human CD45RA-BV605 or CD45RA-BV510 (HI100, Biolegend, 304134/304142 or BD Biosciences, 562886), anti-human CD45RO-BV421 (UCHL1, Biolegend, 304224), anti-human CD127-APC (A019D5, Biolegend, 351342), anti-human CD14 BUV395 (MφP9, BD Biosciences, 563562) and anti-human CCR8-BV421 or BUV395 (433H, BD Biosciences, or 747573) at a dilution of 1:20 or 1:100. Viability staining was performed using eBioscience Fixable Viability Dye eFluor 780 (Thermo Fisher Scientific, 65-0865-14) according to manufacturer's instructions at a dilution of 1:1,000.

FACS of T cells from blood and skin

T cells were isolated, pre-enriched and stained as described above. BD CS&T beads were used to validate machine functionality. Fluorescence spillover compensation was performed with lymphocytes stained with CD4 (OKT4, Biolegend or BD Biosciences) in the respective colors. Flow cytometry data were analyzed using FACSDiva (version 8.0.2) BD FlowJo (versions 10.6.2 and 10.10.0). Sorting was performed with a BD FACSAriaII or BD FACSFusion cell sorter with an 85-µm nozzle and 45 psi of pressure. Postsort quality controls were performed as applicable. Cells were sorted directly into 500-µl of RLT+ lysis buffer (Qiagen AllPrep DNA/RNA Mini kit, 80204). All procedures were performed in DNA low-bind tubes (Eppendorf, 0030108051). From human skin samples, we sorted 3,500 to 10,000 T_{reg} cells ($CD45^+CD3^+TCR\beta^+CD4^+CD8^-CD127^-CD25^+$) and 5,500 to 10,000 T_{conv} cells ($CD45^+CD3^+TCR\beta^+CD4^+CD8^-CD127^+CD25^-$). From human peripheral blood samples, we sorted 10,000 $CD45RA^+$ T_{reg} cells ($CD45^+CD3^+TCR\beta^+CD4^+CD8^-CD127^-CD25^+CD45RA^+CD45RO^-$), 10,000 $CCR8^+$ T_{reg} cells ($CD45^+CD3^+TCR\beta^+CD4^+CD8^-CD127^-CD25^+CD45RA^-CD45RO^+CCR8^+$) and 10,000 $CD45RA^+$ T_{conv} cells ($CD45^+CD3^+TCR\beta^+CD4^+CD8^-CD127^+CD25^-CD45RA^+CD45RO^-$).

Whole-genome bisulfite sequencing

DNA was isolated using a DNA/RNA micro kit (Qiagen, 80284), and DNA quality and concentration were assessed by Qubit (dsDNA HS kit, Q32851) and TapeStation 4200 with Genomic DNA Screentape (Agilent, 5067-5365). Tagmentation-based whole-genome bisulfite sequencing was essentially performed as described previously[51]. Two differently barcoded libraries were generated each per sample. Corresponding libraries were pooled in equimolar amounts, and each pool was sequenced on a single lane using an Illumina Novaseq 6000 with paired-end sequencing and 150 cycles (PE150).

scATAC-seq

The scATAC-seq data set was taken from our previous study[10].

Bulk RNA-seq

The RNA-seq data set was taken from our previous study[10]. This data set had been generated as follows. Total RNA was isolated using a DNA/RNA micro kit (Qiagen, 80284), and RNA was eluted in 14 µl of RNase-free water. RNA quality was assessed using a TapeStation 4200 and High-Sensitivity RNA Screentape (Agilent, 5067-5579). Eight microliters of RNA was used for generating RNA-seq libraries using a SMART-Seq Stranded kit (Takara, 634444). Indexed libraries were pooled in an equimolar ratio and sequenced on an Illumina NextSeq 550 machine with a NextSeq 500/550 High Output kit v2.5 (75 cycles). DNA was eluted in 30 µl of buffer EB and used for whole-genome bisulfite sequencing as described above.

Generation of amplicon data for validation of methylation differences

Custom bisulfite primers were designed using the bisulfite primer seeker (Zymo Research; for primer sequences, see Supplementary Table 4). The forward primers were extended with barcode sequences for multiplexing (Supplementary Table 4). In addition, forward and reverse primers were extended with partial Illumina sequences as recommended by Genewiz, from Azenta Life Sciences, where sequencing was performed (5′–3′ forward: ACACTCTTTCCCTACACGACGCTCTTCCGATCT; reverse: GACTGGAGTTCAGACGTGTGCTCTTCCGATCT). Primers were synthesized by Sigma-Aldrich. DNA was extracted using a DNeasy Blood and Tissue kit (Qiagen, 69504). Afterward, bisulfite conversion was performed using an EpiTec Bisulfite kit (Qiagen, 59104). For amplicon generation, KAPA HiFi HotStart ReadyMix was used (Roche, 7959079001). Together with bisulfite-converted DNA, barcoded forward and reverse primers and double-distilled water, PCRs were run (initial denaturation at 95 °C for 3 min, 35 cycles start denaturation at 98 °C for 20 s, annealing at primer optimal temperature for 15 s, extension at 72 °C for 15 s, cycle end, final extension at 72 °C for 1 min and hold indefinitely at room temperature). To clean up the PCR products, 1% agarose gels were run, and a MiniElute Gel Extraction kit was used to extract the amplicons (Qiagen, 28604). Afterward, Qubit and TapeStation were run to measure concentration and average base pair size. Taking the barcodes and regions into account, the different amplicons were pooled and sequenced on an Illumina MiSeq machine, yielding 2 × 250 bp paired-end reads. The analysis of the corresponding data is described in 'Bioinformatics: general'.

CRISPR-based transcriptional activation of *MLPH* and *GNA11*

Blood $CD45RA^+$ T_{reg} cells were isolated from peripheral blood mononuclear cells by gradient centrifugation, followed by MACS and FACS isolation as described above. Cells were rested with 100 U ml^{-1} IL-2 for 24 h before being transduced with dCas9-VP64 and guide RNA using separate lentiviral vectors. Guide RNA sequences were 5′TTAGATGGGAGCTATGTGTG3′ for *MLPH_A*, 5′TGCTAGTGAGATTTGAGCAC3′ for *MLPH_B* and 5′AGCCCCTGACCCGAGACTGA3′ for *GNA11*. A random guide RNA sequence ('scrambled'; 5′GACCATCTTCTAACCTTACA3′) was used as a negative control. After 3–6 days of incubation, cells transduced with both dCas9-VP64 and guide RNA were sorted by FACS based on expression of co-transduced reporter genes. RNA isolation was performed using an innuPREP RNA Mini kit according to the manufacturer's specifications. cDNA synthesis was performed according to the manufacturer's protocol (Reverse Transcriptase II, Life Technologies). Quantitative PCR with reverse transcription was performed with TaqMan probes and master mix in a Viia7 real-time PCR system (all Thermo Fisher Scientific). Gene expression was normalized to housekeeping gene expression (*HPRT*).

To control for efficient and specific targeting of the guides, classic CRISPR–Cas9 constructs able to cleave DNA containing the same guide RNAs were generated. Guide RNA was generated by mixing transactivating CRISPR RNA (Integrated DNA Technologies, 1072534) and *MLPH* CRISPR RNAs (sequence: 5′TTAGATGGGAGCTATGTGTG3′), *GNA11* CRISPR RNAs (sequence: 5′AGCCCCTGACCCGAGACTGA3′) or scrambled CRISPR RNAs (Integrated DNA Technologies, 1072544) in equimolar concentrations, heating to 95 °C for 5 min and allowing to cool down to room temperature. Guide RNA mixes are combined with Cas9 Enzyme (Integrated DNA Technologies, 1081060) and incubated at room temperature for 30 min to form the RNP complex. Electroporation was performed using a Neon transfection instrument (settings: 1,600 V, 10-ms pulse width, three pulses; Thermo Fisher Scientific) in the presence of an electroporation enhancer (Thermo Fisher Scientific, 1075915) using a Neon transfection system 10 µl kit (Thermo Fisher Scientific, MPK1096). $CD4^+$ T cells were cultured with 100 U ml^{-1} IL-2 and Transact for 3 days before genomic DNA was isolated using a QIAmp DNA Mini kit (Qiagen, 51304). Target DNA was PCR amplified using the following primers: 5′CCACACACACACACGCTATTGGCTCTGC3′ and 5′GCGGACCGTGGCTGTGGCCTGTG3′ for *MLPH* and 5′CCACACACACACACGCTATTGGCTCTGC3′ and 5′GCGGACCGTGGCTGTGGCCTGTG3′ for *GNA11*. PCR amplicons were Sanger sequenced, and Tracking of Indels by Decomposition (http://shinyapps.datacurators.nl/tide/) confirmed specific targeting of both guides to the respective genomic position.

Origin, treatment and analyses of Kaede-expressing mice

Tg(CAG-Kaede)15Kgwa mice[33] (genetic background: C57BL/6J) were a gift from R. Linker (Clinic and Polyclinic for Neurology at the University of Regensburg). Animals were housed under specific pathogen-free conditions at the Regensburg University Clinic animal care facility, and the governmental committee for animal experimentation

(Regierungspräsidium Unterfranken) approved all experiments involving animals. We used seven adult male and female mice between 30 and 35 weeks of age. Air exchange rates were >8 AC h^{-1}, light/dark cycles were 12 h/12 h, and mice were maintained at ambient temperature (22 ± 2 °C) and a relative humidity of 55 ± 10%. Tg(CAG-Kaede)15Kgwa mice express the photoconvertible fluorescent Kaede protein under the control of a CAG promoter. The excitation maximum of 'Kaede-green' was 508 nm. During exposure to violet light, the Kaede-green protein was converted to 'Kaede-red', which is characterized by an excitation maximum of 572 nm (ref. 52). For photoconversion of skin, Tg(CAG-Kaede)15Kgwa mice were anesthetized, hair and hair follicles from the back were removed with an electric shaver and depilatory cream, and an area of 8 cm^2 was exposed to violet light for 5 min (100% intensity at a distance of 10 cm using a CoolLED lamp from the pE-100 series with 440 nm; AHF). Six days after initial exposure, animals were killed, and skin dLNs (inguinal and axillary) were collected. Randomization was not applicable as mice were not assigned to different experimental groups. For the same reason, data collection and analysis were not performed blind to the conditions of the experiments. T cells were isolated from LNs by mechanical dissociation on a 40-µm filter. Cells were pre-enriched for CD25 by staining biotinylated anti-mouse CD25 (clone PC61, Biolegend, 102003), followed by column-based magnetic separation with anti-biotin microbeads (Miltenyi Biotec, 130-105-637) following the manufacturer's protocol. The following mouse antibodies were used for surface staining: CD4-BUV395 (GK1.5, BD Biosciences, 563790), TCRβ-BV605 (H57-597, Biolegend, 109241), GITR-PE-Cy7 (DTA-1, Biolegend, 126318) and CCR8-BV421 (SA214G2, Biolegend, 150305) or Rat IgG2bk BV421 Isotype Ctrl (RTK4530, Biolegend, 400655) at a dilution of 1:100. Viability staining was performed using eBioscience Fixable Viability Dye eFluor 780 (Thermo Fisher Scientific, 65-0865-14) according to manufacturer's instructions at a dilution of 1:1,000. Data analysis was performed using FlowJo v10.10 and GraphPad Prism v10.4.1.

Bioinformatics: general

Software versions and corresponding references, if available, are indicated upon first mention of the respective software. All analyses that used the programming language R were performed using R v4.0.0.

Preprocessing of whole-genome bisulfite sequencing data

Alignment and methylation calling was performed based on a previously described workflow[53] that uses a customized version of methylCtools[54]. The workflow was modified as follows. Trimmomatic[55] (v0.30) PE was used to trim adaptor sequences with the options '-threads 12 -phred33 ILLUMINACLIP:xxx:2:30:10:8:true SLIDINGWINDOW:4:15 MINLEN:36'. Here, 'xxx' refers to a fasta file containing the adaptor sequences. Alignment to the hs37d5 reference genome (based on GRCh37) was performed using BWA-MEM[56] (v0.7.8) with the '-T' parameter set to 0. Duplicates were marked using sambamba (v0.6.5) with the parameters '-t 1 -l 0–hash-table-size = 2000000–overflow-list-size = 1000000–io-buffer-size = 64' and not removed from the data. We confirmed successful bisulfite conversion in all but one sequencing library by observing low methylation signal at CH sites (Extended Data Fig. 1b). Here, we restricted our analysis to the first 3,000,000 CH sites on chromosome 1. The sequencing library that did not meet this quality criterion was subsequently excluded. For the analysis of CpGs, we combined data on the two opposite cytosines of the same CpG by summing up their read counts. To compute position-wise coverage, we added the counts of methylated and unmethylated reads at each profiled position. One skin T$_{reg}$ cell sample displayed exceptionally low coverage (Extended Data Fig. 1c) as we had excluded the library with aberrant CH methylation signal. Because all donors were female, we excluded positions on chromosome Y. We then stored the counts of methylated and total reads at each position in a bsseq object (bsseq[57] package; v1.26.0). We computed smoothed methylation values using the BSmooth function from the bsseq package.

Preprocessing of RNA-seq data

The RNA-seq data set was taken from our previous study[10]. It had been preprocessed as follows. For all samples, low-quality bases were removed with Fastq_quality_filter from the FASTX (http://hannonlab.cshl.edu/fastx_toolkit/index.html) Toolkit v0.0.13, with 90% of the reads needing a quality phred score of >20. Homertools[31] v4.7 was used for poly(A) tail trimming, and reads with a length of <17 were removed. PicardTools v1.78 (https://broadinstitute.github.io/picard/) was used to compute the quality metrics with CollectRNASeqMetrics. With STAR[58] v2.3, the filtered reads were mapped against human genome 38 using default parameters. Count data and RPKM tables were generated by mapping filtered reads against union transcripts using a custom pipeline. Mapping was performed with bowtie2 (ref. 59) v2.2.4 against union human genes: every gene is represented by a union of all its transcripts (exons). The count values (RPKM and raw counts) were calculated by running CoverageBed from Bedtools v2.26.0 of the mapped reads together with the human annotation file (Ensembl 90) in gtf format and parsing the output with custom Perl scripts.

UMAP visualization of scATAC-seq data

We subsetted scATAC-seq data to the relevant cell types and renormalized the data using the term frequency–inverse document frequency (TF-IDF) approach (RunTFIDF function from Signac[60]; v1.2.1). We then identified the most relevant peaks using Signac's FindTopFeatures function and performed dimensionality reduction with Signac's RunSVD function. We subsequently corrected for donor-specific effects using the RunHarmony function (group.by.vars = 'donor', project.dim = FALSE) from the harmony[61] package (v0.1.0). Finally, we computed a uniform manifold approximation and projection (UMAP) representation using Seurat's[62] (v4.0.1) RunUMAP function with the argument 'dims = 2:50'. This excluded the first harmony-corrected component, which we had previously found to be strongly correlated with sequencing depth.

Principal component analysis

We divided the hs37d5 reference genome into 5,000-bp bins and computed sample-level mean raw methylation across all CpGs in a bin using the getMeth function (regions = bins, type = 'raw', what = 'perRegion') from bsseq. We then selected bins in which all samples displayed a mean CpG-level coverage of at least 2 and exhibited a nonmissing methylation value. Among these, we identified the 2,000 bins displaying the highest variance across samples and ran a principal component analysis using the prcomp function (scale. = TRUE).

Analysis of global methylation

To visualize methylation across the whole genome, we divided the hs37d5 reference genome into bins of 1,000,000 bases. For each bin and each sample, we then computed the mean raw methylation across all CpGs in that bin using bsseq's getMeth function (regions = bins, type = 'raw', what = 'perRegion'). We averaged these bin-level values across all samples of a cell type (rowMeans function with 'na.rm = TRUE') and computed the deviation of this value from the average value of blood CD45RA$^+$ T$_{conv}$ cells. We removed bins on the mitochondrial chromosome. To plot genome-wide methylation together with chromosome band information, we used the circos.initializeWithIdeogram (species = 'hg19', plotType = c('ideogram', 'labels'), chromosome.index = relevant_chromosomes) function from circlize[63] (v0.4.13). We then plotted the methylation values using circlize's circos.track and circos.yaxis functions. To calculate global methylation values for autosomes and chromosome X, we extracted raw sample-level methylation values for every CpG using bsseq's getMeth function (type = 'raw', what = 'perBase'). Of these, we selected CpGs displaying a coverage of at least 2 in all samples. We then computed sample-level mean methylation values across CpGs in the respective chromosome categories (all autosomes or chromosome X) and averaged the resulting values across all samples of a cell type.

Extraction of methylation-level cell-type signatures

To extract cell-type signatures at the methylation level, we first generated CpG-level annotations. To this end, we considered all CpGs that displayed a coverage of at least 2 in at least two samples of each cell type. For these CpGs, we extracted sample-level smoothed methylation values using the getMeth function (type = 'smooth', what = 'perBase') from bsseq. We averaged these values across all samples from a cell type (mean function with 'na.rm = TRUE') and ranked the cell types according to these averages. Afterward, we identified the largest and second-to-largest methylation gap between any two adjacent cell types in this ranking. Furthermore, we computed the maximum standard error of the mean (excluding missing values) across the methylation values for all cell types. We annotated a CpG to a signature category if the largest methylation gap was at least 0.15, the ratio between the largest and second-to-largest gap was at least 1.5, and the maximum standard error was not larger than 0.5 times the largest gap. We left all CpGs that did not meet these requirements unannotated. To generate names for signature categories, we divided cell types into two groups based on the location of the largest gap. We named categories according to what cell types were in the group displaying lower methylation (for example, 'Skin T_{reg}/Blood CCR8$^+$ T_{reg}'). Based on these CpG-level annotations, we identified signature regions. To this end, we identified groups of consecutive CpGs with the same annotation that were not more than 300 bp apart. We termed these groups of CpGs 'signature regions'. Afterward, we removed signature regions that contained fewer than three CpGs or displayed a mean coverage (across all CpGs in this region) below 2 in at least one sample. To remove signature regions that were identified due to smoothing artifacts, we performed an additional filtering step based on raw methylation. We fitted a logistic regression model (glm function with the family argument set to 'binomial') to sample-level mean raw methylation values (across CpGs; bsseq's getMeth function with regions = 'region_intervals', what = 'perRegion', type = 'raw'), using methylation as an independent variable and group membership (lower or higher methylation) as a dependent variable. We performed leave-one-out cross-validation by ignoring one sample at a time, fitting the logistic model using all remaining samples and using the fitted model to predict group membership (higher or lower methylation) of the left-out sample. If more than one sample was misclassified during this process, we discarded the respective signature region.

Intervals defined with respect to gene bodies and CpG islands

We used locations of gene bodies and exons in the hs37d5 reference genome that were computed based on the Gencode[64] annotation, version 19. We inferred transcription start sites by the start and end position of gene body intervals together with genomic strand information. For genes on the plus strand, we identified the start of the gene body as the transcription start site. For genes on the minus strand, we identified the end of the gene body as the transcription start site. We ordered exons and introns according to their distance to the transcription start site. We downloaded locations of CpG islands ('cpgIslandExt' data set) from https://hgdownload.cse.ucsc.edu/goldenPath/hg19/database/ on 7 March 2022. We defined shores as the 2,000 bp flanking a CpG island on both sides and shelves as the 2,000 bp flanking these shores.

Differential methylation analysis

To identify regions of differential methylation between two cell types, we adapted the strategy for signature extraction (see above) to a two-class comparison. We did not consider the ratio between the largest and second-to-largest methylation gap because the second-to-largest gap does not exist in a two-class comparison. Furthermore, we discarded regions for which at least one sample was misclassified during leave-one-out cross-validation with logistic regression.

Differential peak accessibility analysis in scATAC-seq data

We subsetted scATAC-seq data to the two compared populations and renormalized the data using Signac's RunTFIDF function. We then analyzed differential accessibility using the FindMarkers (test.use = 'LR', latent.vars = 'peak_region_fragments') function from Seurat. We considered a peak statistically significant if its Bonferroni-adjusted P value was below 0.05. Sample sizes were 5,687 blood CD45RA$^+$ T_{reg} cells, 6,531 blood CD45RA$^+$ T_{conv} cells and 4,091 skin T_{reg} cells. For heat map visualization (see Figs. 2a and 3a), we averaged normalized accessibility values across all cells of the respective cell type. We did so separately for each donor who had donated cells from the respective compartment (blood or skin).

Differential expression analysis of RNA-seq data

We considered all genes that had a unique gene symbol and performed differential gene expression analysis based on raw expression counts. For the actual analysis, we used the functions DESeqDataSetFromMatrix ('design = ~ Donor + Cell_type' for the comparison between blood CD45RA$^+$ T_{reg} cells and blood CD45RA$^+$ T_{conv} cells and 'design = ~ Cell_type' for all other comparisons because of their unpaired sample structure) from the DESeq2 (ref. 65) package (v1.30.1) and relevel from the stats package, followed by the functions DESeq and results ($\alpha = 0.05$) from the DESeq2 package. The inclusion of donor ID as a model covariate was due to the partly paired sample structure in the comparison between blood CD45RA$^+$ T_{reg} cells and blood CD45RA$^+$ T_{conv} cells. For differential TE expression analysis, we deviated from this workflow as described in the respective Methods section. We considered a feature statistically significant if its Benjamini–Hochberg-adjusted P value ('padj' column in the results table returned by DESeq2) was below 0.05 and its absolute $\log_2$ (fold change) was above 0.5. Sample sizes were five samples (from five donors) for blood CD45RA$^+$ T_{reg} cells, three samples (from three donors) for blood CD45RA$^+$ T_{conv} cells, four samples (from four donors) for skin T_{reg} cells and five samples (from five donors) for blood CCR8$^+$ T_{reg} cells.

Computation of TPM values in RNA-seq data

We converted previously computed RPKM values to TPM values by multiplying each RPKM value by 1,000,000 and then dividing by the sum of RPKM values across all genes in the respective sample.

Definition and analysis of DMR–peak–gene links

We defined a DMR–peak–gene link as a combination of a DMR, an overlapping differentially accessible peak and a differentially expressed gene that both the DMR and the peak were associated with. We considered a genomic region (DMR or peak) associated with a gene if it overlapped with the gene body or the 2,000-bp interval upstream of the transcription start site. To identify these associations, we used the gene annotation described in 'Intervals defined with respect to gene bodies and CpG islands'. To compute differences in methylation, we extracted sample-level mean raw methylation values across all CpGs in a DMR using bsseq's getMeth function (regions = DMRs, type = 'raw', what = 'perRegion'). We aggregated these to the cell-type level by averaging across all samples of a cell type (rowMeans function with 'na.rm = TRUE') and computed the difference between the two cell types. For heat map visualization of accessibility values in DMR–peak–gene links, we averaged normalized accessibility values across all cells of the respective cell type. We did so separately for each donor who had donated cells from the respective compartment (blood or skin).

Generation of track plots

To visualize methylation, chromatin accessibility and other position-wise data in selected genomic regions, we used track plots.

We generated methylation tracks by extracting smoothed methylation values for each CpG and sample using bsseq's getMeth function (regions = regions_of_interest, type = 'smooth', what = 'perBase'). The track plot consists of lines connecting CpG-wise values for each sample. To visualize chromatin accessibility in the same regions, we used BAM files of scATAC-seq data. If necessary, we merged BAM files corresponding to subsets of the same cell type using sambamba merge. We then generated BigWig files containing scATAC-seq signal aggregated into 50-bp genomic bins. For this, we used RPKM normalization using bamCoverage (-of bigwig --normalizeUsing RPKM) from the deeptools[66] suite (v3.5.1). We used the import function from the rtracklayer[67] package (v1.50.0) to load BigWig files into memory. If the plot contained ChIP–seq data, we read the corresponding BigWig files into memory using the same function. To visualize genes in the corresponding regions, we used locations of gene bodies and exons in the hs37d5 reference genome that were computed based on the Gencode annotation, version 19. We inferred transcription start sites as described in 'Intervals defined with respect to gene bodies and CpG islands'. We aligned all data panels using the plot_grid function (ncol = 1, axis = 'lr', align = 'v') from cowplot (v1.1.1). To visualize raw methylation values alongside smoothed methylation values, we extracted raw methylation for each CpG site covered in a track plot using bsseq's getMeth function (regions = region_of_interest, what = 'perBase', type = 'raw'). Each row in the resulting heat maps corresponds to a sample from one donor, and each column corresponds to one CpG site covered in the track plot.

Analysis of amplicon data for the validation of methylation differences

We demultiplexed sequencing reads by looking for exact sequence matches between the starts of R1 reads and the cell-type barcodes used. We removed these barcodes from the reads and subsequently trimmed remaining sequencing adaptors using cutadapt[68] (v4.8) with the options '-a R1_3prime_adaptor -G R2_5prime_adaptor -A R2_3prime_adaptor'. To enable sequencing read alignment, we downloaded the GRCh37 reference genome from http://ftp.ensembl.org/pub/release-75/fasta/homo_sapiens/dna/ on 6 June 2024 and prepared it for usage with the bismark[69] aligner (v0.20.0) using the bismark_genome_preparation command built into the alignment software. We then performed alignment using the bismark command with the options '--unmapped --ambiguous --genome genome_directory' together with bowtie (v2.3.5.1) and samtools (v1.11.0). To increase alignment yield, we realigned previously unmapped R1 and R2 reads independently using the same alignment command. We merged BAM files from the different alignment steps using the samtools merge command and performed methylation calling on this merged BAM file using the bismark_methylation_extractor command with the options '--comprehensive --cytosine_report --genome_folder genome_directory'. To analyze methylation in the targeted genomic regions, we converted the resulting CpG-level methylation file into a structure resembling a Bed file and then extracted all CpGs overlapping with targeted regions using the bedtools (v2.24.0) intersect command with the options '-a CpG_methylation_file -b Amplicon_interval_file -u'. We combined data on the two opposite cytosines of the same CpG by summing up their read counts. Coverage was computed as for whole-genome bisulfite sequencing data (see 'Preprocessing of whole-genome bisulfite sequencing data'). To assess the statistical significance of CpG-wise methylation differences, we used two-tailed Wilcoxon signed-rank tests. For visualization of methylation levels together with their statistical significance, we used the plot_grid (ncol = 1, axis = 'lr', align = 'v') function from cowplot.

Enrichment analysis of Hallmark gene sets

We downloaded the collection of Hallmark gene sets using the msigdbr function (species = '*Homo sapiens*', category = 'H') from the msigdbr package (v7.4.1) on 16 May 2024. We then identified DMR–peak–gene links displaying hypomethylation, hyperaccessibility and hyperexpression in skin T_{reg} cells compared to blood CD45RA$^+$ T_{reg} cells. From these links, we extracted all genes and investigated enrichment of Hallmark terms among them using one-tailed Fisher's exact tests. Our background collection of genes consisted of all genes present in the Gencode annotation, version 19.

Transcription factor analyses

To analyze enrichments of transcription factor motifs in selected genomic regions, we saved the respective region sets in Bed format and used the findMotifsGenome.pl functionality from homer[31] (v4.11) with the options 'hg19 -size given'. When we compared two region sets directly instead of characterizing single region sets independently, we specified a custom set of background regions via the -bg option. This was the case in the analysis of blood CCR8$^+$ T_{reg} cell positioning. Within a data type (methylation or chromatin accessibility), we used the 'closer to skin T_{reg}' regions as background for the 'closer to blood CD45RA$^+$ T_{reg}' regions and vice versa. To determine whether a motif was enriched or depleted in a region set, we divided the percentage of query regions containing the motif (as computed by homer) by the percentage of background regions containing the motif (as computed by homer). We considered a motif enriched if this quotient was above 1 and depleted otherwise.

To visualize methylation and chromatin accessibility around genomic sites for the relevant motifs, we updated the Seurat object containing scATAC-seq data. To this end, we applied the function UpdateSeuratObject from Seurat, used Signac's as.ChromatinAssay function to update the assay object with scATAC-seq data, set the genome of the chromatin assay to 'hg19' (Signac's genome function), applied Signac's CreateFragmentObject (path = fragments_file, cells = colnames(seurat_object)) function and added the resulting fragments object to the Seurat object (Signac's Fragments function). We then subsetted the Seurat object to the relevant cell types and renormalized data by the TF-IDF approach (Signac's RunTFIDF function). We used the position frequency matrices (PFMs) that were returned along with homer's results for relevant motifs. For our analysis, we converted them to a PFMatrixList object using the PFMatrix function (strand = '*', profileMatrix = 1,000 * PFM) and PFMatrixList function from TFBSTools[70] (v1.28.0). We added motif annotations to the Seurat object using the AddMotifs function (genome = BSgenome.Hsapiens.UCSC.hg19, pfm = PFMs) from Signac. For the visualization of methylation around motif sites, we extracted motif positions from the positions slot of the Motifs object (Signac's Motifs function). We extended these positions by 200 bases on each side and computed sample-level average raw methylation values across all CpGs therein (bsseq's getMeth function with arguments regions = 'extended_regions', type = 'raw', what = 'perRegion'). We excluded regions that returned missing values in every sample. In the final visualization, we ordered regions by their mean methylation across all visualized samples. For the visualization of chromatin accessibility around motif sites, we used the Footprint function from Signac (motif.name = names_of_relevant_motifs, genome = BSgenome.Hsapiens.UCSC.hg19) together with Signac's PlotFootprint function.

For the analysis of transcriptomic footprints, we obtained a network of transcription factors and their target genes using the get_dorothea function from decoupleR[71] (v2.3.2). We then analyzed the enrichment of transcription factor target genes among differentially expressed genes based on each gene's $\log_2$ (fold change) values using the fast gene set enrichment analysis (fgsea) method implemented in decoupleR's run_fgsea (mat = log2_fold_changes, network = transcriptionfactor_target_network) function.

To identify interesting motif sites for c-Myc and USF1, we extracted motif sites as described above. Our previous analysis had demonstrated enrichment of two motifs for c-Myc. For this c-Myc analysis, we only considered genomic sites of the 'c-Myc(bHLH)-Unpublished' motif that overlapped with genomic sites of the 'c-Myc(bHLH)-GSE11431' motif. We identified c-Myc/USF1 motif sites that overlapped with a 'Skin T_{reg} cell hypomethylation' DMR, a nondifferential peak and a region of pronounced c-Myc/USF1 ChIP–seq signal. We downloaded ChIP–seq tracks from ENCODE[32] via the Gene Expression Omnibus (GEO; accession numbers: GSM822291, GSM822310, GSM822290, GSM803527, GSM803441 and GSM803347) on 9 March 2023. If several replicates were available, we downloaded data for replicate 1.

Analysis of blood CCR8$^+$ T_{reg} cell positionings

We focused on all features that were different between skin T_{reg} cells and blood CD45RA$^+$ T_{reg} cells. For methylation levels, we extracted sample-level average raw methylation values across all CpGs in a region using bsseq's getMeth function (regions = DMRs, type = 'raw', what = 'perRegion'). We averaged these across all samples of a cell type (rowMeans function with 'na.rm = TRUE'). For chromatin accessibility levels, we subsetted the Seurat object with scATAC-seq data to the relevant cell types and renormalized the data by TF-IDF (RunTFIDF function from Signac). We extracted cell-level normalized accessibility data using SeuratObject's (v4.0.1) GetAssayData function (slot = 'data') and aggregated these into cell-type-level means. For the gene expression level, we extracted sample-level TPM values, transformed them by log (100 × TPM + 1) and averaged the resulting values across all samples of a cell type. We then excluded all features for which the extracted (and possibly transformed) values contradicted the differential tendencies found during differential analysis (zero DMRs, zero differential peaks and five differential genes). We scaled cell-type-level values linearly to an interval between 0 and 1. For each feature, we then identified whether its value in blood CCR8$^+$ T_{reg} cells was closer to that in skin T_{reg} cells or closer to that in blood CD45RA$^+$ T_{reg} cells. For heat map visualization of methylation and gene expression values (see Fig. 5a), we repeated the steps described above without computing the mean across samples so that each sample is displayed independently. For heat map visualization of chromatin accessibility values (see Fig. 5a), we averaged normalized accessibility values across all cells of the respective cell type. We did so separately for each donor who had donated cells from the respective compartment (blood or skin). We ordered features by the difference between blood CCR8$^+$ T_{reg} cells and skin T_{reg} cells (considering only the methylation level in the case of DMR–peak–gene links). For the analysis of blood CCR8$^+$ T_{reg} cell positionings stratified by blood CCR8$^+$ T_{reg} cell donor, we extracted methylation and gene expression values for each individual blood CCR8$^+$ T_{reg} cell donor. At the methylation level, we only considered DMRs that had nonmissing methylation values in all blood CCR8$^+$ T_{reg} cell donors. To compute donor-level values at the chromatin accessibility level, we considered all cells annotated to the relevant cell types that originated from the respective tissue and then averaged chromatin accessibility values across all relevant cells independently for each donor. For each blood CCR8$^+$ T_{reg} cell donor, we subsequently compared the donor-level methylation, chromatin accessibility and gene expression values to the corresponding cell-type-level values of skin T_{reg} cells and blood CD45RA$^+$ T_{reg} cells, which had been computed as described above.

Analyses based on TCR clonotypes

We used combined scRNA-seq/scTCR-seq data of human blood and skin T cells from our previous study[10]. This data set contains data from two donors (TCR Donors 6 and 7). To identify blood CCR8$^+$ T_{reg} cells and blood CD45RA$^+$ T_{reg} cells, we processed samples 28 (blood T_{reg} cells, TCR Donor 6), 29 (blood CD45RO$^+$ T_{reg} cells, TCR Donor 7), 24 (blood T_{reg} cells, TCR Donor 7) and 25 (blood CD45RO$^+$ T_{reg} cells, TCR Donor 7). For each sample, we identified the 3,000 most variable genes using Seurat's FindVariableFeatures function with the option 'nfeatures = 3000'. We then scaled expression data using Seurat's ScaleData function with the options features = 'rownames(seurat_object)' and vars.to.regress = 'nFeature_RNA'. We ran principal component analysis using Seurat's RunPCA function and generated a UMAP representation using the RunUMAP function (dims = 1:i) from Seurat. The parameter 'i' (that is, the number of principal components used) was 10 (samples 24 and 28), 20 (sample 29) and 30 (sample 25). For clustering by the Leiden algorithm, we used Seurat's FindNeighbors (dims = 1:i) and FindClusters (resolution = y, algorithm = 4) functions. The parameter 'i' was the same as above. The parameter 'y' (that is, the clustering resolution) was 0.7 (samples 24 and 28), 0.8 (sample 25) or 0.9 (sample 29). To annotate cells, we used several single marker genes next to two gene signatures defining blood CCR8$^+$ T_{reg} cells (Extended Data Fig. 8c–f). Blood CCR8$^+$ T_{reg} cell signature 1 contains genes that are overexpressed in blood CCR8$^+$ T_{reg} cells compared to blood CD45RA$^+$ T_{reg} cells according to our analysis of bulk RNA-seq data (see 'Differential expression analysis of RNA-seq data'). Blood CCR8$^+$ T_{reg} cell signature 2 contains genes that are overexpressed in blood CCR8$^+$ T_{reg} cells compared to blood CD45RO$^+$ (memory) T_{reg} cells. To generate this signature, we used another scRNA-seq/scTCR-seq sample (sample 30) from TCR Donor 6, which contains sorted blood CCR8$^+$ T_{reg} cells, and compared it to cells in sample 29 using Seurat's FindMarkers function. We interpreted genes with Bonferroni-adjusted P values below 0.05 as differentially expressed. To generate cell-level scores for the two blood CCR8$^+$ T_{reg} cell signatures, we used the AddModuleScore function from Seurat. For further analysis of blood CD45RA$^+$ T_{reg} cells, we examined blood CD45RA$^+$ T_{reg} cells identified in samples 24 and 28 (Extended Data Fig. 8c,e; note that samples 25 and 29 contain cells sorted for CD45RO expression and thus do not contain blood CD45RA$^+$ T_{reg} cells). For further analysis of blood CCR8$^+$ T_{reg} cells, we investigated blood CCR8$^+$ T_{reg} cells identified in samples 24, 25, 28 and 29 (Extended Data Fig. 8c–f), which we combined with all cells from the CCR8-sorted sample 30. Skin T_{reg} cells from both donors had previously been identified in this data set (TCR Donor 6: intersection between original cluster 10 and sample R3; TCR Donor 7: intersection between original cluster 8 and sample R7)[10]. We considered two cells 'TCR matched' if the nucleotide sequence string of their clonotypes was identical and if this sequence string contained at least one TCRα chain sequence and TCRβ chain sequence. To visualize clonotype sharing between cell types, we examined all clonotypes that appeared among skin T_{reg} cells and contained at least one TCRα chain sequence and TCRβ chain sequence. For each of these clonotypes, we identified TCR-matched cells among blood CCR8$^+$ T_{reg} cells and blood CD45RA$^+$ T_{reg} cells as described above. We then computed the percentage of each clonotype among all cells of the respective population that had nonmissing clonotype information. To compute module scores of our skin T_{reg} signatures, we used the 'Skin T_{reg} cell hyperexpression' and 'Blood CD45RA$^+$ T_{reg} hyperexpression' genes that are shown in Fig. 5a. We restricted single-cell gene expression data to (1) skin T_{reg} cells that were TCR matched with blood CCR8$^+$ T_{reg} cells, (2) blood CCR8$^+$ T_{reg} cells that were TCR matched with skin T_{reg} cells and (3) blood CD45RA$^+$ T_{reg} cells from clonotypes that were shared between skin T_{reg} cells and blood CCR8$^+$ T_{reg} cells. We then applied Seurat's AddModuleScore function.

TE analyses

To analyze the methylation and chromatin accessibility of TEs, we downloaded RepeatMasker annotations from University of California, Santa Cruz (UCSC, https://hgdownload.soe.ucsc.edu/goldenPath/hg19/database/rmsk.txt.gz), on 14 September 2023. To restrict our analysis to repeat elements that are confidently TE insertion sites, we selected elements that were classified as 'DNA', 'LINE', 'LTR', 'SINE', 'RC' or 'Retroposon' (column 12 of the resulting table). We extracted TE classes from column 12 and TE subfamily names from column 11 of the RepeatMasker table.

To investigate enrichments of TEs in sets of genomic regions, we identified the proportion of regions in the region set overlapping with TE insertion sites. We shuffled regions in the region set across the human genome 10,000 times by saving these regions in Bed format, generating a chromosome length file (lengths were retrieved using seqlengths from GenomeInfoDb (v1.26.7) together with BSgenome.Hsapiens.1000genomes.hs37d5 (v0.99.1) for DMRs and BSgenome.Hsapiens.UCSC.hg19 (v1.4.2) for peaks) and using bedtools shuffle (-noOverlapping) with 10,000 different random seeds and the previously generated chromosome length file. For each of these shufflings, we recomputed the proportion of regions from the (shuffled) region set overlapping with TE insertion sites. We computed an enrichment score as the proportion of regions from the original region set overlapping with TE insertion sites divided by the mean of this proportion across all random shufflings. We computed a one-tailed enrichment *P* value as the proportion of shufflings for which the overlap between regions from the shuffled region set and TE insertion sites was equal to or larger than the overlap obtained with the original, unshuffled, region set.

To investigate how far blood CCR8$^+$ T$_{reg}$ cells reflect TE-related epigenetic traits of skin T$_{reg}$ cells, we selected DMRs of the 'Skin T$_{reg}$ cell hypomethylation' class and peaks from the 'Skin T$_{reg}$ cell hyperaccessibility' class. We stratified these by whether they placed blood CCR8$^+$ T$_{reg}$ cells closer to skin T$_{reg}$ cells or closer to blood CD45RA$^+$ T$_{reg}$ cells. Afterward, we analyzed whether TEs were enriched in one of these strata with respect to the other. To this end, we identified overlaps between TE insertion sites and regions inside the two strata. We then assessed differences in overlap proportions between the two strata using Fisher's exact test.

We visualized methylation in TE insertion sites by extracting insertion site-level raw methylation values (bsseq's getMeth function with arguments regions = 'insertion_sites', type = 'raw', what = 'perRegion') and excluding insertion sites for which at least one sample displayed a missing value. We visualized accessibility in peaks overlapping with TE insertion sites by subsetting the scATAC-seq Seurat object to cells from relevant cell types originating from donors that had donated the respective tissue (blood or skin), renormalizing data by TF-IDF (Signac's RunTFIDF function), extracting normalized accessibility data with SeuratObject's GetAssayData function (slot = 'data') and averaging these across all cells, independently for each donor.

To analyze expression of TEs, we downloaded consensus sequences of TEs after browsing the Giri Repbase[72] (https://www.girinst.org/repbase/) with the criteria taxon '*Homo sapiens* (Human)', repeat class 'Transposable Element', include elements 'Autonomous' and 'Nonautonomous' and 'Simple' (that is, all) and download '*Homo sapiens* and ancestral (shared) repeats' on 3 November 2023. We also extracted sequences of full gene bodies in the human genome. To this end, we used the gene body annotations described in 'Generation of track plots' and used BSgenome's (v1.58.0) getSeq function (x = BSgenome.Hsapiens.1000genomes.hs37d5 and as.character = TRUE). Additionally, we downloaded sequences of human lncRNAs from Gencode version 19 (https://ftp.ebi.ac.uk/pub/databases/gencode/Gencode_human/release_19/gencode.v19.lncRNA_transcripts.fa.gz) on 19 December 2023. We applied TEspeX[73] (v2.0.1) to Fastq files with the options '--TE te_consensus_sequences --cdna gene_body_sequences --ncrna lncRNA_sequences --paired F --length 76 --strand 'no'' together with zlib (v1.2.12) and Python (v3.8.3). To compute TPM values, we divided raw expression counts by the respective consensus sequence length, divided these quotients by the sum of all quotients within the respective sample and multiplied the resulting value by 1,000,000. For heat map visualization, we clustered TEs by hierarchical clustering using the Euclidean distance and complete linkage. We identified differentially expressed TEs using DEseq2 as described in 'Differential expression analysis of RNA-seq data' with the following deviation: we did not run the wrapper function DEseq but executed the steps contained therein independently. The reason for this was that the DESeq function automatically estimates size factors based on the sums of read counts in the expression matrix. However, we reasoned that TE-derived reads account only for a minority of sequencing reads so that the complete read numbers (including non-TE reads) yield a more accurate estimate of the library size. We used DESeq2's sizeFactors function to manually set size factors to total read counts as returned by TEspeX, multiplied by 1×10^{-7}. Afterward, we used the functions estimateDispersions and nbinomWaldTest from DESeq2.

We computed methylation of HERVIP10F-int and LRT45B insertion sites overlapping with 'Skin T$_{reg}$ cell hypomethylation' DMRs by using bsseq's getMeth function (regions = overlapping_insertion_sites, type = 'raw', what = 'perRegion').

Statistics

Unless indicated in the respective figure caption or Methods, the statistical tests performed were two-tailed. We interpreted *P* values below 0.05 as statistically significant. If possible, test statistics, degrees of freedom, confidence intervals and so on are included in our Supplementary Tables or Source Data. In case of parametric tests, data distribution was assumed to be normal, but this was not formally tested.

Reporting summary

Further information on research design is available in the Nature Portfolio Reporting Summary linked to this article.

Data availability

Human whole-genome bisulfite sequencing data have been deposited in the European Genome Phenome Archive (EGA; accession number EGAD50000001022) and will be available under controlled access. The following are the file name conventions: labels 1–3: skin T$_{reg}$ cell samples; labels 4–6: skin T$_{conv}$ cell samples; labels 13–15: blood CCR8$^+$ T$_{reg}$ cell samples; labels 16–18: blood CD45RA$^+$ T$_{reg}$ cell samples; labels 19–21: blood CD45RA$^+$ T$_{conv}$ cell samples. Access will require application to a data access committee and will require a data sharing agreement. CpG-level methylation data have been deposited in GEO (accession number: GSE286948) and are available without restrictions.

We used data sets that were already used in our previous study[10]. Corresponding raw sequencing data have been deposited in the EGA (accession numbers: EGAD00001006779 for scATAC-seq; EGAD00001007665 and EGAD00001007661 for scRNA-seq/scTCR-seq; EGAD00001007663 and EGAD00001007665 for bulk RNA-seq; access requires application to a data access committee and a data sharing agreement). The versions of the corresponding processed data that were used in this study are available on Zenodo (https://doi.org/10.5281/zenodo.14999322 (ref. 74) for scATAC-seq; https://doi.org/10.5281/zenodo.14999788 (ref. 75) for scRNA-seq/scTCR-seq; https://doi.org/10.5281/zenodo.14999989 (ref. 76) for bulk RNA-seq).

In addition, we used several data sets from other sources. The hs37d5 reference genome is publicly available at https://ftp.ncbi.nlm.nih.gov/1000genomes/ftp/technical/reference/phase2_reference_assembly_sequence. The GRCh37 reference genome is available at http://ftp.ensembl.org/pub/release-75/fasta/homo_sapiens/dna. The human genome 38 is available at https://hgdownload.soe.ucsc.edu/goldenPath/hg38/chromosomes. Gencode V19 annotations are available at https://ftp.ebi.ac.uk/pub/databases/gencode/Gencode_human/release_19. We downloaded locations of CpG islands (the 'cpgIslandExt' data set) from https://hgdownload.cse.ucsc.edu/goldenPath/hg19/database. Hallmark gene sets are available via the msigdbr function (species = '*Homo sapiens*', category = 'H') from the msigdbr package. ChIP–seq data for c-Myc and USF1 are publicly available at GEO (accession numbers: GSM822291, GSM822310, GSM822290, GSM803527, GSM803441 and GSM803347). RepeatMasker annotations are available at https://hgdownload.soe.ucsc.edu/goldenPath/hg19/database/rmsk.txt.gz. We downloaded consensus sequences of TEs from the Giri Repbase[72] (https://www.girinst.org/repbase/). Sequences of human lncRNAs are available at https://ftp.ebi.ac.uk/pub/databases/gencode/Gencode_human/release_19/gencode.v19.lncRNA_transcripts.fa.gz.

Source data for this study are available at Zenodo at https://doi.org/10.5281/zenodo.15607737 (ref. 77).

Code availability

We did not develop any new software but used functionality that is publicly available via software packages as described in the Methods. Our wrappercode used for running this publicly available software is published on GitHub, can be accessed without restrictions at https://github.com/DKFZ-ABI/hum_tistreg_methylation and is reusable under a CC BY-NC-SA 4.0 license.

References

50. Wu, M. J. et al. Mutant IDH1 inhibition induces dsDNA sensing to activate tumor immunity. *Science* **385**, eadl6173 (2024).
51. Weichenhan, D. et al. Tagmentation-based library preparation for low DNA input whole genome bisulfite sequencing. *Methods Mol. Biol.* **1708**, 105–122 (2018).
52. Ando, R., Hama, H., Yamamoto-Hino, M., Mizuno, H. & Miyawaki, A. An optical marker based on the UV-induced green-to-red photoconversion of a fluorescent protein. *Proc. Natl Acad. Sci. USA* **99**, 12651–12656 (2002).
53. Wang, Q. et al. Tagmentation-based whole-genome bisulfite sequencing. *Nat. Protoc.* **8**, 2022–2032 (2013).
54. Hovestadt, V. et al. Decoding the regulatory landscape of medulloblastoma using DNA methylation sequencing. *Nature* **510**, 537–541 (2014).
55. Bolger, A. M., Lohse, M. & Usadel, B. Trimmomatic: a flexible trimmer for Illumina sequence data. *Bioinformatics* **30**, 2114–2120 (2014).
56. Li, H. Aligning sequence reads, clone sequences and assembly contigs with BWA-MEM. Preprint at https://arxiv.org/abs/1303.3997 (2013).
57. Hansen, K. D., Langmead, B. & Irizarry, R. A. BSmooth: from whole genome bisulfite sequencing reads to differentially methylated regions. *Genome Biol.* **13**, R83 (2012).
58. Dobin, A. et al. STAR: ultrafast universal RNA-seq aligner. *Bioinformatics* **29**, 15–21 (2013).
59. Langmead, B., Trapnell, C., Pop, M. & Salzberg, S. L. Ultrafast and memory-efficient alignment of short DNA sequences to the human genome. *Genome Biol.* **10**, R25 (2009).
60. Stuart, T., Srivastava, A., Madad, S., Lareau, C. A. & Satija, R. Single-cell chromatin state analysis with Signac. *Nat. Methods* **18**, 1333–1341 (2021).
61. Korsunsky, I. et al. Fast, sensitive and accurate integration of single-cell data with Harmony. *Nat. Methods* **16**, 1289–1296 (2019).
62. Hao, Y. et al. Integrated analysis of multimodal single-cell data. *Cell* **184**, 3573–3587 (2021).
63. Gu, Z., Gu, L., Eils, R., Schlesner, M. & Brors, B. Circlize implements and enhances circular visualization in R. *Bioinformatics* **30**, 2811–2812 (2014).
64. Frankish, A. et al. GENCODE reference annotation for the human and mouse genomes. *Nucleic Acids Res.* **47**, D766–D773 (2019).
65. Love, M. I., Huber, W. & Anders, S. Moderated estimation of fold change and dispersion for RNA-seq data with DESeq2. *Genome Biol.* **15**, 550 (2014).
66. Ramirez, F. et al. deepTools2: a next generation web server for deep-sequencing data analysis. *Nucleic Acids Res.* **44**, W160–W165 (2016).
67. Lawrence, M., Gentleman, R. & Carey, V. rtracklayer: an R package for interfacing with genome browsers. *Bioinformatics* **25**, 1841–1842 (2009).
68. Martin, M. Cutadapt removes adapter sequences from high-throughput sequencing reads. *EMBnet J.* **17**, 10–12 (2011).
69. Krueger, F. & Andrews, S. R. Bismark: a flexible aligner and methylation caller for bisulfite-seq applications. *Bioinformatics* **27**, 1571–1572 (2011).
70. Tan, G. & Lenhard, B. TFBSTools: an R/bioconductor package for transcription factor binding site analysis. *Bioinformatics* **32**, 1555–1556 (2016).
71. Badia, I. M. P. et al. decoupleR: ensemble of computational methods to infer biological activities from omics data. *Bioinform. Adv.* **2**, vbac016 (2022).
72. Bao, W., Kojima, K. K. & Kohany, O. Repbase update, a database of repetitive elements in eukaryotic genomes. *Mob. DNA* **6**, 11 (2015).
73. Ansaloni, F., Gualandi, N., Esposito, M., Gustincich, S. & Sanges, R. TEspeX: consensus-specific quantification of transposable element expression preventing biases from exonized fragments. *Bioinformatics* **38**, 4430–4433 (2022).
74. Beumer, N. Processed single-cell ATAC-seq data of $CD4^+$ T cell subsets from skin and blood of healthy human donors. *Zenodo* https://doi.org/10.5281/zenodo.14999322 (2025).
75. Beumer, N. Processed single-cell RNA/TCR-seq data of regulatory T cells from blood and skin of healthy human donors. *Zenodo* https://doi.org/10.5281/zenodo.14999788 (2025).
76. Beumer, N. Processed RNA-seq data of $CD4^+$ T cell subsets from blood and skin of healthy human donors. *Zenodo* https://doi.org/10.5281/zenodo.14999989 (2025).
77. Beumer, N. Source data for the publication ‘DNA hypomethylation traits define human regulatory T cells in cutaneous tissue and identify their blood recirculating counterparts’. *Zenodo* https://doi.org/10.5281/zenodo.15607737 (2025).

Acknowledgements

We thank the Leibniz Institute for Immunotherapy (LIT) and Research Center for Immunotherapy Mainz (*Forschungszentrum für Immuntherapie*, FZI) Next-Generation Sequencing core facility, the LIT and FZI flow cytometry core facility and the University Regensburg animal facility for technical support. We thank V. Hofmann, H. Stanewsky, M. Wuttke, J. Raitel, U. Ackermann, R. Eder and I. Fink (all LIT) for technical support. We thank B. Hutter (DKFZ) for help with Gencode annotations. We thank R. Linker (Clinic and Polyclinic for Neurology at the University of Regensburg) for Tg(CAG-Kaede)15Kgwa mice. This work was supported by grants from the European Research Council (ERC-CoG, 648145 REGiREG; to M.F.) and the Deutsche Forschungsgemeinschaft (German Research Foundation) Projektnummer 324392634–TRR221 (to M.F.), Projektnummer 318346496–SFB1292/2 TP19N (to M.D. and F.M.), Projektnummer 490846870–TRR355/1 TPA01 (to J.H. and M.D.) and TPZ02 (to M.D.). The funders had no role in study design, data collection and analysis, decision to publish or preparation of the manuscript.

Author contributions

Study design: M.F., M.D., N.B. and J.H. Analysis of bisulfite sequencing data: N.B. Analysis of scATAC-seq data: N.B. Analysis of RNA-seq data: N.B. Analysis of TEs: N.B. Analyses related to TCR sequences: N.B. and C.D.I. Development and execution of amplicon-based validation experiments: T.K. Contribution to experimental work and/or analyses: L.S., K.G., P.S., H.M., D.W., M.B., B.R., F.M., L.S., U.R., M.S., K.L.B., M.M.V., S.S.H., D.M.M., A.H.-W., H.N., A.E., L.P., C.G., M.R., N.S, K.S., J.K.P., C.S., C.P. and T.H. Original manuscript draft: N.B., M.F., M.D., T.K., C.D.I., L.S., P.S., C.S., M.R., J.H., U.R., K.S. and J.K.P. Supervision of investigation: M.F., M.D., C.D.I., B.B. and C.P. Funding acquisition: M.F., M.D., F.M. and J.H.

Competing interests

M.D. received personal fees from Odyssey Therapeutics outside the submitted work. The other authors declare no competing interests.

Additional information

Extended data is available for this paper at https://doi.org/10.1038/s41590-025-02210-x.

Supplementary information The online version contains supplementary material available at https://doi.org/10.1038/s41590-025-02210-x.

Correspondence and requests for materials should be addressed to Michael Delacher or Markus Feuerer.

Peer review information *Nature Immunology* thanks Adrian Liston and the other, anonymous, reviewer(s) for their contribution to the peer review of this work. Primary Handling Editor: Ioana Staicu, in collaboration with the *Nature Immunology* team.

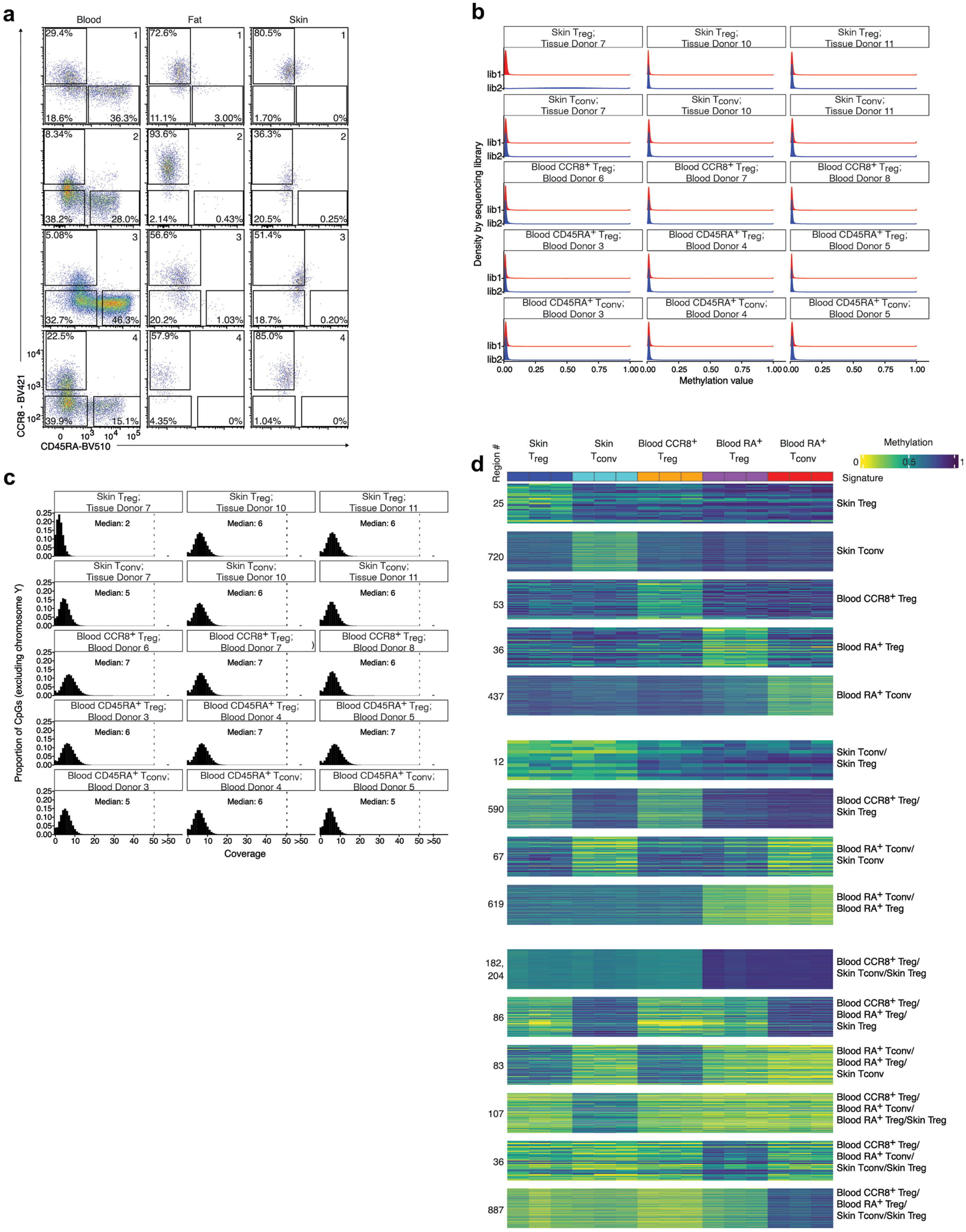

Extended Data Fig. 1 | See next page for caption.

Extended Data Fig. 1 | Quality control and methylation-level cell type signatures. a, Frequency of CD45RA$^-$CCR8$^+$ T$_{reg}$ cells among CD4$^+$CD127$^-$CD25$^+$ T$_{reg}$ cells in human blood, fat and skin, 4 donors. **b**, Distribution of methylation at the first 3,000,000 CH sites of chromosome 1, stratified by sample (3 samples from three donors per cell type) and sequencing library. **c**, Distribution of CpG-wise coverage values (3 samples from three donors per cell type). **d**, DNA Methylation in regions belonging to methylation-level cell type signatures with at least 10 regions. Rows correspond to signature regions; columns correspond to samples from individual donors (n = 3 donors per cell type). Numbers on the left indicate the number of regions in each signature category. Parts of this panel are duplicated from Fig. 1f and included for the sake of completeness. Data are representative of three or more independent experiments with three or more individual donors.

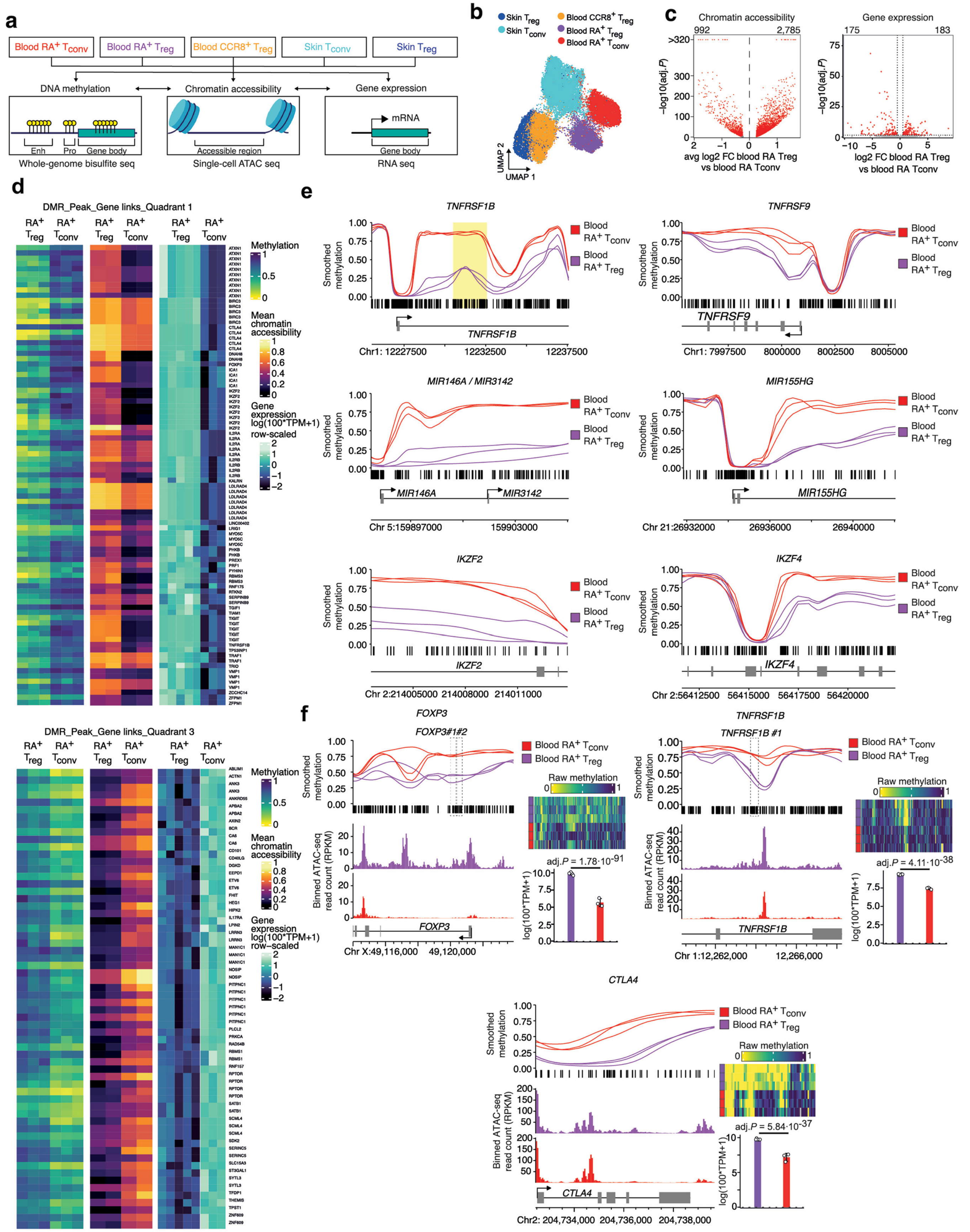

Extended Data Fig. 2 | See next page for caption.

Extended Data Fig. 2 | Details and examples of the 'core naïve T_{reg}' signature. **a**, Schematic of the study design, describing that blood CD45RA$^+$ T_{conv} cells, blood CD45RA$^+$ T_{reg} cells, blood CCR8$^+$ T_{reg} cells, skin T_{conv} cells and skin T_{reg} cells were analyzed with respect to their DNA methylation, chromatin accessibility and gene expression. Schematic generated using BioRender.com. **b**, UMAP showing scATAC-seq data of the analyzed cell types (encompassing 2 donors per cell type). **c**, Volcano plots for differential analyses on the chromatin accessibility and gene expression level (corresponding to heat maps in Fig. 2a). Features shown in red are considered statistically significant. Numbers at the top indicate the numbers of features displaying statistical significance. *P* values for chromatin accessibility, two-tailed likelihood ratio test (see Methods, n = 5,687 blood CD45RA$^+$ T_{reg} cells, 6,531 blood CD45RA$^+$ T_{conv} cells), adjusted using Bonferroni correction; *P* values for gene expression, two-tailed Wald test based on the raw count matrix as implemented in DESeq2, using donor ID as additional covariate (see Methods; n = 5 T_{reg} cell donors, 3 T_{conv} cell donors), adjusted using Benjamini-Hochberg correction. **d**, Methylation (left), chromatin accessibility (middle) and gene expression (right) of features in DMR-peak-gene links, stratified by quadrant (see Fig. 2b). Labels on the right indicate the genes in each DMR-peak-gene link. Parts of this panel are duplicated from Fig. 2a as the same features are shown. **e**, Methylation for selected genomic regions. Highlighted regions mark DMRs. Vertical lines at the bottom of the methylation tracks mark CpG sites. **f**, Smoothed methylation and chromatin accessibility for selected DMR-peak-gene links together with corresponding raw methylation for each shown CpG site (top right heat maps; rows indicate donors; columns indicate CpG sites; gray fields indicate missing values) and expression of the associated gene (bottom right bar charts; mean ± s.d.). Highlighted regions mark DMRs (methylation tracks) and differential peaks (accessibility tracks). Vertical lines at the bottom of the methylation tracks mark CpG sites. Dashed boxes mark the locations of amplicons used for validation of methylation differences. Gene expression *P* values, two-tailed Wald test based on the raw count matrix as implemented in DESeq2, using donor ID as additional covariate (see Methods; n = 5 T_{reg} cell donors, 3 T_{conv} cell donors) with Benjamini-Hochberg correction. Data are representative of two or more independent experiments with two or more individual donors.

https://doi.org/10.1038/s41590-025-02210-x

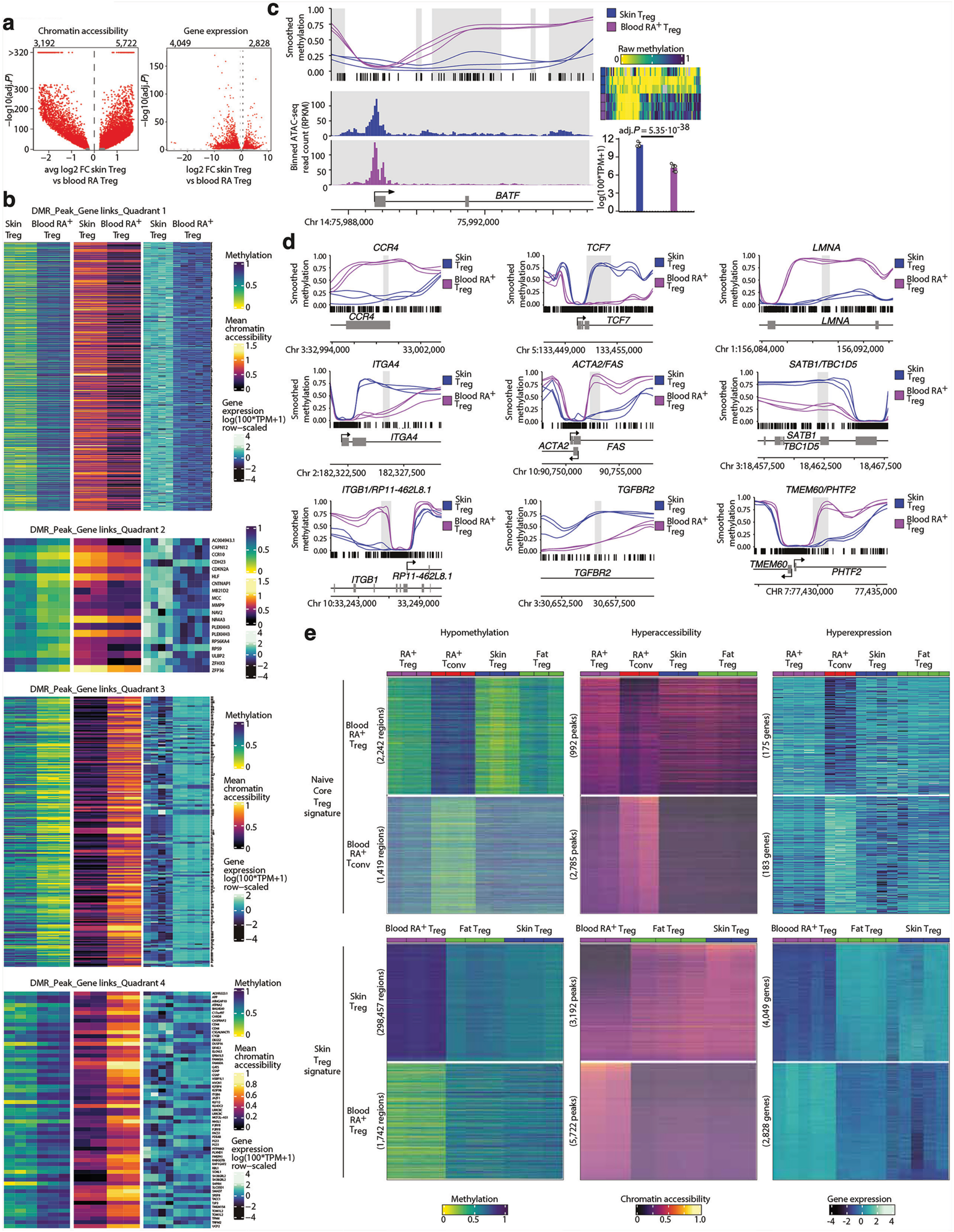

Extended Data Fig. 3 | See next page for caption.

Extended Data Fig. 3 | Details and examples of the 'skin T_{reg}' signature. **a**, Volcano plots for differential analyses on the chromatin accessibility and gene expression level (corresponding to heat maps in Fig. 3a). Features shown in red are considered statistically significant. Numbers at the top indicate the numbers of features displaying statistical significance. *P* values for chromatin accessibility, two-tailed likelihood ratio test (see Methods, n = 4,091 skin T_{reg} cells, 5,687 blood CD45RA$^+$ T_{reg} cells), adjusted using Bonferroni correction; *P* values for gene expression, two-tailed Wald test based on the raw count matrix as implemented in DESeq2 (see Methods; n = 4 skin T_{reg} cell donors, 5 blood CD45RA$^+$ T_{reg} cell donors; unpaired sample structure), adjusted using Benjamini-Hochberg correction. **b**, Methylation (left), chromatin accessibility (middle) and gene expression (right) of features in DMR-peak-gene links, stratified by quadrant (see Fig. 3b). Labels on the right indicate the genes in each DMR-peak-gene link. Parts of this panel are duplicated from Fig. 3a as the same features are shown. **c**, Smoothed methylation and chromatin accessibility for a selected DMR-peak-gene link together with corresponding raw methylation for each shown CpG site (top right heat map; rows indicate donors; columns indicate CpG sites; gray fields indicate missing values) and expression of the associated gene (bottom right bar chart; mean ± s.d.). Highlighted regions mark DMRs (methylation track) and differential peaks (accessibility track). Vertical lines at the bottom of the methylation track mark CpG sites. Dashed boxes mark the locations of amplicons used for validation of methylation differences. Gene expression *P* value, two-tailed Wald test (see Methods; n = 4 skin donors, 5 blood donors) with Benjamini-Hochberg correction. Expression bar charts are duplicated from Fig. 5 as they correspond to the same gene. **d**, Methylation for selected genomic regions. Highlighted regions mark DMRs. Vertical lines at the bottom of the methylation tracks mark CpG sites. **e**, DMRs (left), differentially accessible peaks (middle) and differentially expressed genes (right; row-scaled) between blood CD45RA$^+$ T_{reg} cells, blood CD45RA$^+$ T_{conv} cells, shown together with corresponding values in skin T_{reg} cells and fat T_{reg} cells ('core naïve T_{reg}' signature, upper panel), and between blood CD45RA$^+$ T_{reg} cells, fat T_{reg} cells and skin T_{reg} cells ('skin T_{reg}' signature, lower panel). Rows indicate genomic regions (left, middle) or genes (right). Columns indicate samples from individual donors, with n = 3 donors for methylation data, n = 2 skin T_{reg} / blood CD45RA$^+$ T_{reg} / blood CD45RA$^+$ T_{conv} donors and 3 fat T_{reg} donors for accessibility data, or n = 3 blood CD45RA$^+$ T_{conv} donors, 4 skin T_{reg} donors and 5 blood CD45RA$^+$ T_{reg} / fat T_{reg} donors for gene expression data. Parts of this panel are duplicated from Figs. 2a and 3a as the same features are shown. Data are representative of two or more independent experiments with two or more individual donors.

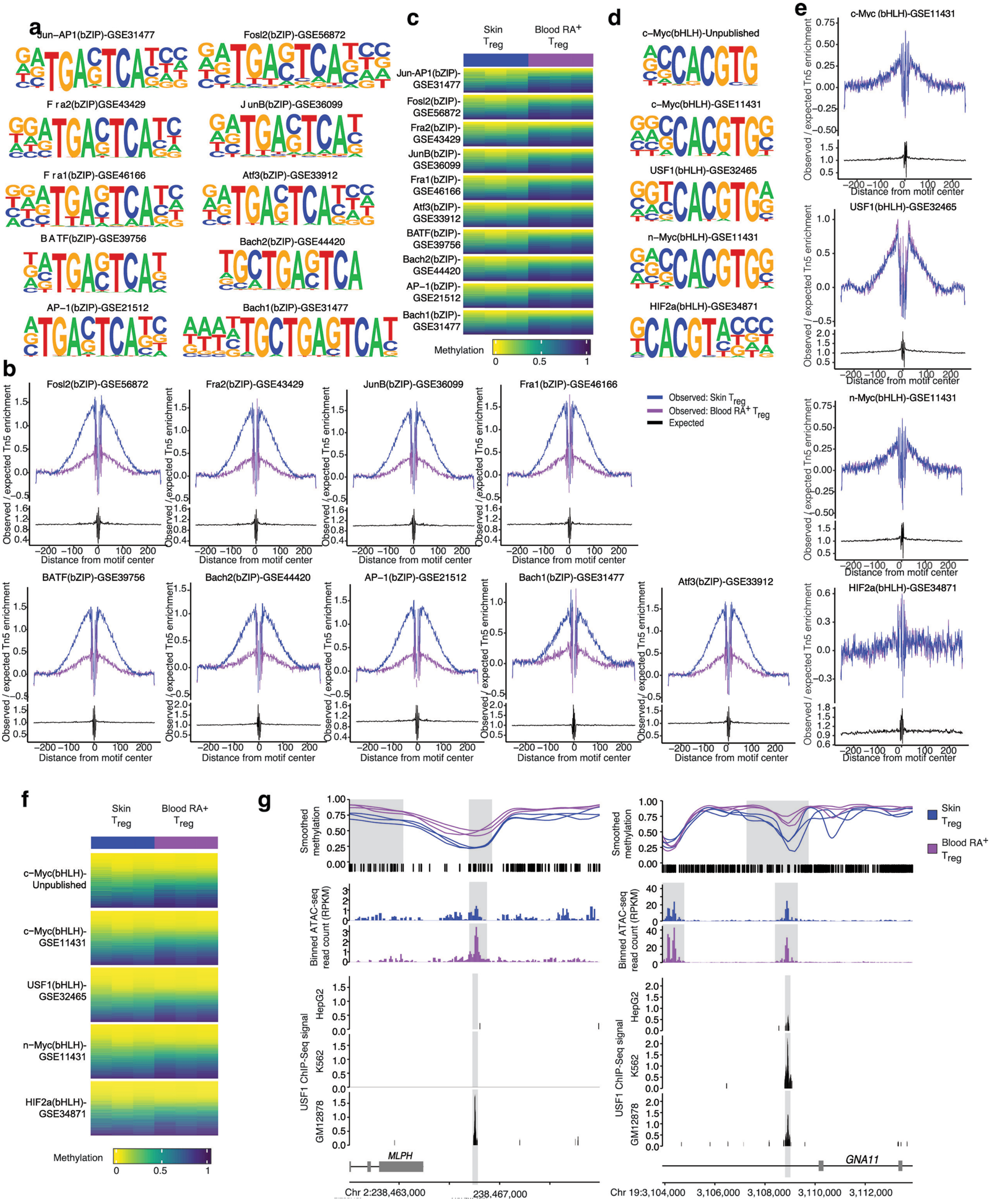

Extended Data Fig. 4 | See next page for caption.

Extended Data Fig. 4 | Details for transcription factor results with respect to skin adaptation of T_{reg} cells. a, Logos for the bZIP motifs highlighted in Fig. 4a (obtained from homer). **b**, Chromatin accessibility around genomic sites for additional bZIP motifs. **c**, Methylation (each row corresponds to a motif site ± 200 bases, each column corresponds to one of 3 donors, donors for skin Treg cells and blood CD45RA$^+$ T_{reg} cells are unpaired) around genomic sites for bZIP motifs (n = 29,813 motif sites, 29,546 motif sites, 28,220 motif sites, 28,693 motif sites, 26,628 motif sites, 30,426 motif sites, 27,920 motif sites, 23,868 motif sites, 28,863 motif sites and 18,907 motif sites, respectively, from top to bottom). **d**, Logos for the bHLH motifs highlighted in Fig. 4c (obtained from homer). **e**, Chromatin accessibility around genomic sites for additional bHLH motifs. **f**, Methylation (each row corresponds to a motif site ± 200 bases, each column corresponds to one of 3 donors, donors for skin Treg cells and blood CD45RA$^+$ T_{reg} cells are unpaired) around genomic sites for bHLH motifs. n = 12,050 motif sites, 11,186 motif sites, 9,358 motif sites, 11,415 motif sites and 3,004 motif sites, respectively, from top to bottom). **g**, Methylation, chromatin accessibility and USF1 ChIP-seq signal from three cell lines around interesting motif sites for USF1. Highlighted regions correspond to selected DMRs (methylation tracks), scATAC-seq peaks (chromatin accessibility tracks) and USF1 motif sites (motif ± 100 bases; ChIP-seq and gene tracks). Vertical lines at the bottom of the methylation tracks mark CpG sites. Parts of this panel are duplicated from Fig. 4g as they display the same genomic regions but focus on a different transcription factor. Data are representative of two or more independent experiments with two or more individual donors.

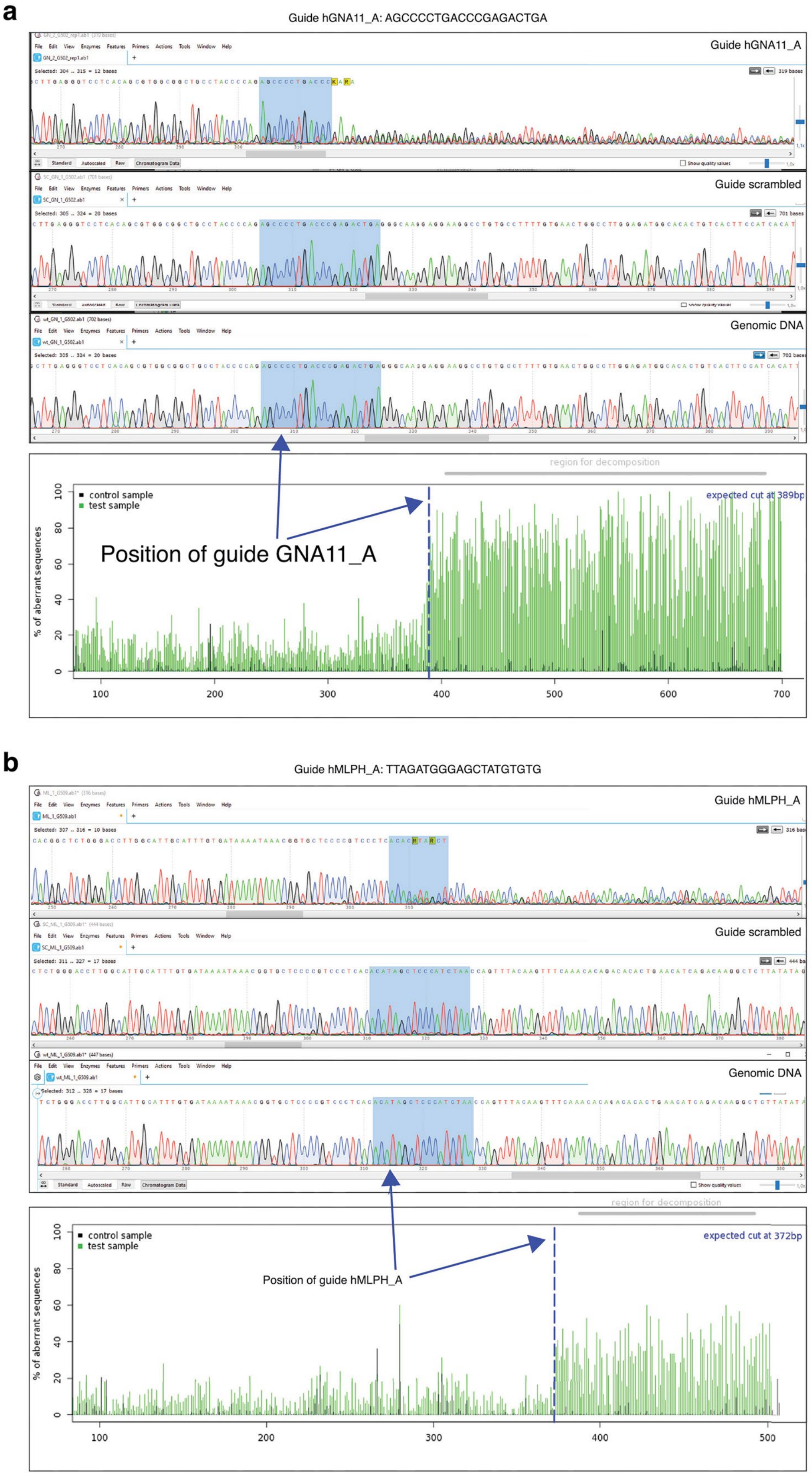

Extended Data Fig. 5 | See next page for caption.

Extended Data Fig. 5 | Targeting of GNA11_A guide and MLPH_A guide. a, Sanger sequencing of *GNA11* locus in human CD4$^+$ T cells after CRISPR-Cas9 targeting with guide GNA11_A (top), scrambled control (middle) and not-CRISPRed genomic DNA (bottom) of human T cells. Blue boxes indicate position of GNA11_A guide. Lower part, percentage of aberrant sequences (not matching to genomic control sample). Dashed blue line indicates position of GNA11_A guide. **b**, Sanger sequencing of *MLPH* locus in human CD4$^+$ T cells after CRISPR-Cas9 targeting with guide MLPH_A (top), scrambled control (middle) and not-CRISPRed genomic DNA (bottom) of human T cells. Blue boxes indicate position of MLPH_A guide. Lower part, percentage of aberrant sequences (not matching to genomic control sample). Dashed blue line indicates position of MLPH_A guide.

a

Hypomethylation/Hyperaccessibility/Hyperexpression in Blood RA$^+$ T$_{reg}$

Blood CCR8$^+$ T$_{reg}$ position	Methylation	Accessibility	Expression
Closer to skin T$_{reg}$	1,571	3,221	1,006
Closer to blood RA$^+$ T$_{reg}$	171	2,501	1,822

Hypomethylation/Hyperaccessibility/Hyperexpression in Skin T$_{reg}$

Blood CCR8$^+$ T$_{reg}$ position	Methylation	Accessibility	Expression
Closer to skin T$_{reg}$	292,033	2,064	1,982
Closer to blood RA$^+$ T$_{reg}$	6,424	1,128	2,062

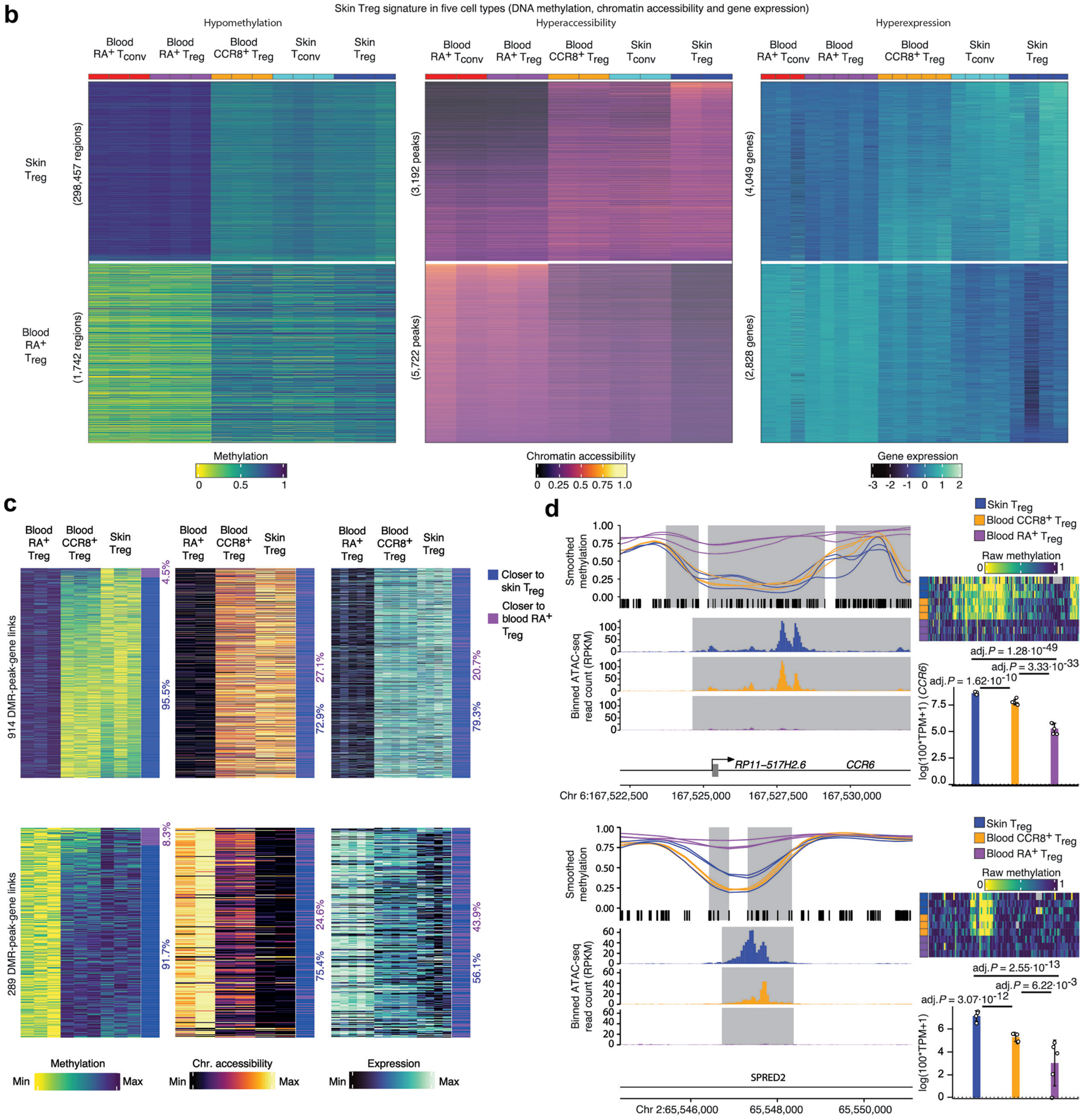

Extended Data Fig. 6 | See next page for caption.

Extended Data Fig. 6 | The 'Skin T_{reg}' signature across many cell types and the molecular positioning of blood CCR8$^+$ T_{reg} cells. a, Feature numbers (*that is* numbers of DMRs, differentially accessible peaks and differentially expressed genes) underlying blood CCR8$^+$ T_{reg} cell positionings shown in Fig. 5a. **b**, Methylation, chromatin accessibility and gene expression for the 'skin T_{reg}' signature in skin T_{reg} cells, skin T_{conv} cells, blood CCR8$^+$ T_{reg} cells, blood CD45RA$^+$ T_{reg} cells and blood CD45RA$^+$ T_{conv} cells. Parts of this panel are duplicated from Fig. 3a as the same features are shown. **c**, Methylation (left), chromatin accessibility (middle) and gene expression (right) of features that belong to DMR-peak-gene links with hypomethylation in skin T_{reg} cells (top) or blood CD45RA$^+$ T_{reg} cells (bottom). Columns indicate samples from different donors (left, right) or donor-wise mean accessibility across cells (middle). n = 3 donors on the methylation level, 2 donors on the accessibility level, 4 (skin T_{reg}) and 5 (blood CCR8$^+$ T_{reg}, blood CD45RA$^+$ T_{reg}) donors on the expression level. Annotation bars on the right of each heat map indicate whether blood CCR8$^+$ T_{reg} cells are closer to skin T_{reg} cells or closer to blood CD45RA$^+$ T_{reg} cells with respect to a feature (based on the mean across donors; see Methods for details). Parts of this panel are duplicated from Fig. 5a as the same features are shown. **d**, Smoothed methylation and chromatin accessibility in regions where chromatin accessibility of the overlapping peak places blood CCR8$^+$ T_{reg} cells closer to skin T_{reg} cells (top) and closer to blood CD45RA$^+$ T_{reg} cells (bottom). These regions are shown together with corresponding raw methylation for each displayed CpG site (top right heat maps; rows indicate donors; columns indicate CpG sites; gray fields indicate missing values) and expression of the associated gene (bottom right bar charts; mean ± s.d.). Highlighted regions mark DMRs (methylation tracks) and differential peaks (accessibility tracks). Vertical lines at the bottom of the methylation tracks mark CpG sites. *P* values, two-tailed Wald test based on the raw count matrix as implemented in DESeq2 (see Methods; n = 4 skin T_{reg} donors, 5 blood CCR8$^+$ T_{reg} donors, 5 blood CD45RA$^+$ T_{reg} donors; unpaired sample structure) with Benjamini-Hochberg correction. Data are representative of two or more independent experiments with two or more individual donors.

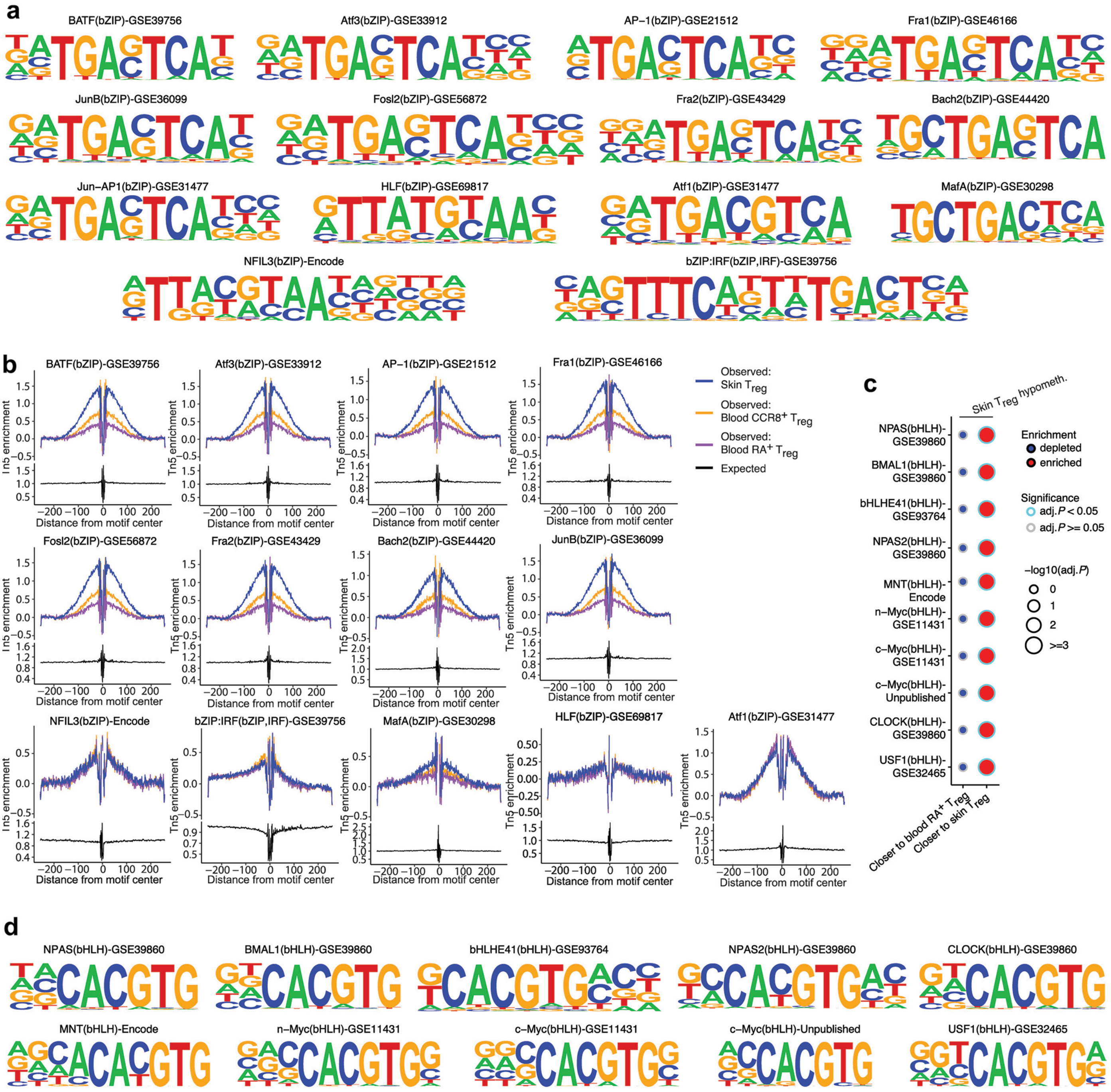

Extended Data Fig. 7 | Details of motif analysis regarding the positioning of blood CCR8$^+$ T$_{reg}$ cells. a, Logos for motifs highlighted in Fig. 5d (obtained from homer). **b**, Chromatin accessibility around genomic sites for additional bZIP motifs. Parts of these plots are duplicated from Extended Data Fig. 4 as they correspond to the same motifs. **c**, Enrichment of bHLH motifs in methylation-level region sets defined by different blood CCR8$^+$ T$_{reg}$ cell positionings. *P* values, one-tailed binomial test implemented in homer assessing enrichment of motif sites among the region sets compared to background sets of random regions (see Methods; n = 6,424 DMRs and 292,033 DMRs for columns 1 and 2, respectively) with Benjamini-Hochberg correction. **d**, Motifs highlighted in **c** (obtained from homer). Parts of this figure are duplicated from Extended Data Fig. 5 as they correspond to the same motifs. Data are representative of two or more independent experiments with two or more individual donors.

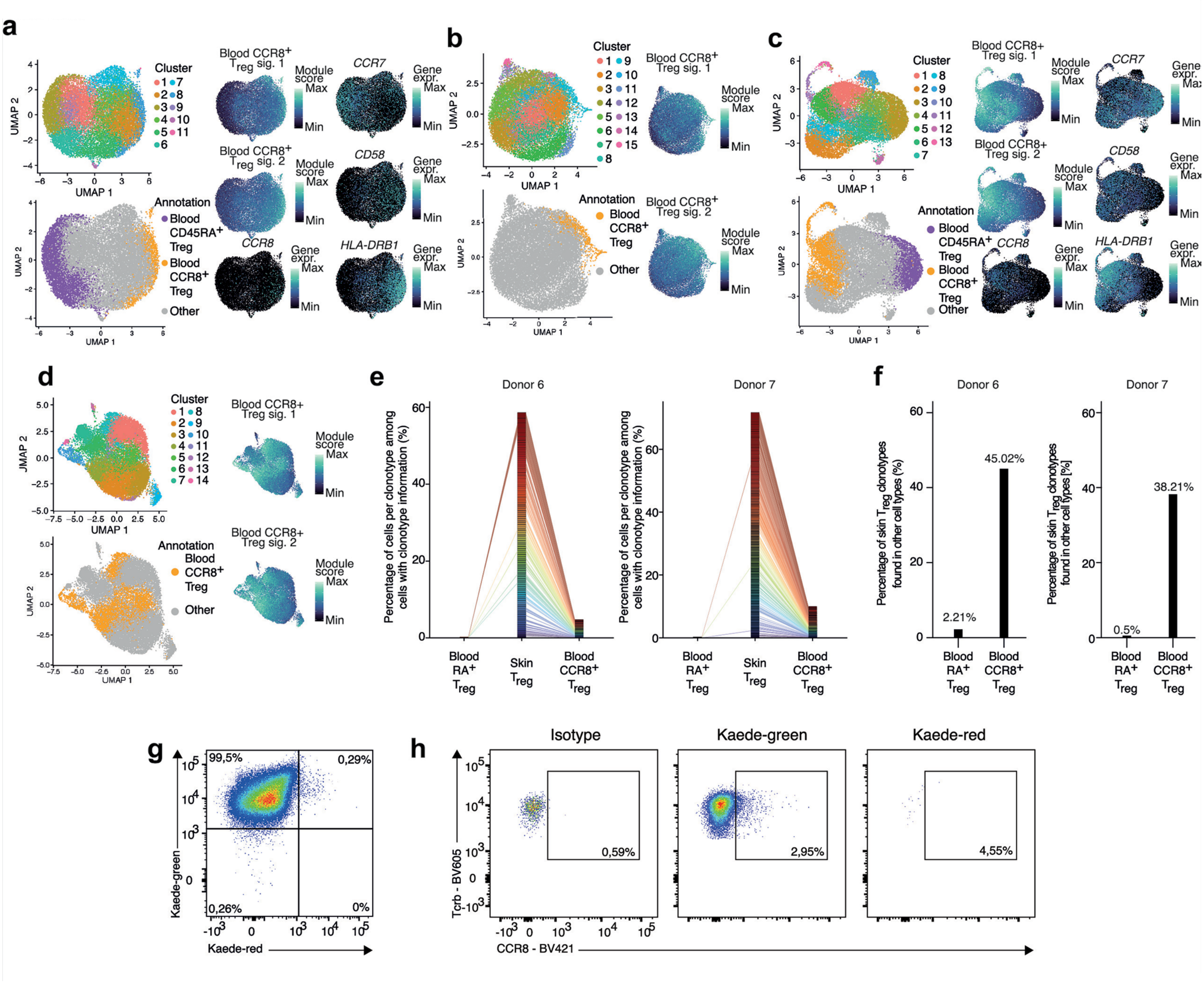

Extended Data Fig. 8 | Details of scRNA-seq/scTCR-seq data analysis and Kaede mice experiments regarding the positioning of blood CCR8$^+$ T_{reg} cells. **a**–**d**, UMAP representations of cells from scRNA-seq/scTCR-seq, showing clusters and cell type annotation next to gene expression and signature values underlying the annotation. Data correspond to blood T_{reg} cells from TCR Donor 6 (sample 28; **a**), blood CD45RO$^+$ T_{reg} cells from TCR Donor 6 (sample 29, **b**), blood T_{reg} cells from TCR Donor 7 (sample 24, **c**) and blood CD45RO$^+$ T_{reg} cells from TCR Donor 7 (sample 25, **d**). Blood CCR8$^+$ T_{reg} signature 1 defines blood CCR8$^+$ T_{reg} cells against blood CD45RA$^+$ T_{reg} cells. Blood CCR8$^+$ T_{reg} signature 2 defines blood CCR8$^+$ T_{reg} cells against blood CD45RO$^+$ (memory) T_{reg} cells. For details regarding the annotation, see the Methods section. **e**, Stacked bar charts showing TCR clonotype sharing between blood CD45RA$^+$ T_{reg} cells, skin T_{reg} cells and blood CCR8$^+$ T_{reg} cells. Bar sections indicate the percentage of cells belonging to a particular clonotype. Connections between bar sections indicate that a clonotype was found in two cell types. All clonotypes that appear in skin T_{reg} cells and contain at least one TCR-α and TCR-β chain are shown (271 clonotypes from TCR Donor 6, 602 clonotypes from TCR Donor 7). **f**, Percentages of skin T_{reg} cell clonotypes that were also found among blood CD45RA$^+$ T_{reg} cells and blood CCR8$^+$ T_{reg} cells. **g**, Kaede-green and Kaede-red expression in skin-draining-lymph-node-derived T_{reg} cells of Kaede mice 6 days after photoconversion of skin. Cells were pre-enriched for CD25 and gated on size, viability, TCR-β, CD4, CD25 and GITR. Concatenated data of 7 mice. **h**, CCR8 expression was measured in T_{reg} and T_{conv} cells 6 days after light exposure of skin of Kaede mice. Cells were harvested from LN and enriched for CD25 expression. Shown here are the T_{conv} cells present in CD25-enriched fractions, results for T_{reg} cells are shown in the main figure. Concatenated data of 7 mice. Data are representative of two or more independent experiments with two or more individual donors/mice.

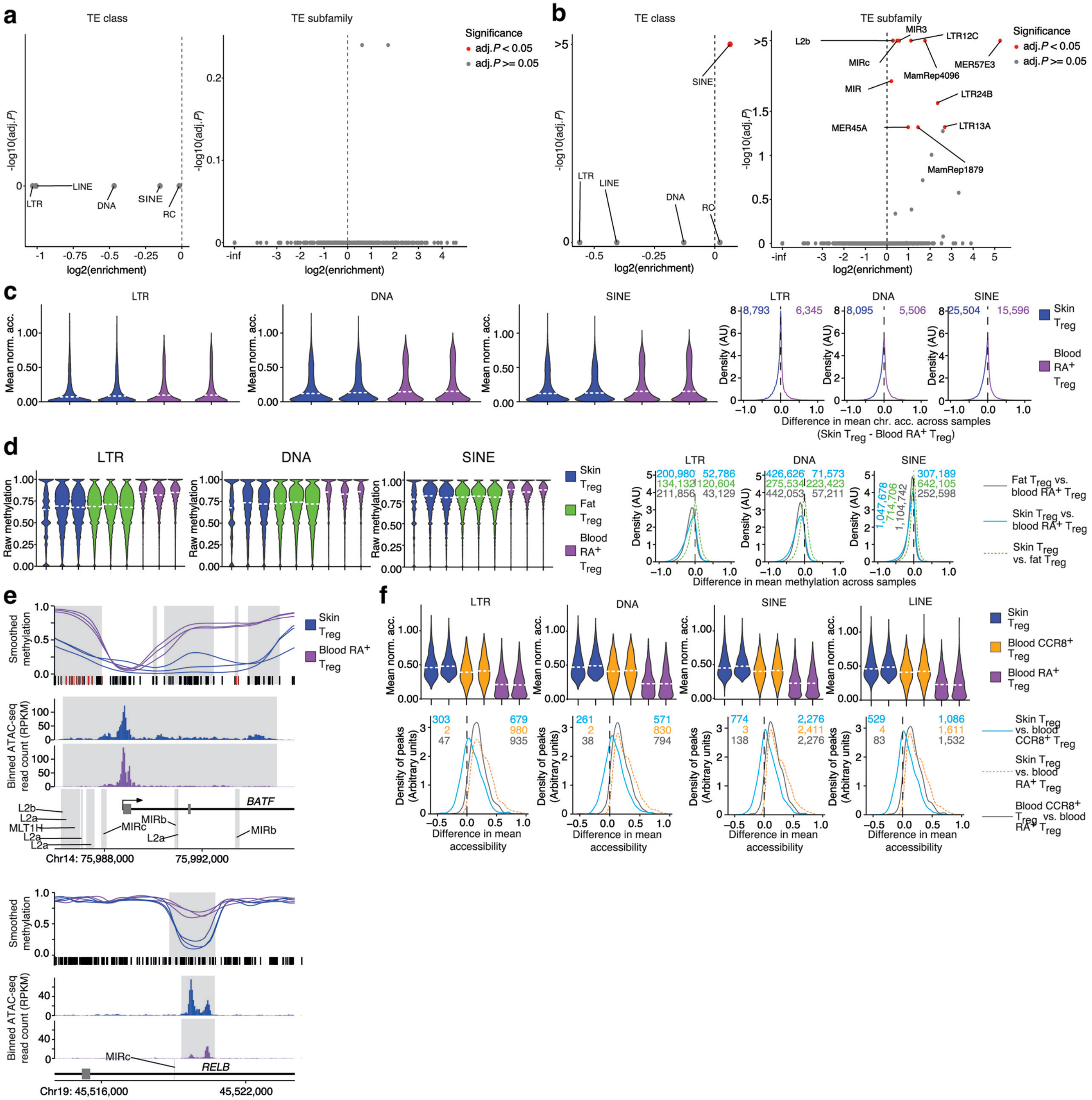

Extended Data Fig. 9 | The contribution of TEs to the epigenetic landscape of skin T_{reg} cells and blood CCR8$^+$ T_{reg} cells. a, **b**, Enrichment of TE classes (left) and subfamilies (right) in regions hypomethylated (**a**) or hyperaccessible (**b**) in blood CD45RA$^+$ T_{reg} cells. P values: one-tailed permutation test assessing enrichment of TE insertion sites among DMRs or peaks (see Methods) based on 1,742 DMRs (**a**) and 5,722 differential peaks (**b**) displayed in Fig. 3 with Benjamini-Hochberg correction. **c**, Left, Chromatin accessibility of peaks overlapping with annotated LTR-TE, DNA-TE and SINE insertion sites (n = 2 donors per cell type). White horizontal lines inside violins indicate medians across all peaks. Right, Distribution of differences in mean accessibility (across the two donors) between skin T_{reg} cells and blood CD45RA$^+$ T_{reg} cells for each peak. Numbers indicate how many insertion sites displayed differences below and above 0. **d**, Left, Methylation of annotated LTR, DNA-TE and SINE insertion sites as in c with skin T_{reg}, fat T_{reg} and blood CD45RA$^+$ T_{reg} (n = 3 donors per cell type). White horizontal lines inside violins indicate medians across all insertion sites. Right, Distribution of differences in mean methylation (across the three donors) between any two cell types for each insertion site. Numbers indicate how many insertion sites displayed differences below and above 0. **e**, Smoothed methylation and chromatin accessibility around selected TE insertion sites. Highlighted regions mark DMRs (methylation tracks), differential peaks (accessibility tracks) and TE insertion sites overlapping with DMRs (only TE subfamilies enriched among the DMRs; gene tracks). Vertical lines at the bottom of the methylation tracks mark CpG sites (CpG sites overlapping with TEs are shown in red). TE labels correspond to TE subfamilies. Parts of these plots are duplicated from Fig. 3 and Extended Data Fig. 3 as they show the same genomic regions. **f**, Top, Chromatin accessibility of peaks displaying hyperaccessibility in skin T_{reg} cells and overlapping with DNA-TE, LINE, LTR-TE and SINE insertion sites (n = 2 donors per cell type). White horizontal lines inside violins indicate medians across all peaks. Bottom, Distribution of differences in mean accessibility (across the two donors) between any two cell types for each peak. Numbers indicate how peaks displayed differences below and above 0. Data are representative of two or more independent experiments with two or more individual donors.

https://doi.org/10.1038/s41590-025-02210-x

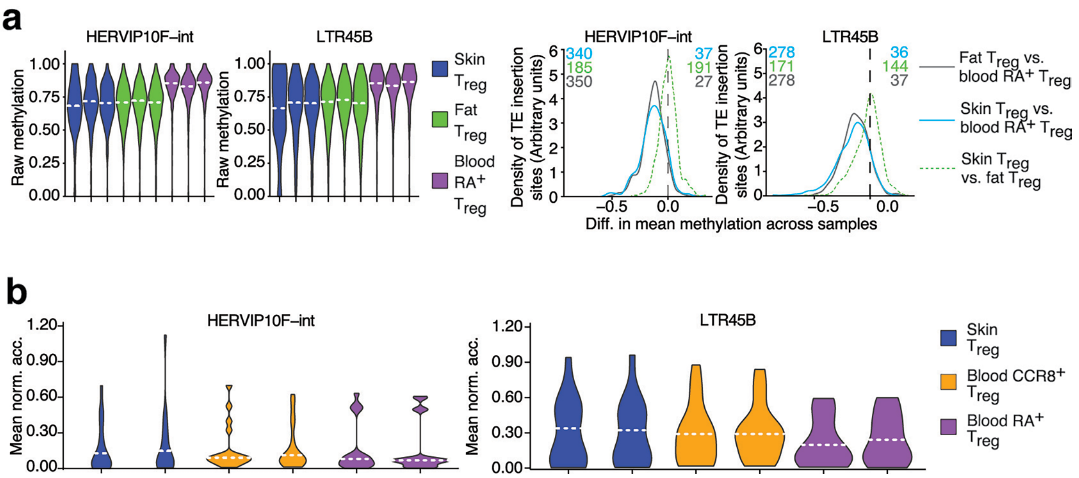

Extended Data Fig. 10 | Methylation and accessibility of HERVIP10F-int and LTR45B insertion sites. a, Left, Methylation of annotated HERVIP10F-int and LTR45B insertion sites in skin T_{reg}, fat T_{reg} and blood CD45RA$^+$ T_{reg} cells (n = 3 donors per cell type). White horizontal lines inside violins indicate medians across all insertion sites. Right, Distribution of differences in mean methylation (across the three donors) between any two cell types for each insertion site. Numbers indicate how many insertion sites displayed differences below and above 0. **b**, Chromatin accessibility of peaks overlapping with annotated HERVIP10F-int and LTR45B insertion sites in skin T_{reg}, blood CCR8$^+$ T_{reg} and blood CD45RA$^+$ T_{reg} cells. White horizontal lines inside violins indicate medians across all peaks. Data are representative of two or more independent experiments with two or more individual donors.

nature portfolio

Corresponding author(s): Michael Delacher, Markus Feuerer

Last updated by author(s): Jun 8, 2025

Reporting Summary

Statistics

For all statistical analyses, confirm that the following items are present in the figure legend, table legend, main text, or Methods section.

n/a	Confirmed	
☐	☒	The exact sample size (*n*) for each experimental group/condition, given as a discrete number and unit of measurement
☐	☒	A statement on whether measurements were taken from distinct samples or whether the same sample was measured repeatedly
☐	☒	The statistical test(s) used AND whether they are one- or two-sided *Only common tests should be described solely by name; describe more complex techniques in the Methods section.*
☒	☐	A description of all covariates tested
☐	☒	A description of any assumptions or corrections, such as tests of normality and adjustment for multiple comparisons
☐	☒	A full description of the statistical parameters including central tendency (e.g. means) or other basic estimates (e.g. regression coefficient) AND variation (e.g. standard deviation) or associated estimates of uncertainty (e.g. confidence intervals)
☐	☒	For null hypothesis testing, the test statistic (e.g. *F*, *t*, *r*) with confidence intervals, effect sizes, degrees of freedom and *P* value noted *Give P values as exact values whenever suitable.*
☒	☐	For Bayesian analysis, information on the choice of priors and Markov chain Monte Carlo settings
☒	☐	For hierarchical and complex designs, identification of the appropriate level for tests and full reporting of outcomes
☐	☒	Estimates of effect sizes (e.g. Cohen's *d*, Pearson's *r*), indicating how they were calculated

Our web collection on statistics for biologists contains articles on many of the points above.

Software and code

Policy information about availability of computer code

Data collection	Bisulfite sequencing data was generated by Novogene Inc. We received sequencing data in Fastq format.
Data analysis	We did not develop any new software but used functionality that is publicly available via software packages as described in the Methods section. For FACS, we used the following software: FACSDiva v8.0.2 BD FlowJo v10.6.2 and v10.10.0 For visualization of laboratory data, we used GraphPad Prism (v10.3.1 and v10.4.1). For analysis of sequencing data, we used the following software: bedtools v2.24.0 and v2.26.0 bismark v0.20.0 bowtie2 v2.2.4 and v2.3.5.1 BSgenome v1.58.0 BSgenome.Hsapiens.1000genomes.hs37d5 v0.99.1 BSgenome.Hsapiens.UCSC.hg19 v1.4.2 bsseq v1.26.0 BWA-MEM v0.7.8 circlize v0.4.13

cowplot v1.1.1
cutadapt v4.8
decoupleR v2.3.2
deeptools v3.5.1
DESeq2 v1.30.1
FASTX v0.0.13
GenomeInfoDb v1.26.7
harmony v0.1.0
homer v4.11
Homertools v4.7
methylCtools (custom version as described in the methods section)
msigdbr v7.4.1
PicardToold v1.78
Python v3.8.3
R v4.0.0
rtracklayer v1.50.0
sambamba v0.6.5
samtools v1.11.0
Seurat v4.0.1
SeuratObject v4.0.1
stats (base package linked to the employed version of R)
Signac v1.2.1
STAR v2.3
TEspeX v2.0.1
TFBSTools v1.28.0
Trimmomatic v0.30
zlib v2.1.12

Our wrapper code used for running this publicly available software is available on GitHub (https://github.com/DKFZ-ABI/hum_tistreg_methylation), can be accessed without restrictions and is reusable under a CC BY-NC-SA 4.0 license..

For manuscripts utilizing custom algorithms or software that are central to the research but not yet described in published literature, software must be made available to editors and reviewers. We strongly encourage code deposition in a community repository (e.g. GitHub). See the Nature Portfolio guidelines for submitting code & software for further information.

Data

Policy information about availability of data

All manuscripts must include a data availability statement. This statement should provide the following information, where applicable:

- Accession codes, unique identifiers, or web links for publicly available datasets
- A description of any restrictions on data availability
- For clinical datasets or third party data, please ensure that the statement adheres to our policy

Human whole-genome bisulfite sequencing data has been deposited in the European Genome Phenome Archive (EGA; accession number EGAD50000001022) and will be available under controlled access. File name conventions are: Labels 1-3: Skin Treg cell samples, Labels 4-6: Skin Tconv cell samples, Labels 13-15: Blood CCR8 + Treg cell samples, Labels 16-18: Blood CD45RA+ Treg cell samples, Labels 19-21: Blood CD45RA+ Tconv cell samples. Access will require application to a data access committee and will require a data sharing agreement. CpG-level methylation data have been deposited in the Gene Expression Omnibus (GEO; accession number: GSE286948) and will be available without restrictions.
We used data sets that were already utilized in our previous study10. Corresponding raw sequencing data had been deposited in the EGA (accession numbers: EGAD00001006779 for scATAC-seq; EGAD00001007665 and EGAD00001007661 for sRNA/TCR seq; EGAD00001007663 and EGAD00001007665 for bulk RNA-seq; access requires application to a data access committee and a data sharing agreement.). The versions of the corresponding processed data that were used in this study are available on Zenodo (accession numbers: 14999322 for scATA-seq; 14999788 for scRNA/TCR-seq; 14999989 for bulk RNA-seq).
In addition, we used several data sets from other sources. The hs37d5 reference genome is publicly available under https://ftp.ncbi.nlm.nih.gov/1000genomes/ftp/technical/reference/phase2_reference_assembla_sequence. The GRCh37 reference genome is available under http://ftp.ensembl.org/pub/release-75/fasta/homo_sapiens/dna. The human genome 38 is available under https://hgdownload.soe.ucsc.edu/goldenPath/hg38/chromosomes. Gencode V19 annotations are available under https://ftp.ebi.ac.uk/pub/databases/gencode/Gencode_human/release_19. We downloaded locations of CpG islands ("cpgIslandExt" data set) from https://hgdownload.cse.ucsc.edu/goldenPath/hg19/database. Hallmark gene sets are available via the msigdbr function (species = 'Homo sapiens', category = 'H') from the msigdbr package. ChIP-seq data for c-Myc and USF1 are publicly available in the Gene Expression Omnibus (accession numbers: GSM822291, GSM822310, GSM822290, GSM803527, GSM803441, GSM803347). RepeatMasker annotations are available under https://hgdownload.soe.ucsc.edu/goldenPath/hg19/database/rmsk.txt.gz. We downloaded consensus sequences of TEs from the Giri Repbase72 (https://www.girinst.org/repbase/). Sequences of human long non-coding RNAs are available under https://ftp.ebi.ac.uk/pub/databases/gencode/Gencode_human/release_19/gencode.v19.lncRNA_transcripts.fa.gz.
Source data for this study are available in Zenodo (accession number: 15607737).

Research involving human participants, their data, or biological material

Policy information about studies with human participants or human data. See also policy information about sex, gender (identity/presentation), and sexual orientation and race, ethnicity and racism.

Reporting on sex and gender	All donors of bisulfite sequencing samples, bulk RNA-seq samples, scATAC-seq samples, scRNA/TCR-seq samples and FACS-only samples were female. Due to sex-specific X-chromosomal incactivation, we chose to only include samples from female donors in our analysis. All donors of amplicon sequencing samples were male. Sex of donors for CRISPR analyses is unknown.

Reporting on race, ethnicity, or other socially relevant groupings	Not applicable
Population characteristics	Tissue samples for whole-genome bisulfite sequencing and bulk RNA-seq: For whole-genome bisulfite sequencing, samples from three donors per cell type were processed. We analyzed skin Treg cells from Tissue Donor 7, Tissue Donor 10 and Tissue Donor 11 (median age: 52; range: 41-53), skin Tconv cells from Tissue Donor 7, Tissue Donor 10 and Tissue Donor 11 (ages as for skin Treg cells) and fat Treg cells from Tissue Donor 6, Tissue Donor 7 and Tissue Donor 8 (age not available for each donor). For bulk RNA sequencing, we profiled samples from 4-5 donors per cell type. We analyzed skin Treg cells from Tissue Donor 7, Tissue Donor 8, Tissue Donor 10 and Tissue Donor 11 (age not available for each donor), skin Tconv cells from Tissue Donor 7, Tissue Donor 8, Tissue Donor 10 and Tissue Donor 11 (age not available for each donor) and fat Treg cells from Tissue Donor 5, Tissue Donor 6, Tissue Donor 7, Tissue Donor 8 and Tissue Donor 9 (age not available for each donor). This bulk RNA-seq data had been published (ref. 10). Blood samples for whole-genome bisulfite sequencing and bulk RNA-seq: Age unknown FACS-only analyses: For statistical analysis, we utilized samples from “FACS donor 1”, “FACS donor 2”, “FACS donor 3”, “FACS donor 4”, “FACS donor 5” and “FACS donor 6” (median age: 46; range: 31-61). For exemplification of our gating strategy, we utilized samples from “FACS Donor 7” (age unknown). CRISPR analyses: Age unknown Amplicon analyses: Age unknown scATAC-seq: scATAC-seq data (ref. 10) contained data on CD4+ T cells from blood, skin and subcutaneous fat of 5 healthy female donors (blood from ATAC Donor 1 and ATAC Donor 2, skin from ATAC Donor 4 and ATAC Donor 5 and fat from ATAC Donor 3, ATAC Donor 4 and ATAC Donor 5) with an average age of 44.6 years (±14; range from 26 to 56, ages for individual donors unknown). scRNA/scTCR analyses: Age unknown
Recruitment	Recruitment at the University Hospital Regensburg. We are not aware of any potential self-selection bias or other biases that may be present and impact the results.
Ethics oversight	The study was approved by the local ethics committee at Regensburg University, Germany (reference numbers 19-1453-101, 19-1414-101 and 19-1614-101).

Note that full information on the approval of the study protocol must also be provided in the manuscript.

Field-specific reporting

Please select the one below that is the best fit for your research. If you are not sure, read the appropriate sections before making your selection.

☒ Life sciences ☐ Behavioural & social sciences ☐ Ecological, evolutionary & environmental sciences

For a reference copy of the document with all sections, see nature.com/documents/nr-reporting-summary-flat.pdf

Life sciences study design

All studies must disclose on these points even when the disclosure is negative.

Sample size	Human skin and subcutaneous adipose (fat) tissue used for whole-genome bisulfite sequencing and RNA-sequencing was obtained from 7 healthy female donors (termed ”Tissue Donor 5”, “Tissue Donor 6”, “Tissue Donor 7”, “Tissue Donor 8”, “Tissue Donor 9”, “Tissue Donor 10” and “Tissue Donor 11”) For whole-genome bisulfite sequencing, samples from three donors per cell type were processed. We analyzed skin Treg cells from Tissue Donor 7, Tissue Donor 10 and Tissue Donor 11, skin Tconv cells from Tissue Donor 7, Tissue Donor 10 and Tissue Donor 11 and fat Treg cells from Tissue Donor 6, Tissue Donor 7 and Tissue Donor 8. For bulk RNA sequencing, we profiled samples from 4-5 donors per cell type. We analyzed skin Treg cells from Tissue Donor 7, Tissue Donor 8, Tissue Donor 10 and Tissue Donor 11, skin Tconv cells from Tissue Donor 7, Tissue Donor 8, Tissue Donor 10 and Tissue Donor 11 and fat Treg cells from Tissue Donor 5, Tissue Donor 6, Tissue Donor 7, Tissue Donor 8 and Tissue Donor 9. This bulk RNA-seq data had been published (ref. 10). For flow cytometry analysis, blood and skin samples were obtained from seven healthy female donors. For statistical analysis, we utilized samples from “FACS donor 1”, “FACS donor 2”, “FACS donor 3”, “FACS donor 4”, “FACS donor 5” and “FACS donor 6”. For exemplification of our gating strategy, we utilized samples from “FACS Donor 7”. To obtain human blood samples for whole-genome bisulfite sequencing and RNA-sequencing, peripheral blood mononuclear cells for CD4+ T cell enrichment were isolated from leukocyte reduction chambers from 10 healthy female donors (termed “Blood donor 3”, “Blood donor 4”, “Blood donor 5”, “Blood donor 6”, “Blood donor 7”, “Blood donor 8”, “Blood Donor 9” and “Blood Donor 10”, “Blood Donor 11” and “Blood Donor 12”). For whole-genome bisulfite sequencing, samples from three donors per cell types were used (blood CD45RA+ Treg cells from Blood Donor 3, Blood Donor 4 and Blood Donor 5, blood CD45RA+ Tconv cells from Blood Donor 3, Blood Donor 4 and Blood Donor 5 and blood CCR8+ Treg cells from Blood Donor 6, Blood Donor 7 and Blood Donor 8). For bulk RNA-seq, we profiled 3-5 samples per cell type (Blood CD45RA+ Treg cells from Blood Donor 3, Blood Donor 4, Blood Donor 5, Blood Donor 9 and Blood Donor 10, Blood CD45RA+ Tconv cells from

Blood Donor 3, Blood Donor 4 and Blood Donor 5 and Blood CCR8+ Treg cells from Blood Donor 6, Blood Donor 7, Blood Donor 8, Blood Donor 11 and Blood Donor 12). This bulk RNA-seq data had been published (ref. 10). For CRISPR activation, we analyzed T cells from 6 donors. Cells from “CRISPR Donor 1”, “CRISPR Donor 2” and “CRISPR Donor 3” were used for the guide RNAs hMLPH_A and hGNA11; cells from “CRISPR Donor 4”, “CRISPR Donor 5” and “CRISPR Donor 6” were used for the guide RNA hMLPH_B. For amplicon-based bisulfite sequencing, we processed samples from six male donors. These donors were termed “Amplicon Donor 1”, “Amplicon Donor 2”, “Amplicon Donor 3”, “Amplicon Donor 4”, “Amplicon Donor 5” and “Amplicon Donor 6”.
In addition, we utilized public scATAC-seq and scRNA-seq/scTCR-seq data (ref. 10). scATAC-seq data contained data on CD4+ T cells from blood, skin and subcutaneous fat of 5 healthy female donors (blood from ATAC Donor 1 and ATAC Donor 2, skin from ATAC Donor 4 and ATAC Donor 5 and fat from ATAC Donor 3, ATAC Donor 4 and ATAC Donor 5). scRNA/TCR-seq data contained data on CD4+ T cells from blood, skin and subcutaneous fat of 2 heathy female donors (termed “TCR Donor 6” and “TCR Donor 7”).
Mouse experiments were based on 7 animals.
No statistical methods were used to pre-determine sample sizes but our sample sizes are similar to those reported in previous publications

Data exclusions

Within one bisulfite sequencing sample (skin Treg cells, Tissue Donor 7), one of two sequencing libraries exhibited exceptionally high CH methylation (Extended Data Fig. 1b). Thus, we suspected incomplete bisulfite conversion and consequenntly excluded this sequencing library. This criterion was not pre-established as the present study did not include formally defined exclusion criteria. However, the strong evidence for incomplete bisulfite conversion in the excluded sequencing library mandated this exclusion as incomplete bisulfite conversion would substantially falsify the resulting data.

Replication

We developed an amplicon-sequencing based strategy to verfify methylation data presented in Fig. 2.

Randomization

Human donors and mice were not assigned to different experimental groups. Thus, randomization was not applicable.

Blinding

Human donors and mice were not assigned to different experimental groups. Thus, blinding was not applicable and data collection and analysis were not performed blind to the conditions of the experiments

Reporting for specific materials, systems and methods

We require information from authors about some types of materials, experimental systems and methods used in many studies. Here, indicate whether each material, system or method listed is relevant to your study. If you are not sure if a list item applies to your research, read the appropriate section before selecting a response.

Materials & experimental systems

n/a	Involved in the study	
☐	☒	Antibodies
☒	☐	Eukaryotic cell lines
☒	☐	Palaeontology and archaeology
☐	☒	Animals and other organisms
☒	☐	Clinical data
☒	☐	Dual use research of concern
☒	☐	Plants

Methods

n/a	Involved in the study	
☒	☐	ChIP-seq
☐	☒	Flow cytometry
☒	☐	MRI-based neuroimaging

Antibodies

Antibodies used

Human cells were pre-enriched with either biotinylated anti-human CD4 (clone OKT4, Biolegend, Cat.No. 317406), biotinylated anti-human CD8 (clone HIT8a, Biolegend, Cat.No. 300904) or PE-labeled or biotinylated anti-human CD25 (Clone BC96, Biolegend, Cat.No. 302606 or Cat.No. 302624) at 1:20 or 1:100 dilution,
The following anti-human antibodies were used for surface staining: anti-human CD3-BV785 (OKT3, Biolegend Cat.No. 317330 or BD Biosciences Cat.No. 566782), anti-human CD4-BV711 (OKT4/L200, Biolegend Cat.No. 317440 or BD Biosciences Cat.No. 563913), anti-human TCR-β chain BV785 (IP26, Biolegend Cat.No. 306742), anti-human CD8-BUV395 (RPA-T8, BD Biosciences #563795), anti-human CD19-BV605 (HIB19, Biolegend Cat.No. 302244), anti-human CD25-PE (BC96/2A3, Biolegend Cat.No. 302606 or BD Biosciences Cat.No. 57214), anti-human CD45-BUV737 (HI30, BD Biosciences Cat.No. 748719), anti-human CD45RA-BV605 or CD45RA-BV510 (HI100, Biolegend Cat.No. 304134/304142 or BD Biosciences Cat.No. 562886), anti-human CD45RO-BV421 (UCHL1, Biolegend Cat.No. 304224), anti-human CD127-APC (A019D5, Biolegend Cat.No. 351342), anti-human CD14 BUV395 (MϕP9, BD Biosciences Cat.No. 563562), anti-human CCR8 BV421 or BUV395 (433H, BD Biosciences Cat.No. 566379 or Cat.No. 747573) at 1:20 dilution or 1:100 dilution.
All antibodies were from commercial sources and amounts and dilutions were chosen according to the manufacturers' instructions.

Murine cells were pre-enriched for CD25 by staining biotinylated anti-mouse CD25 (Clone PC61, Biolegend, Cat.No. 102003), followed by column-based magnetic separation with anti-biotin microbeads (Miltenyi Biotec #130-105-637) following manufacturer’s protocol. The following anti-mouse antibodies were used for surface staining: CD4-BUV395 (GK1.5, BD Biosciences, Cat.No. 563790), Tcr-β-BV605 (H57-597, Biolegend, Cat.No. 109241), GITR-PE-Cy7 (DTA-1, Biolegend, Cat.No. 126318), and CCR8-BV421 (SA214G2, Biolegend, Cat.No. 150305) or Rat IgG2bk BV421 Isotype Ctrl (RTK4530, Biolegend, Cat.No. 400655) at a dilution of 1:100.

Validation

All antibodies are from commercial sources and have been validated by the vendors. Validation data are available on the manufacturer's website.

Animals and other research organisms

Policy information about studies involving animals; ARRIVE guidelines recommended for reporting animal research, and Sex and Gender in Research

Laboratory animals	Tg(CAG-Kaede)15Kgwa mice (Genetic background: C57BL/6J) were a gift from Ralf Linker. Animals were housed under specific pathogen-free conditions at the Regensburg University Clinics animal care facility. We used 7 adult male and female mice between 30 and 35 weeks of age. Air exchange rates were > 8 AC/h, light/dark cycles were 12h/12h and mice were kept at ambient temperature (22±2°C) and at a relative humidity of 55 ± 10%.
Wild animals	We did not use wild animals.
Reporting on sex	We used male and female mice.
Field-collected samples	We did not use field-collected samples.
Ethics oversight	The governmental committee for animal experimentation (Regierungspräsidium Unterfranken, Bavaria, Germany) approved all experiments involving animals.

Note that full information on the approval of the study protocol must also be provided in the manuscript.

Plants

Seed stocks	NA
Novel plant genotypes	NA
Authentication	NA

Flow Cytometry

Plots

Confirm that:

☒ The axis labels state the marker and fluorochrome used (e.g. CD4-FITC).

☒ The axis scales are clearly visible. Include numbers along axes only for bottom left plot of group (a 'group' is an analysis of identical markers).

☒ All plots are contour plots with outliers or pseudocolor plots.

☒ A numerical value for number of cells or percentage (with statistics) is provided.

Methodology

Sample preparation	Sample preparation is described in detail in the Methods section of the manuscript.
Instrument	Sorting was performed with a BD FACSAriaII™ or BD FACSFusion™ cell sorter with 85 µm nozzle and 45 psi of pressure. Analysis was performed using a BD FACSSymphony A5 or A5SE.
Software	We used BD FACDiva for sorting and BD FowJo for analysis (for versions, see above).
Cell population abundance	We performed post-sort QC for all relevant populations, where feasible.
Gating strategy	Gating stategy for preparation of bisulfite sequencing samples is present in Extended Data Figure 1a. Gating strategy for samples used for amplicon-based bisulfite sequencing was the same as that used for whole-genome bisulfite sequencing. The gating strategy employed for the flow cytometry analysis of murine cells was included in the figures and/ or figure legends of the manuscript.

☒ Tick this box to confirm that a figure exemplifying the gating strategy is provided in the Supplementary Information.